

UNIVERSITY OF CALIFORNIA

Santa Barbara

**Travelling-Wave Photodetectors**

by

Kirk Steven Giboney

A dissertation submitted in partial satisfaction  
of the requirements for the degree of

Doctor of Philosophy

in

Electrical and Computer Engineering

Committee in Charge

Professor John E. Bowers, Co-Chairperson

Professor Mark J. W. Rodwell, Co-Chairperson

Professor Larry A. Coldren

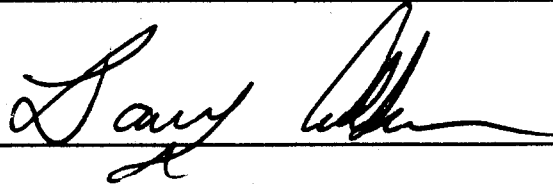
Professor Umesh K. Mishra

August 1995

The dissertation of Kirk Steven Giboney is approved



---



---



---

Committee Co-Chairperson



---

Committee Co-Chairperson

August 1995

August 4, 1995

Travelling-Wave Photodetectors

Copyright © 1995

by Kirk Steven Giboney

## ACKNOWLEDGEMENTS

– Beauty makes our pursuits worthwhile. –

Progress flows only from collective efforts. Individuals can claim no more than incremental contributions. Even so, the aptly exploited talents are not earned, but merely developed. Like our talents, our associations with our contemporaries are gifts that we choose to develop. I would like to thank several people who contributed to my education and this work.

A thesis advisor is a lot like a parent for the graduate student's intellectual and professional development. My advisors, Mark Rodwell and John Bowers, took their roles as seriously. Their technical guidance, support, and impetus, enabled this work, and greatly enhanced my life. My committee, which also included Larry Coldren and Umesh Mishra, made whole-hearted efforts not only to direct outstanding research, but to communicate the personal and professional aspects crucial to success.

The faculty have set an invaluable example of cooperation and collaboration that has been enthusiastically embraced throughout the department by staff, graduate students, and visiting and postdoctoral researchers. Radha Nagarajan helped me develop the process I used. Tom Reynolds balanced a difficult job of keeping the labs running while making significant contributions to individual research, such as the anti-reflection coatings on the travelling-wave photodetectors. Rich Mirin made sure the material he grew was appropriate and done right the first time. I learned much about high-speed photodetectors from Yih-Guei Wey while doing electro-optic sampling measurements on his.

Daily interactions among researchers contribute substantially to research results, professional maturity, and personal satisfaction. Many fruits of my interactions with Scott Allen and Masayuki Kamegawa, particularly related to device processing, were incorporated into this work. Judy Karin helped me get started on the optical bench. Dan Tauber, Ralph Spickerman, and Mike Case were comrades in microwave devices and slow-wave effects, and together, we planted many seeds of ideas. Dennis Derickson showed me the detailed workings of mode-locked semiconductor lasers. I worked with Mark Mondry at McDonnell Douglas before we came to UCSB, and we engaged in many discussions on a wide range of subjects at both places. Anish Goyal

and Dubravko Babic were always willing to discuss anything and offer help. Dan Cohen supported Professor Coldren's group and managed to help others while working on his thesis.

It has been a pleasure to work alongside many others. In Professor Bowers' group were Roger Helkey, Wenbin Jiang, Gary Wang, Chi-Kuang Sun, Rajeev Ram, Jim Dudley, Alan Mar, Pat Corvini, John Wasserbauer, Debbie Crawford, Paul Morton, Peter Blixt, Anders Petersen, Aaron Hawkins, and Kehl Sink. In Professor Rodwell's group were Ruai Yu, Eric Carman, Kimi Abe, Yoshiyuki Konishi, Uddalak Bhattacharya, Madhukar Reddy, Bipul Agarwal, Rajasekhar Pullela, and James Guthrie. There were also Scott Campbell, Joyce Olsen, Jong Chang Yi, Chi-Ping Chao, Eva Strzelecka, and many others. My special appreciation goes to Lorene Inouye for helping me to keep in balance.

I cherish our friendships and experiences together far above any other aspect of my time at UCSB. I am happy that you all shared your time and efforts with me.

I thank ARPA Optoelectronics Technology Center and Ultra Program administered by Anis Husain and Robert Leheny, Charles Tsacoyeanes at Rome Laboratories, Joe Weller at the ONT Block Program on Electro-Optics Technology, and the United States Congress for their support. I am grateful to the American taxpayers for providing funding for this work, and to the California taxpayers for funding the University of California.

I especially appreciate my parents and grandmother, and my brother and sister and their families for their support and love, and for helping me to keep my values straight.

## VITA

July 19, 1960	Born, Bakersfield, California, USA
December 1984	B.S. Physics, University of California, Davis
August 1985 – August 1988	Senior Engineer, McDonnell Douglas Astronautics Company, Huntington Beach, California
December 1990	M.S. Electrical and Computer Engineering, University of California, Santa Barbara
April 1989 – July 1995	Graduate Student Researcher, University of California, Santa Barbara
July 1990 – July 1995	Technical Consultant, Hughes Research Laboratories, Malibu, California
July 1995 –	Research Intern VI, Hewlett-Packard Laboratories, Palo Alto, California

## Publications

34. Yih-Guei Wey, Kirk Giboney, John Bowers, Mark Rodwell, Pierre Silvestre, Prabhu Thiagarajan, and Gary Robinson, "110 GHz GaInAs/InP Double Heterostructure p-i-n Photodetectors," *J. Lightwave Technol.*, vol. 13, no. 7, pp. 1490-1499, Jul., 1995.
33. Kirk Giboney, John Bowers, and Mark Rodwell, "Travelling-Wave Photodetectors," in *1995 IEEE MTT-S Microwave Symposium Digest*, pp. 159-162, May 15-19, 1995. (Invited)
32. Kirk S. Giboney, Mark J. W. Rodwell, and John E. Bowers, "Field-Screening Effects in Travelling-Wave and Vertically Illuminated p-i-n Photodetectors," presented at 1995 Conf. Lasers Electro-Optics, Baltimore, MD, May, 1995, CFB4.
31. Kirk S. Giboney, Radhakrishnan L. Nagarajan, Thomas E. Reynolds, Scott T. Allen, Richard P. Mirin, Mark J. W. Rodwell, and John E. Bowers, "Travelling-Wave Photodetectors with 172 GHz Bandwidth and 76 GHz Bandwidth-Efficiency Product," *IEEE Photon. Technol. Lett.*, vol. 7, no. 4, pp. 412-414, Apr., 1995.
30. Kirk S. Giboney, Scott T. Allen, Mark J. W. Rodwell, and John E. Bowers, "Picosecond Measurements by Free-Running Electro-Optic Sampling," *IEEE Photon. Technol. Lett.*, vol. 6, no. 11, pp. 1353-1355, Nov., 1994.
29. Radhakrishnan Nagarajan, Kirk Giboney, Rangchen Yu, Daniel Tauber, John Bowers, and Mark Rodwell, "High-Speed Optoelectronics," presented at 21st Int. Symp. Compound Semicond., San Diego, CA, Sep., 1994, WP3.1. (Invited)

28. R. H. Walden, W. E. Stanchina, R. A. Metzger, R. Y. Loo, J. Schaffner, M. W. Pierce, Y. K. Brown, F. Williams, V. Jones, J. Pikulski, M. Rodwell, K. Giboney, R. A. Mullen, R. WongQuen, and J. F. Jensen, "InP-Based Optoelectronic Integrated Receiver Front-Ends Using Heterojunction Bipolar Transistors and Base-Collector Photodiodes," presented at Eng. Found. Third Conf. High Speed Optoelectron. Devices for Commun. and Interconnects, Shell Beach, CA, Aug., 1994. (Invited)
27. Kirk Giboney, Mark Rodwell, and John Bowers, "Travelling-Wave Photodetectors," presented at Eng. Found. Third Conf. High Speed Optoelectron. Devices for Commun. and Interconnects, Shell Beach, CA, Aug., 1994. (Invited)
26. Kirk Giboney, Radhakrishnan Nagarajan, Thomas Reynolds, Scott Allen, Richard Mirin, Mark Rodwell, and John Bowers, "172 GHz, 42% Quantum Efficiency p-i-n Travelling-Wave Photodetector," presented at 52nd Annual Device Res. Conf., Boulder, CO, Jun., 1994, VIA-9.
25. Kirk S. Giboney, Scott T. Allen, Mark J. W. Rodwell, and John E. Bowers, "1.5 ps Fall-Time Measurements by Free-Running Electro-Optic Sampling," presented at Conf. Lasers Electro-Optics, Anaheim, CA, May, 1994, CME4.
24. R. H. Walden, W. E. Stanchina, R. A. Metzger, R. Y. Loo, J. Schaffner, M. W. Pierce, Y. K. Brown, F. Williams, V. Jones, J. Pikulski, M. Rodwell, K. Giboney, R. A. Mullen, and J. F. Jensen, "Broadband optoelectronic integrated receiver front-ends comprising InP-based heterojunction bipolar transistors and base-collector photodiodes," presented at Conf. Optical Fiber Commun., San Jose, CA, Feb., 1994.
23. Yih-Guei Wey, Kirk S. Giboney, John E. Bowers, Mark J. W. Rodwell, Pierre Silvestre, Prabhu Thiagarajan, and Gary Y. Robinson, "108 GHz GaInAs/InP p-i-n Photodiodes with Integrated Bias Tees and Matched Resistors," *IEEE Photon. Technol. Lett.*, vol. 5, no. 11, pp. 1310-1312, Nov., 1993.
22. John Bowers, Kirk Giboney, Yih-Guei Wey, Mark Rodwell, "New Concepts in 100 GHz High-Efficiency Photodetectors," presented at LEOS Summer Topical Meeting Optical Microwave Interactions, Santa Barbara, Jul., 1993, M1.1. (Invited)
21. Kirk S. Giboney, Yih-Guei Wey, John E. Bowers, Mark J. W. Rodwell, Pierre Silvestre, Prabhu Thiagarajan, and Gary Y. Robinson, "High-Speed GaInAs/InP p-i-n Photodiodes with Integrated Bias Tees," presented at Fifth Int. Conf. Indium Phosphide and Related Mater., Paris, France, Apr., 1993, TuE5.
20. Yih-Guei Wey, Kirk S. Giboney, John E. Bowers, Mark J. W. Rodwell, Pierre Silvestre, Prabhu Thiagarajan, and Gary Y. Robinson, "110 GHz Double Heterostructure GaInAs/InP p-i-n Photodiode," in *OSA Proc. Ultrafast Electron. Optoelectron.*, vol. 14, pp. 45-48, 1993.
19. Kirk S. Giboney, Mark J. W. Rodwell, and John E. Bowers, "Traveling-Wave Photodetectors," *IEEE Photon. Technol. Lett.*, vol. 4, no. 12, pp. 1363-1365, Dec., 1992.

18. J. G. Wasserbauer, D. J. Derickson, K. Giboney, R. J. Helkey, J. R. Karin, A. Mar, and J. E. Bowers, "Integrated Optical Transmitters and Receivers Using Multi-Segment Laser Processes," presented at LEOS Summer Topical Meeting Optical Microwave Interactions, Santa Barbara, Jul., 1992.
17. Eric Carman, Michael Case, Masayuki Kamegawa, Ruai Yu, Kirk Giboney, and M. J. W. Rodwell, "V-Band and W-Band Broad-Band, Monolithic Distributed Frequency Multipliers," *IEEE Microwave Guided Wave Lett.*, vol. 2, no. 6, pp. 253-254, Jun., 1992.
16. Eric Carman, Michael Case, Masayuki Kamegawa, Ruai Yu, Kirk Giboney, and M. J. W. Rodwell, "V-Band and W-Band Broad-Band, Monolithic Distributed Frequency Multipliers," presented at 1992 IEEE MTT-S Int. Microwave Symp., Albuquerque, NM, Jun., 1992 (in 1992 *IEEE MTT-S Microwave Symposium Digest*, pp. 819-22, Jun. 1-5, 1992).
15. Eric Carman, Michael Case, Masayuki Kamegawa, Ruai Yu, Kirk Giboney, and M. J. W. Rodwell, "Electrical Soliton Devices as >100 GHz Signal Sources," presented at Ultrafast Phenomena VIII Conf., Antibes, France, Jun., 1992.
14. M. J. W. Rodwell, Scott Allen, Masayuki Kamegawa, Kirk Giboney, Judy Karin, Michael Case, Ruai Y. Yu, and J. E. Bowers, "Picosecond Photodetectors Monolithically Integrated with High-Speed Sampling Circuits," presented at AFCEA DOD Fiber Opt. Conf., Mar., 1992.
13. Mark J. W. Rodwell, Masayuki Kamegawa, Ruai Yu, Michael Case, Eric Carman, and Kirk S. Giboney, "GaAs Nonlinear Transmission Lines for Picosecond Pulse Generation and Millimeter-Wave Sampling," *IEEE Trans. Microwave Theory Tech.*, vol. 39, no. 7, pp. 1194-1204, Jul., 1991.
12. M. Kamegawa, K. Giboney, J. Karin, S. Allen, M. Case, R. Yu, M. J. W. Rodwell, and J. E. Bowers, "Picosecond GaAs Monolithic Optoelectronic Sampling Circuit," *IEEE Photon. Technol. Lett.*, vol. 3, no. 6, pp. 567-569, Jun., 1991.
11. Y. G. Wey, D. L. Crawford, K. Giboney, J. E. Bowers, M. J. Rodwell, P. M. Sylvestre, M. J. Hafich, and G. Y. Robinson, "Ultrafast graded double-heterostructure GaInAs/InP photodiode," *Appl. Phys. Lett.*, vol. 58, no. 19, pp. 2156-2158, May 13, 1991.
10. M. J. W. Rodwell, Masayuki Kamegawa, Michael Case, Ruai Y. Yu, and Kirk Giboney, Eric Carman, Judy Karin, Scott Allen, and Jeff Franklin, "Nonlinear Transmission Lines and their Applications in Picosecond Optoelectronic and Electronic Measurements," presented at Eng. Found. Conf. High Freq./High Speed Optoelectron., Palm Beach, FL, Mar., 1991.
9. Y. Wey, D. Crawford, K. Giboney, A. Mar, J. Bowers, "Graded Double Heterostructure Photodetectors," presented at Eng. Found. Conf. High Freq./High Speed Optoelectron., Palm Beach, FL, Mar., 1991.
8. D. L. Crawford, Y. G. Wey, K. Giboney, M. Rodwell, J. Bowers, P. Sylvestre, M. Hafich, and G. Robinson, "3.8 ps FWHM Impulse Response of a Graded Double Heterostructure P-I-N Photodiode Fabricated on a Semi-Insulating Substrate," presented at Third Int. Conf. Indium Phosphide and Related Mater., Cardiff, Wales, 1991.

7. D. L. Crawford, Y. G. Wey, J. E. Bowers, K. Giboney, and M. Rodwell, "New Directions in High Speed Photodetectors," presented at Conf. Lasers Electro-Optics, Baltimore, MD, 1991, CWB6. (Invited)
6. Michael Case, Eric Carman, Masayuki Kamegawa, Kirk Giboney, Ruai Yu, Kathryn Abe, M. J. W. Rodwell, and Jeff Franklin, "Impulse Generation and Frequency Multiplication Using Soliton Effects in Monolithic GaAs Circuits," in *OSA Proc. Picosecond Electron. Optoelectron.*, vol. 9, pp. 140-144, 1991.
5. Masayuki Kamegawa, K. Giboney, J. Karin, S. Allen, M. Case, R. Yu, M. J. W. Rodwell, and J. E. Bowers, "Picosecond GaAs Photodetector Monolithically Integrated with a High-Speed Sampling Circuit," in *OSA Proc. Picosecond Electron. Optoelectron.*, vol. 9, pp. 104-107, 1991.
4. D. L. Crawford, Y. G. Wey, K. Giboney, J. E. Bowers, M. J. Rodwell, P. M. Sylvestre, M. J. Hafich, and G. Y. Robinson, "Ultrafast Graded Double-Heterostructure p-i-n Photodiode," in *OSA Proc. Picosecond Electron. Optoelectron.*, vol. 9, pp. 92-96, 1991. (Invited)
3. Eric Carman, Kirk Giboney, Michael Case, Masayuki Kamegawa, Ruai Yu, Kathryn Abe, M. J. W. Rodwell, and Jeff Franklin, "28–39 GHz Distributed Harmonic Generation on a Soliton Nonlinear Transmission Line," *IEEE Microwave Guided Wave Lett.*, vol. 1, no. 2, pp. 28-31, Feb., 1991.
2. Y. G. Wey, M. Kamegawa, A. Mar, K. J. Williams, K. Giboney, D. L. Crawford, J. E. Bowers, and M. Rodwell, "Hybrid Integration of an InGaAs/InP PIN Photodiode with an Ultrafast Sampling Circuit," presented at Conf. Optical Fiber Commun., San Diego, CA, 1991, PD8-1.
1. M. Case, M. Kamegawa, K. Giboney, M. Rodwell, J. Franklin, and J. E. Bowers, "62.5 ps to 5.5 ps Soliton Compression on a Monolithic Nonlinear Transmission Line," presented at 48th Annual Device Res. Conf., Santa Barbara, CA, Jun., 1990, VA-2.

## **ABSTRACT**

### **Travelling-Wave Photodetectors**

by

Kirk Steven Giboney

Photodetector efficiency decreases as bandwidth increases. Bandwidth-efficiency products of vertically illuminated photodetectors are limited to about 40 GHz. This product imposes a bound on the speed and sensitivity of photoreceivers used in optical transmission systems.

Waveguide photodetectors are an attractive option for increasing the bandwidth-efficiency product over the intrinsic limit of vertically illuminated photodetectors. By guiding the illumination perpendicular to the carrier drift field, the inherent tradeoff between efficiency and the transit-time bandwidth limitation is diminished. However, even higher bandwidth-efficiency products are possible with consideration for the propagation of the electrical waves to the load.

Attention to the microwave design of waveguide photodetectors leads to travelling-wave photodetectors. A travelling-wave photodetector is a waveguide photodetector with an electrode structure designed to support travelling electrical waves with characteristic impedance matched to that of the external circuit. The travelling-wave photodetector is thus modelled by a matched section of transmission line with an exponentially decaying photocurrent source propagating on it at the optical group velocity.

The mismatch between the group velocity of the photocurrent source and the phase velocities of the electrical waves it generates limits travelling-wave photodetector bandwidth. The velocity-mismatch bandwidth limitation is essentially independent of device length, so a travelling-wave photodetector can arbitrarily be made long enough for nearly 100% internal quantum efficiency without compromising bandwidth. A simple form for the velocity-mismatch bandwidth limitation is derived that affords physical insight and provides a basis for using traditional design methods.

The first theory, fabrication, and measurement of travelling-wave photodetectors comprise this thesis work. New developments in electro-optic techniques enable measurements of bandwidths as high as 190 GHz, the highest reported for a p-i-n photodetector by more than 70%. The travelling-wave photodetectors display bandwidth-efficiency products as large as 84 GHz, breaking the record for any photodetector without gain by 50%. Comparisons with vertically illuminated and waveguide photodetectors fabricated on the same wafer establish the advantage of travelling-wave photodetectors.

# CONTENTS

<b>1</b>	<b>INTRODUCTION .....</b>	<b>1</b>
1.1	Background	1
1.2	Range and Organization of this Dissertation	8
	References	10
<b>2</b>	<b>THEORY OF DISTRIBUTED PHOTODETECTION.....</b>	<b>13</b>
2.1	Photodetector-Electrical Waveguide	14
2.2	Equivalent-Circuit Model	20
2.3	Velocity-Mismatch Impulse Response	28
2.4	Velocity-Mismatch Bandwidth Limitation	34
2.5	Space-Charge Field Screening	40
	References	44
<b>3</b>	<b>DESIGN &amp; FABRICATION .....</b>	<b>47</b>
3.1	Hybrid-Coplanar Travelling-Wave Photodetector	47
3.2	Bandwidth Model	51
3.3	Device Design	53
3.4	Fabrication	60
	References	70
<b>4</b>	<b>ELECTRO-OPTIC MEASUREMENT TECHNIQUES.....</b>	<b>73</b>
4.1	Electro-Optic Probe Station	73
4.2	Electro-Optic Sampling	78
4.3	System Response	83
4.4	Deconvolution	86
4.5	Noise & Interference	89
	References	95

<b>5</b>	<b>MEASUREMENTS &amp; ANALYSIS .....</b>	<b>99</b>
5.1	Travelling-Wave Photodetector Performance	99
5.2	Propagation Constant	105
5.3	Electro-Optic Sampling System Response Correction	111
5.4	Reflection Deconvolution	115
5.5	Field-Screening Effects	117
	References	122
<b>6</b>	<b>OVERVIEW.....</b>	<b>123</b>
6.1	Summary	123
6.2	Further Analysis & Improvements	125
6.3	Periodic Travelling-Wave Photodetector	127
6.4	Applications	131
	References	132
<b>A</b>	<b>TRANSVERSE-RESONANCE SOLUTION PROGRAM.....</b>	<b>135</b>
A.1	Main Script	135
A.2	Specific Functions	140
A.3	General Functions & Scripts	142
	References	143
<b>B</b>	<b>FABRICATION PROCESS .....</b>	<b>145</b>
B.1	Process Plan	145
B.2	Cleaning, Photolithography, & Spin-On Films	154
B.3	Chemical Specifications & Preparation	157
	References	158

# CHAPTER 1

## INTRODUCTION

Optical fiber communications is the primary means of transmitting information over long distances today. The National Information Infrastructure, or "Information Superhighway," envisions a large-scale, high-speed computer network covering the entire nation and connecting with the rest of the world. Full realization of this plan will require large increases in the transmission capacity of our optical communications systems. This will be achieved by increasing transmission rates through greater time-division multiplexing (TDM), and further exploiting the optical bandwidth of silica fibers with optical-frequency-division multiplexing (OFDM).

Optoelectronic instrumentation must keep a step ahead of the communications industry and also keep pace with developments in short-pulse lasers. Commercially available mode-locked solid-state lasers that produce ultrafast optical pulses are driving new scientific, medical, manufacturing, and military applications. Conventional photodetectors and electronics that have routinely met the demands of optoelectronic systems are now being pressed to their limits and beyond.

This work encompasses the invention of the travelling-wave photodetector (TWPD). With this new device, the largest simultaneous bandwidth and efficiency of a photodetector is demonstrated, and a significantly higher fundamental limit on photodetector performance is exposed. The introduction of the TWPD contributes to continuing advances in high-speed optoelectronics and will enable larger capacity in future optoelectronic systems.

### 1.1 Background

A photodetector is an optical-to-electrical transducer. High-speed photodetectors are capable of converting high-modulation-frequency optical signals into electrical signals. Efficient photodetectors convert a large fraction of the light to electricity.

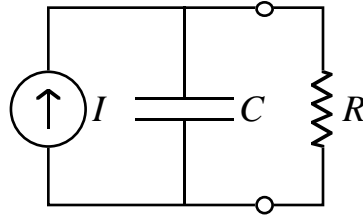


Fig. 1.1 Simplified circuit diagram of a lumped-element photodetector and load showing the photocurrent source, capacitance of the depletion region, and load resistance.

High-speed photodetectors must have good efficiency to be useful, so bandwidth and efficiency are the primary measures of high-speed photodetector performance.

A photodetector can be viewed as a two port device with an optical input and an electrical output. As a linear system, it is completely characterized by its impulse or frequency response. Photodetector performance is conventionally summarized by specifying two parameters: bandwidth and quantum efficiency. Bandwidth is generally taken to be the lowest frequency at which the magnitude electrical response is less than -3 dB from the DC (zero frequency) response. Quantum efficiency is also called external quantum efficiency, the ratio of unit charges collected to photons incident. The bandwidth-efficiency product is an important figure of merit for photodetectors.

A simplified circuit diagram of a lumped-element photodetector is drawn in Fig. 1.1. The bandwidth of such a device is limited by the response of the current source and the response of the overall circuit. The response of the current source, transit response, applies to all photodetectors and is determined by the velocities of photogenerated electrons and holes and the distances they travel. Assuming carriers are uniformly generated across the depletion layer and the carrier velocities are constant and equal, the transit bandwidth limitation is given by

$$B_t = 0.55 \frac{v_d}{d} \quad (1.1)$$

where  $v_d$  is the electron and hole drift velocity, and  $d$  is the thickness of the depletion region, which is the distance travelled by the carriers. Clearly, large bandwidth requires a thin depletion region.

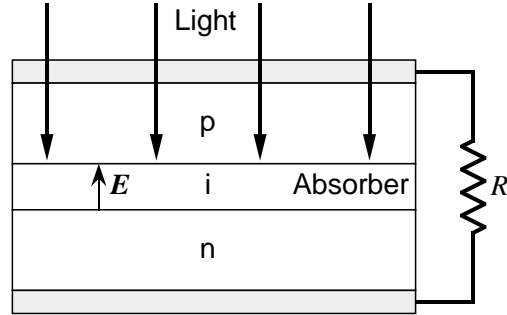


Fig. 1.2 Schematic diagram of a vertically illuminated photodetector.

The circuit RC response applies only to lumped-element photodetectors, and it depends on the area and thickness of the depletion region and the series resistance. The RC bandwidth limitation is given by

$$B_{RC} = \frac{1}{2\pi RC} \quad (1.2)$$

where  $R$  is the series resistance.  $C = \epsilon A/d$ , where  $\epsilon$  is the dielectric constant of the depletion layer and  $A$  is its area.

The general form for external quantum efficiency of a photodetector is

$$\eta = \eta_c (1 - R) (1 - e^{-\Gamma \alpha \ell}) \quad (1.3)$$

where  $\eta_c$  is the modal coupling efficiency,  $R$  is the Fresnel reflectivity,  $\Gamma$  is the modal confinement factor,  $\alpha$  is the optical power absorption coefficient of the absorbing layer material, and  $\ell$  is the optical absorption path length in the depletion region.

The vertically illuminated photodetector (VPD), drawn conceptually in Fig. 1.2, is the most common type. Light is incident perpendicular to the device layers in this type of device. All of the light is coupled directly into the absorbing layer in a VPD, so  $\eta_c = 1$  and  $\Gamma = 1$ , and if light passes through only once,  $\ell = d$ . A thin depletion layer is required for large bandwidth, according to (1.1), however this reduces the quantum efficiency in (1.3). In the limit of a thin depletion layer, (1.3) becomes  $\eta \approx (1 - R)\alpha d$ . A fundamental limit to the bandwidth-efficiency product for VPDs

can be derived from (1.1) and (1.3) by assuming that the junction area,  $A$ , can be decreased arbitrarily to eliminate the RC bandwidth limitation imposed in (1.2). The bandwidth-efficiency product then takes on a simple form for VPDs

$$B\eta = 0.55\alpha v_d \quad (1.4)$$

where the reflectivity has been set to zero [1]. High-field electron and hole velocities in GaAs are about 70 nm/ps. Assuming  $\alpha = 1 \mu\text{m}^{-1}$ , the maximum possible bandwidth-efficiency product for a single-pass GaAs VPD is about 40 GHz.

In light of (1.4), an obvious means of obtaining high bandwidth-efficiency product is to choose a material that has a large product of carrier velocity and absorption coefficient at the wavelength range of interest. Availability of materials and fabrication resources severely restricts the prospects of homogeneous, or bulk, semiconductors, however quantum confinement structures offer additional possibilities.

Quantum wells, wires, or dots (one, two, or three dimensional quantum confinement structures) have peaks in the absorption coefficient over narrow bands of photon energies. The carrier mobility and saturated drift velocity is also enhanced in quantum wells and wires due to suppression of scattering mechanisms. A theoretical study of quantum wire photodetectors concluded that the increase in absorption in the wires is likely to be compromised by dimensional and compositional variations, and further offset by the fill-factor [2]. Large drift velocity enhancements over saturated bulk values were assumed to predict bandwidth-efficiency product improvements over bulk material. The temperature dependence of the absorption spectra in quantum structures can make temperature stabilization necessary.

There are several approaches to increasing the bandwidth-efficiency product over the inherent VPD limit expressed in (1.4). Mirrors are used to reflect light through the absorber several times in the resonant-cavity-enhanced (RCE) photodetector, as depicted in Fig. 1.3 [3-4]. This effectively increases the absorption length,  $\ell$  in (1.3), but not the distance travelled by the carriers,  $d$  in (1.1). The efficiency can then go to unity while the bandwidth is still determined by (1.1) and (1.2). Added series resistance due to the mirrors has limited p-i-n RCE bandwidths to 17 GHz [5], although this has apparently been overcome in metal-semiconductor-metal (MSM)

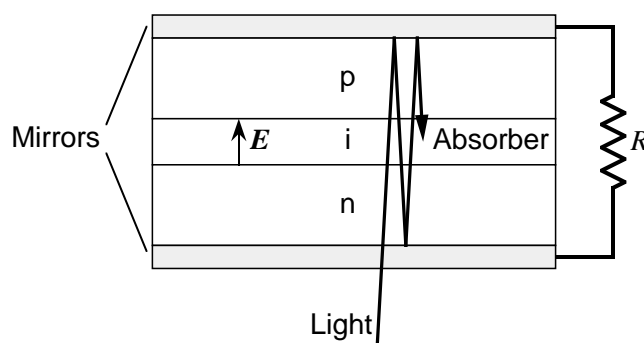


Fig. 1.3 Schematic diagram of a resonant-cavity-enhanced photodetector.

type devices showing bandwidths over 40 GHz [6]. The absorption spectra of RCE photodetectors are peaked at the Fabry-Perot cavity resonances. As in other narrowband optical devices, the peak wavelengths are temperature dependent.

Frequency demultiplexing photoreceivers for OFDM systems have been proposed using Bragg-reflector-based, frequency-selective elements [7]. However, the frequency channels are split  $n$  times and then fed to  $n$  photodetectors. Since all channels are sent to each photodetector, the overall efficiency of such a system is  $1/n$ . Furthermore, the fact that the optical power outside the absorption band is reflected presents a major problem. A large fraction,  $(n-1)/n$ , of the optical power is reflected back into the transmitter, adding demands on isolation. A satisfactory scheme for efficiently collecting light reflected from an RCE photodetector and directing it to other channels appears unlikely.

The waveguide photodetector (WGPD), schematically drawn in Fig. 1.4(a), is another option for increasing the bandwidth-efficiency product over the intrinsic limit of conventional VPDs [1, 8]. The WGPD is an in-plane illuminated photodetector in which transparent dielectric cladding layers about the absorbing core form a dielectric optical waveguide [9-13]. The illumination is guided perpendicular to the carrier drift field, allowing a long absorption path while maintaining a small junction area, so the interdependence of bandwidth and internal efficiency is reduced. High external efficiency then depends on coupling most of the light into the waveguide, which can be accomplished by appropriate design of the device layers [14] or by the use of separate input waveguide segments [15-18].

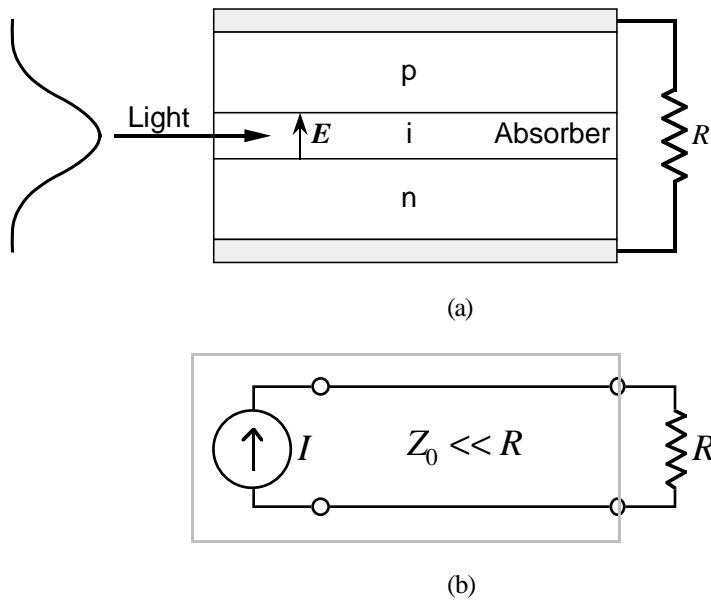


Fig. 1.4 Waveguide photodetector (a) schematic drawing and (b) simplified circuit diagram showing low characteristic impedance electrical wave propagation.

Electrically, the WGPD is modelled as a lumped-element device and its bandwidth limitations are essentially the same as those for a VPD. Mushroom-mesa WGPDs of InGaAs/InP have demonstrated 110 GHz bandwidth with 50% quantum efficiency at 1.55  $\mu\text{m}$  wavelength [19]. This 55 GHz bandwidth-efficiency product is much greater than the inherent VPD single-pass limit of about 30 GHz limit for InGaAs at that wavelength.

WGPDs maintain their performance over a broad optical bandwidth and wide temperature range, and their structure is well-suited for integration with other optical waveguide components [20], particularly integrated semiconductor optical preamplifiers [21]. Practical schemes for optical frequency demultiplexing photoreceivers make use of integrated planar gratings to split the incoming frequencies into  $n$  beams, which are then directed to  $n$  photodetectors [22-27]. The greater flexibility afforded by separating the demultiplexing and photodetection functions results in superior performance and manufacturability. Waveguide-type photodetectors are the natural choice in such applications.

A weakness of WGPDs is that they are generally designed without regard for the propagation of electrical waves to the load. There is either an unsuitable electrical

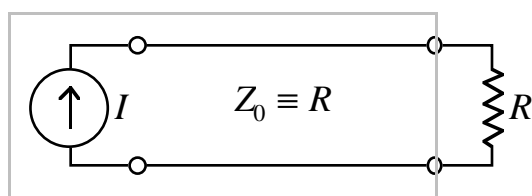


Fig. 1.5 Simplified circuit diagram of a travelling-wave photodetector. The travelling-wave photodetector is a matched electrical transmission line.

waveguide or connection, or there is a large impedance mismatch between the photodetector and the load, as suggested in the simplified circuit diagram of Fig. 1.4(b). Multiple electrical reflections in the device cause the entire junction area to participate in the response. This is why WGPDs are best represented by a lumped-element model, as in Fig. 1.1, and suffer from an RC bandwidth limitation in which the device capacitance is determined by the total junction area.

The travelling-wave photodetector (TWPD) is a fully distributed structure that overcomes the RC bandwidth limitation of the lumped-element WGPD, while retaining the advantages of the WGPD for optical bandwidth, temperature range, and integrability. It is based on the WGPD, but has an electrode arrangement designed to support travelling electrical waves with characteristic impedance matched to that of the external circuit, as indicated in the simplified circuit diagram of Fig. 1.5 [28].

The TWPD is modelled by a terminated section of transmission line with an exponentially decaying photocurrent source propagating on it at the optical group velocity. The TWPD velocity-mismatch bandwidth limitation depends on the optical absorption coefficient and the mismatch between optical group velocity and electrical phase velocity, as opposed to an RC bandwidth limitation determined by the total junction area. TWPDs are not subject to the same RC bandwidth limitation as lumped-element photodetectors and can simultaneously have a large bandwidth and high efficiency.

The concept of the TWPD was first presented in 1990 as a means to overcome the bandwidth-efficiency limits of conventional photodetectors [29]. Both p-n and Schottky junctions were briefly mentioned, although the several designs listed in the proposal were of the metal-semiconductor type. The bandwidths of the proposed structures, as depicted by the schematic drawings, would have been severely limited

by transit-time. No detailed theory or experimental results from these designs have been reported.

The use of doped layers generally results in a slow-wave structure. However, in 1991, a proposal for a velocity-matched p-i-n TWPD was announced [30]. A theory of the effects of velocity matching on device response was not included in this report. This group is focussed on high-power, high-bandwidth applications. Their efforts to date have yielded devices with only 4.8 GHz bandwidth [31].

Unaware of other efforts, we began to investigate ways to improve conventional WGDs at UCSB in 1991 and immediately conceived of the TWPD. We were the first to publish the basic theory of TWPDs, quantifying the velocity mismatch impulse response and associated bandwidth limitations [28]. We subsequently published the first experimental demonstration of TWPDs in 1994 [32]. The TWPDs demonstrated significantly higher bandwidths and bandwidth-efficiency products than comparable WGDs and VPDs on the same wafer [33]. After correcting for the measurement system response, these devices showed bandwidths as high as 190 GHz and bandwidth-efficiency products as large as 84 GHz, breaking the records for bandwidth of a p-i-n photodetector by 70% and bandwidth-efficiency product of any photodetector without gain by 50%.

## **1.2 Range and Organization of this Dissertation**

This dissertation covers the invention of the travelling-wave photodetector, including the first demonstration of a prototype device. Analysis of the results show reasonable correlation with the definition and description. The conception, theory, design, fabrication, measurement, and analysis of TWPDs are all included in this dissertation.

This introduction provides motivation and background for the work, and it lays out the structure of the subsequent presentation. High-speed photodetector theory as it relates to primary performance parameters is outlined. A cursory description of various types of photodetectors and their performance characteristics is then followed by the origins and brief history of the TWPD.

Chapter Two presents the theory that distinguishes the TWPD, laying the foundation for the rest of the dissertation. The model for a fully distributed

photodetector is presented. The photodetector structure electrical waveguide properties are analyzed and the velocity-mismatch impulse response is derived. The velocity-mismatch effective area is deduced from the velocity-mismatch frequency response. This area facilitates the use of conventional methods of photodetector design and analysis on TWPDs. A simple theory of field-screening effects, which limit the high-illumination response of photodetectors, is presented using empirical parameters.

Chapter Three applies the theory presented in Chapter Two to the design and fabrication of TWPDs. A bandwidth model for a practical device structure is developed and used along with optoelectronic device physics, processing, and measurement considerations to optimize a device design. The modified ridge-waveguide laser process used to fabricate TWPDs is described with special attention to unique and newly developed features.

Chapter Four covers the construction of an electro-optic sampling system, which was adjunct to this thesis work. The system hardware and principles are described with special attention to new developments important for high-speed photodetector measurements.

Chapter Five presents measurement results with emphasis on evidence of TWPDs. Travelling wave properties are elucidated and contrasted to lumped element characteristics of the WGDs and VPDs. Post-measurement signal processing increases the range of measurement parameters over which accurate analysis is possible. Measurements of field-screening effects support the theory presented in Section 2.5.

Chapter Six summarizes this work and draws some conclusions. Successes and shortcomings are discussed, providing seeds for future directions. Natural extensions of the TWPD concept and applications of the technology are proposed.

Appendix A lists a Matlab program used for calculating results presented in Sections 2.1 and 2.2 [34]. Appendix B details the TWPD fabrication process described in Section 3.4.

## References

- [1] J. E. Bowers and C. A. Burrus, Jr., "Ultrawide-Band Long-Wavelength p-i-n Photodetectors," *J. Lightwave Technol.*, vol. 5, no. 10, pp. 1339-1350, Oct., 1987.
- [2] D. L. Crawford, R. L. Nagarajan, and J. E. Bowers, "Comparison of Bulk and Quantum Wire Photodetectors," *Appl. Phys. Lett.*, vol. 58, no. 15, pp. 1629-1631, Apr. 15, 1991.
- [3] A. Chin and T. Y. Chang, "Enhancement of Quantum Efficiency in Thin Photodiodes Through Absorptive Resonance," *J. Lightwave Technol.*, vol. 9, no. 3, pp. 321-328, Mar., 1991.
- [4] K. Kishino, M. S. Ünlü, J. Chyi, J. Reed, L. Arsenault, and H. Morkoç, "Resonant Cavity-Enhanced (RCE) Photodetectors," *IEEE J. Quantum Electron.*, vol. 27, no. 8, pp. 2025-2034, Aug., 1991.
- [5] C. C. Barron, C. J. Mahon, B. J. Thibeault, G. Wang, W. Jiang, L. A. Coldren, and J. E. Bowers, "Resonant-Cavity-Enhanced p-i-n Photodetector with 17 GHz Bandwidth-Efficiency Product," *Electron. Lett.*, vol. 30, no. 21, pp. 1796-1797, Oct. 13, 1994.
- [6] K. Litvin, J. Burm, D. Woodard, W. Schaff, and L. F. Eastman, "High Speed Optical Detectors for Monolithic Millimeter Wave Integrated Circuits," in *1993 IEEE MTT-S Microwave Symposium Digest*, pp. 1063-1066, Jun. 14-18, 1993.
- [7] G. P. Agrawal and S. Radic, "Phase-Shifted Fiber Bragg Gratings and their Application for Wavelength Demultiplexing," *IEEE Photon. Technol. Lett.*, vol. 6, no. 8, pp. 995-997, Aug., 1994.
- [8] A. Alping, "Waveguide pin Photodetectors: Theoretical Analysis and Design Criteria," *IEE Proc. J*, vol. 136, no. 3, pp. 177-182, Jun., 1989.
- [9] F. K. Reinhart, "Electroabsorption in  $\text{Al}_y\text{Ga}_{1-y}\text{As}-\text{Al}_x\text{Ga}_{1-x}\text{As}$  Double Heterostructures," *Appl. Phys. Lett.*, vol. 22, no. 8, pp. 372-374, Apr. 15, 1973.
- [10] J. L. Merz and R. A. Logan, "Integrated  $\text{GaAs}-\text{Al}_x\text{Ga}_{1-x}\text{As}$  Injection Lasers and Detectors with Etched Reflectors," *Appl. Phys. Lett.*, vol. 30, no. 10, pp. 530-533, May 15, 1977.
- [11] A. Alping and S. T. Eng, "Detection at Gbit/s Rates with a TJS  $\text{GaAlAs}$  Laser," *Opt. Commun.*, vol. 44, no. 6, pp. 381-383, Feb. 15, 1983.
- [12] J. E. Bowers and C. A. Burrus, "High-Speed Zero-Bias Waveguide Photodetectors," *Electron. Lett.*, vol. 22, no. 17, pp. 905-906, Aug. 14, 1986.
- [13] D. Wake, T. P. Spooner, S. D. Perrin, and I. D. Henning, "50 GHz  $\text{InGaAs}$  Edge-Coupled pin Photodetector," *Electron. Lett.*, vol. 27, no. 12, pp. 1073-1075, Jun. 6, 1991.
- [14] K. Kato, S. Hata, K. Kawano, J. Yoshida, and A. Kozen, "A High-Efficiency 50 GHz  $\text{InGaAs}$  Multimode Waveguide Photodetector," *IEEE J. Quantum Electron.*, vol. 28, no. 12, pp. 2728-2735, Dec., 1992.
- [15] Y. Shani, C. H. Henry, R. C. Kistler, K. J. Orlowsky, and D. A. Ackerman, "Efficient coupling of a semiconductor laser to an optical fiber by means of a tapered waveguide on silicon," *Appl. Phys. Lett.*, vol. 55, no. 23, pp. 2389-2391, Dec. 4, 1989.

- [16] T. Brenner and H. Melchior, "Integrated Optical Modeshape Adapters in InGaAsP/InP for Efficient Fiber-to-Waveguide Coupling," *IEEE Photon. Technol. Lett.*, vol. 5, no. 9, 1053-1056, Sep., 1993.
- [17] S. El Yumin, K. Komori, and S. Arai, "GaInAsP/InP Semiconductor Vertical GRIN-Lens for Semiconductor Optical Devices," *IEEE Photon. Technol. Lett.*, vol. 6, no. 5, pp. 601-604, May, 1994.
- [18] I. Moerman, M. D'Hondt, W. Vanderbauwhede, G. Coudenys, J. Haes, P. De Dobbelaere, R. Baets, P. Van Daele, and P. Demeester, "Monolithic Integration of a Spot Size Transformer with a Planar Buried Heterostructure in GaAsP/InP-Laser using the Shadow Masked Growth Technique," *IEEE Photon. Technol. Lett.*, vol. 6, no. 8, pp. 888-890, Aug., 1994.
- [19] K. Kato, A. Kozen, Y. Muramoto, Y. Itaya, T. Nagatsuma, and M. Yaita, "110-GHz, 50%-Efficiency Mushroom-Mesa Waveguide p-i-n Photodiode for a 1.55- $\mu\text{m}$  Wavelength," *IEEE Photon. Technol. Lett.*, vol. 6, no. 6, 719-721, Jun., 1994.
- [20] R. J. Deri, "Monolithic Integration of Optical Waveguide Circuitry with III-V Photodetectors for Advanced Lightwave Receivers," *J. Lightwave Technol.*, vol. 11, no. 8, pp. 1296-1313, Aug., 1993.
- [21] D. Wake, "A 1550-nm Millimeter-Wave Photodetector with a Bandwidth-Efficiency Product of 2.4 THz," *J. Lightwave Technol.*, vol. 10, no. 7, pp. 908-912, Jul., 1992.
- [22] P. A. Kirby, "Multichannel Wavelength-Switched Transmitters and Receivers— New Component Concepts for Broad-Band Networks and Distributed Switching Systems," *J. Lightwave Technol.*, vol. 8, no. 2, pp. 202-211, Feb., 1990.
- [23] W. J. Grande, J. E. Johnson, C. L. Tang, "GaAs/AlGaAs photonic integrated circuits fabricated using chemically assisted ion beam etching," *Appl. Phys. Lett.*, vol. 57, no. 24, pp. 2537-2539, Dec. 10, 1990.
- [24] C. Cremer, N. Emeis, M. Schier, G. Heise, G. Ebbinghaus, and L. Stoll, "Grating Spectrograph Integrated with Photodiode Array in InGaAsP/InGaAs/InP," *IEEE Photon. Technol. Lett.*, vol. 4, no. 1, pp. 108-110, Jan., 1992.
- [25] P. C. Clemens, G. Heise, R. März, H. Michel, A. Reichelt, and H. W. Schneider, "8-Channel Optical Demultiplexer Realized as SiO<sub>2</sub>/Si Flat-Field Spectrograph," *IEEE Photon. Technol. Lett.*, vol. 6, no. 8, pp. 1109-1111, Sep., 1994.
- [26] C. Dragone, "An NxN Optical Multiplexer Using a Planar Arrangement of Two Star Couplers" *IEEE Photon. Technol. Lett.*, vol. 3, no. 9, pp 812-815, Sep., 1991.
- [27] C. Dragone, C. A. Edwards, and R. C. Kistler, "Integrated Optics NxN multiplexor in Silicon" *IEEE Photon. Technol. Lett.*, vol. 3, no. 10, pp 896-899, Oct., 1991.
- [28] K. S. Giboney, M. J. W. Rodwell, and J. E. Bowers, "Traveling-Wave Photodetectors," *IEEE Photon. Technol. Lett.*, vol. 4, no. 12, pp. 1363-1365, Dec., 1992.
- [29] H. F. Taylor, O. Eknoyan, C. S. Park, K. N. Choi, and K. Chang, "Traveling Wave Photodetectors," *Proc. SPIE - The International Society for Optical Engineering*, vol.1217, pp. 59-63, 1990.

- [30] V. M. Heitala and G. A. Vawter, "A Large-Bandwidth High-Quantum-Efficiency Traveling-Wave Photodetector Based on a Slow-Wave Coplanar Transmission Line," presented at Prog. Electromagnetics Res. Symp., Cambridge, MA, Jul., 1991.
- [31] V. M. Hietala, G. A. Vawter, T. M. Brennan, and B. E. Hammons, "Traveling-Wave Photodetectors for High-Power Large Bandwidth Applications," *IEEE Trans. Microwave Theory Tech.*, submitted, 1995
- [32] K. Giboney, R. Nagarajan, T. Reynolds, S. Allen, R. Mirin, M. Rodwell, and J. Bowers, "172 GHz, 42% Quantum Efficiency p-i-n Travelling-Wave Photodetector," presented at 52nd Annual Device Res. Conf., Boulder, CO, Jun., 1994, VIA-9.
- [33] K. S. Giboney, R. L. Nagarajan, T. E. Reynolds, S. T. Allen, R. P. Mirin, M. J. W. Rodwell, and J. E. Bowers, "Travelling-Wave Photodetectors with 172 GHz Bandwidth and 76 GHz Bandwidth-Efficiency Product," *IEEE Photon. Technol. Lett.*, vol. 7, no. 4, pp. 412-414, Apr., 1995.
- [34] The MathWorks, Inc., *The Student Edition of Matlab Version 4*. Englewood Cliffs, NJ: Prentice Hall, 1995.

## CHAPTER 2

# THEORY OF DISTRIBUTED PHOTODETECTION

A travelling-wave photodetector (TWPD) is generally much shorter than the electrical wavelengths that it is designed for, but much longer than its optical absorption length. The interaction of the optical and electrical waves, or photodetection, occurs over the relatively short optical absorption length. This length and the electrical and optical wave velocities determine the device response. Thus a distributed, rather than lumped, model applies.

The TWPD is based on the waveguide photodetector (WGPD). The characteristics of the TWPD that distinguish it from the WGPD are a TEM or quasi-TEM electrical waveguide that is concomitant with the optical dielectric waveguide, and a matched electrical termination at the device output end. These features provide for controlled transmission of the electrical wave down the device in parallel with the optical wave and eliminate bandwidth-limiting reflections.

The potential for copropagation of electrical and optical waves in a photodetector naturally presents the prospect of designing travelling-wave device. A travelling-wave structure is defined when two or more distinct waves, optical, electrical, acoustical, or other, interact over some distance as they propagate down their respective waveguides. If the interaction is coherent over the distance of interest, then the device can be said to be velocity-matched. The distance of interest in a TWPD is determined by the optical absorption.

TWPDs are generally not velocity-matched. Electrical waves propagate in the slow-wave mode and are usually drastically slower than the optical waves generating them. This results in a distortion of the signal that is the origin of the velocity-mismatch bandwidth limitation. The velocity-mismatch impulse response is derived directly from the optical group and electrical phase velocities and the optical absorption. A simple form for the velocity-mismatch bandwidth limitation allows determination of the overall photodetector bandwidth by traditional methods. It is

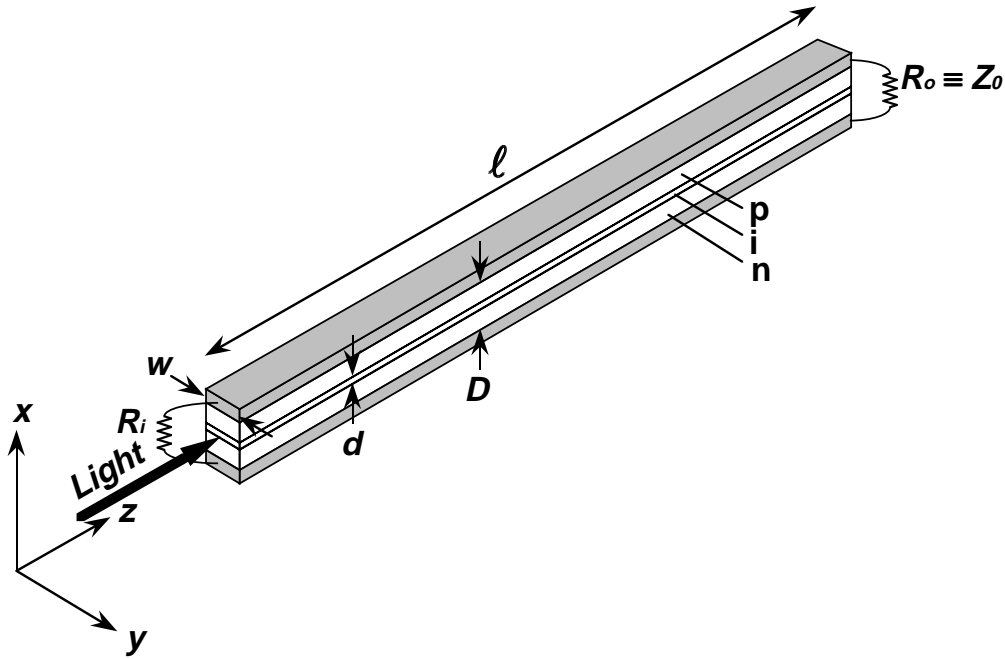


Fig. 2.1 Fully distributed, parallel-plate, p-i-n TWPD schematic diagram. The termination at the output end is defined to match the characteristic impedance of the device.

clear from this form that the velocity-mismatch bandwidth limitation is nearly independent of TWPD length.

Photodetector performance under high-power illumination is important for many applications. High photogenerated charge densities cause nonlinear response in high-speed photodetectors primarily by field screening, resulting in distorted output and reduced bandwidth. A heuristic theory explains how TWPDs take advantage of a mechanism by which in-plane illuminated photodetectors adapt to high-power illumination.

### 2.1 Photodetector-Electrical Waveguide

The TWPD is an electrical and optical waveguide. The fully distributed TWPD structure drawn in Fig. 2.1 allows an analytical representation, and offers insight into the electrical propagation characteristics. In addition to forming the photodiode, the metal-clad, p-i-n structure is a parallel-plate electrical waveguide, and the double-heterostructure semiconductor layers form a planar dielectric optical waveguide. In this section, the electrical propagation characteristics of this structure are analyzed

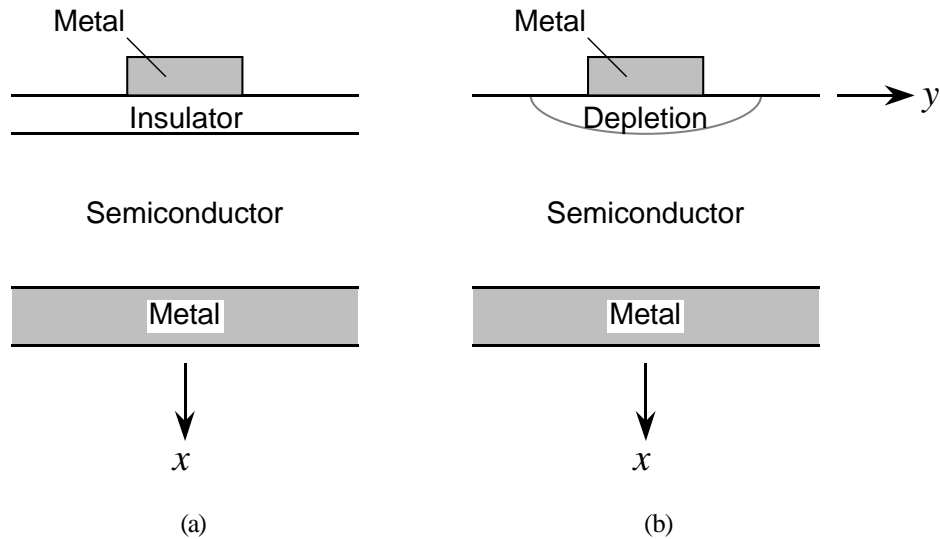


Fig. 2.2 Metal-insulator-semiconductor (MIS) structures for (a) integrated circuit interconnects and (b) Schottky contact transmission line.

from the wave equation using the transverse-resonance method. Losses associated with finite metal conductivity are accounted for.

The TWPD structure is similar to metal-insulator-semiconductor (MIS) structures that have been extensively analyzed [1-17]. MIS structures, such as those drawn in Fig. 2.2, are of interest because they arise when interconnects or Schottky contacts are fabricated on semiconducting substrates. The properties of transmission lines formed in this manner are of consequence for a wide range of integrated circuits and devices. They are called "slow-wave" transmission lines because the phase velocities of supported modes are much slower than expected simply from the permittivities and permeabilities of the media.

The parallel-plate configuration of Fig. 2.1 allows accurate two-dimensional analysis [1-3]. More complicated structures nominally require three-dimensional analyses [4-12], however certain symmetries often permit an effective dimensional reduction [13-17]. Such approaches are discussed in Chapter 3 in conjunction with TWPD design and fabrication.

The structure of the TWPD differs from that of an MIS structure by an additional semiconductor layer, however the general characteristics of the waves supported on these structures are similar. This is seen by assuming that the p- and n-layers of the

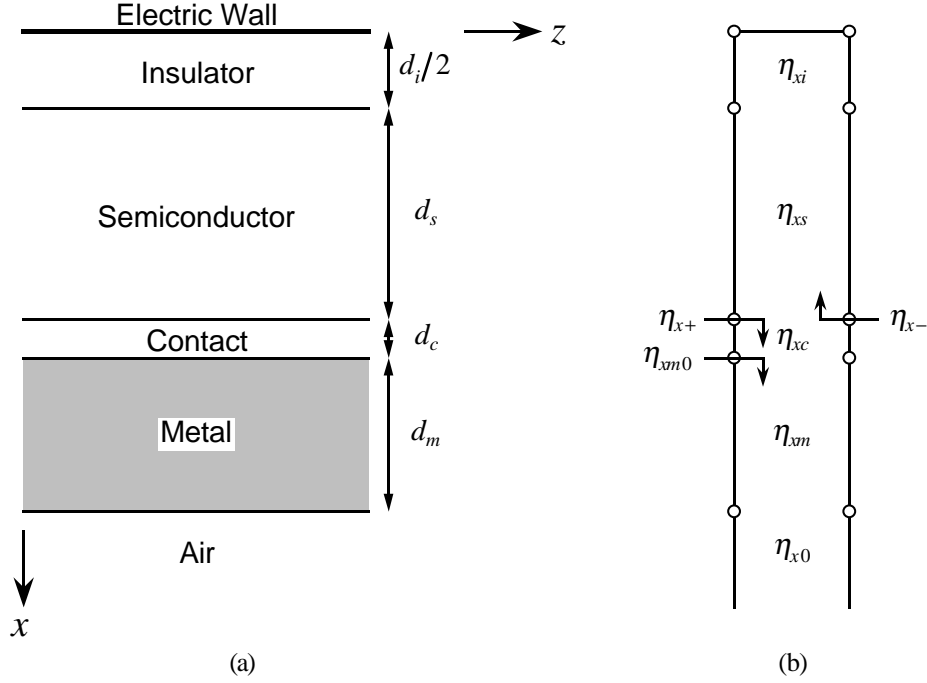


Fig. 2.3 TWPD half-waveguide (a) layer structure and (b) transmission line equivalent circuit for transverse waves.

TWPD are of equal conductivity and thickness, and then applying image theory. The waveguide is cut in half, as shown in Fig. 2.3(a), with an electric wall at the plane of symmetry. The TWPD now looks like an MIS structure with a perfect conductor as the top metal. A thin (10 nm) contact layer is included in the model of Fig. 2.3 to simulate the metal-semiconductor junction.

This structure is analyzed by starting with the time-harmonic form of Maxwell's equations in linear media, using cosine-based phasors

$$\nabla \times \mathbf{E} = -j\omega\mu\mathbf{H} \quad (2.1a)$$

$$\nabla \times \mathbf{H} = j\omega\epsilon\mathbf{E}. \quad (2.1b)$$

Low-loss dielectrics are assumed and conductivity is incorporated into the dielectric constant:  $\epsilon = \epsilon' - j\sigma/\omega$ . The wave equation follows directly from Eqs. (2.1)

$$\nabla^2 \mathbf{H} + \omega^2 \mu \epsilon \mathbf{H} = 0. \quad (2.2)$$

Electromagnetic waves will propagate only in the transverse-magnetic (TM) mode up to frequencies far above 1 THz in micron-dimension waveguides. Assuming no variation in the  $y$ -direction, the H-field is purely  $y$ -directed. The H-field for the  $n^{\text{th}}$  layer is then,

$$\mathbf{H}_n = \hat{y} \left[ H_{++n} e^{-j(k_{xn}x + k_z z)} + H_{+-n} e^{-j(k_{xn}x - k_z z)} + H_{-+n} e^{j(k_{xn}x - k_z z)} + H_{--n} e^{j(k_{xn}x + k_z z)} \right] \quad (2.3)$$

where  $H$  represents the wave component amplitude,  $k_{xn}$  is the transverse propagation constant in the  $n^{\text{th}}$  layer, and  $k_z$  is the longitudinal propagation constant.  $k_n^2 \equiv \omega^2 \mu_n \epsilon_n = k_{xn}^2 + k_z^2$  is the dispersion relation. The transverse wave impedance of the  $n^{\text{th}}$  layer is  $\eta_{xn} = k_{xn} / \omega \epsilon_n$ . The electric fields are found directly from (2.1b).

A set of waves in the form of (2.3) satisfying the boundary conditions of the structure will propagate longitudinally (in the  $z$ -direction) and resonate transversely (in the  $x$ -direction). The transverse resonance condition is used to find the longitudinal propagation constant,  $k_z$ , which characterizes the mode. Methods from mathematically equivalent, and perhaps more familiar, transmission line theory apply, and the problem can be analyzed using the transmission line circuit analog shown in Fig. 2.3(b).

The net impedance of the metal-air layers is reduced to a simple expression by assuming the wave impedance in the metal is much less than the transverse wave impedance in air,  $\eta_m = \sqrt{j\omega\mu_0/\sigma_m} \ll \eta_{x0}$  [1]. The transverse wave impedance of the metal-air layers is then given by

$$\eta_{xm0} \approx \eta_m \coth \left[ (1+j) \frac{d_m}{\delta_{sm}} \right] \quad (2.4)$$

where  $\delta_{sm} = \sqrt{2/\omega\mu_0\sigma_m}$  is the skin depth in the metal.  $\eta_{xm0} \rightarrow 1/\sigma_m d_m$  at low frequencies, and  $\eta_{xm0} \rightarrow \eta_m$  at high frequencies.

At transverse resonance, the sum of the transverse wave impedances in both directions, measured anywhere, is zero. The transverse resonance condition,  $\eta_{x+} + \eta_{x-} = 0$ , is

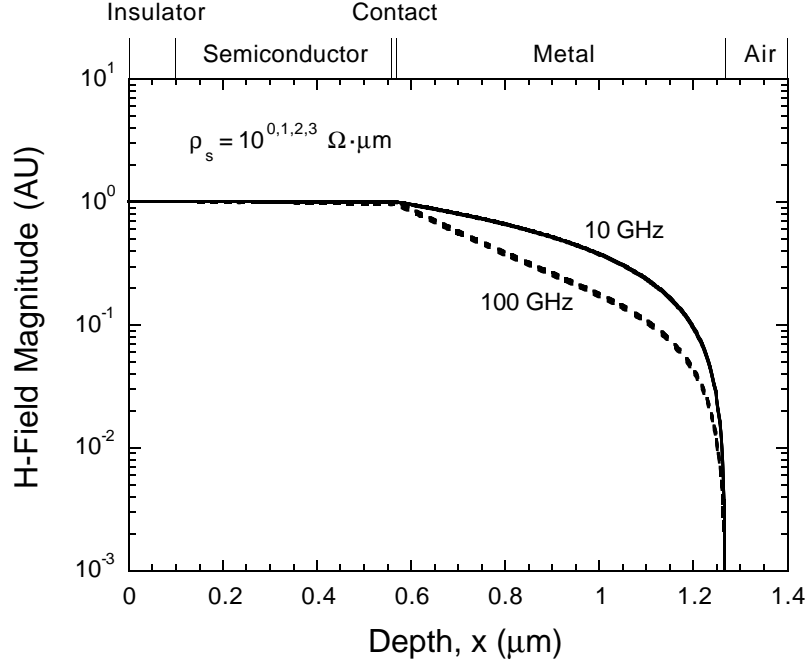


Fig. 2.4 Magnetic field distribution in a parallel-plate TWPD at 10 GHz and 100 GHz for a range of semiconductor layer resistivities of 1 to 1,000  $\Omega \cdot \mu\text{m}$ . The traces are coincident for all of the plotted semiconductor layer resistivities.

$$\eta_{xc} \frac{\eta_{xm0} + j\eta_{xc} \tan(k_{xc} d_c)}{\eta_{xc} + j\eta_{xm0} \tan(k_{xc} d_c)} + j\eta_{xs} \frac{\eta_{xi} \tan(k_{xi} d_i/2) + \eta_{xs} \tan(k_{xs} d_s)}{\eta_{xs} - \eta_{xi} \tan(k_{xi} d_i/2) \tan(k_{xs} d_s)} = 0. \quad (2.5)$$

This equation is solved numerically for  $k_z$  via the dispersion relation. A Matlab program that solves (2.5) and computes the fields and propagation characteristics is listed in Appendix A [18]. The electrical phase velocity and field attenuation constant are found from the real and imaginary parts of  $k_z$ . A waveguide width is assumed for the characteristic impedance, which is directly proportional to  $k_z$ . The waveguide dimensions are chosen such that a one micron wide waveguide will have a characteristic impedance of about 50 ohms.

Field distributions in the waveguide are plotted in Figs. 2.4 – 2.6. The H-field magnitude at 10 GHz and 100 GHz is plotted in Fig. 2.4. This plot shows that most of the current is carried in the metal layers, although the penetration into the metal decreases with increasing frequency. The current in the semiconductor layers

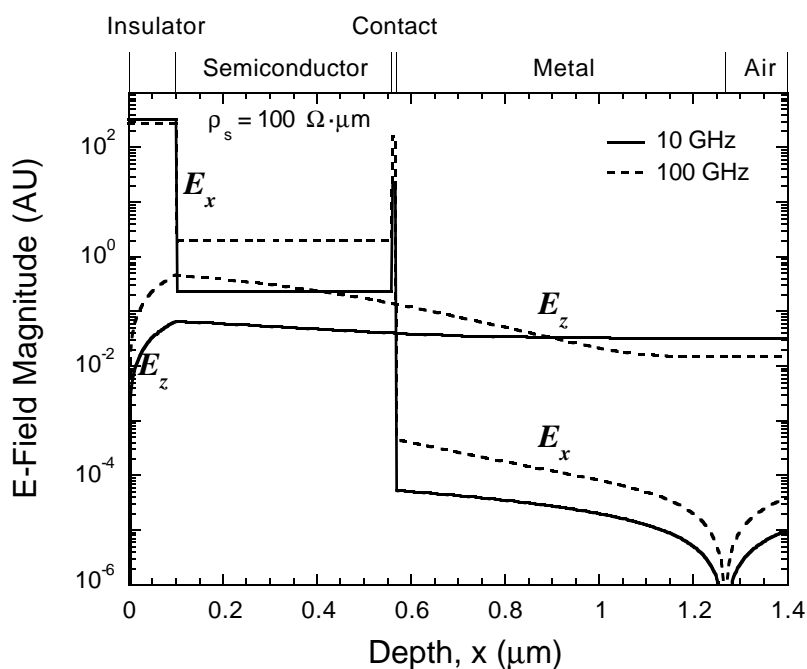


Fig. 2.5 Electric field components in a parallel-plate TWPD at 10 GHz and 100 GHz for semiconductor layer resistivity of  $100 \Omega \cdot \mu\text{m}$ .

increases slightly with frequency. Varying the resistivity of the semiconductor layers over three orders of magnitude produces little effect on the overall current distribution in the device.

The magnitudes of both E-field components at 10 GHz and 100 GHz are plotted in Fig. 2.5 for a semiconductor resistivity of  $100 \Omega \cdot \mu\text{m}$ , which is a typical resistivity for heavily doped semiconductor. Most of the voltage is supported by the insulator layer, although the transverse fields in the semiconductor and metal layers increase with increasing frequency. The longitudinal fields in the insulator and semiconductor layers also increase with increasing frequency. The change in longitudinal fields in the metal layers reflects the changing current distribution inferred from Fig. 2.4. Fields in the semiconductor and metal layers produce longitudinal and transverse currents, causing attenuation on the waveguide.

Fig. 2.6 shows the E-field components at 100 GHz for various semiconductor resistivities. The x-component in the semiconductor approaches the value in the metal as the resistivity is decreased, as expected. The z-component doesn't change

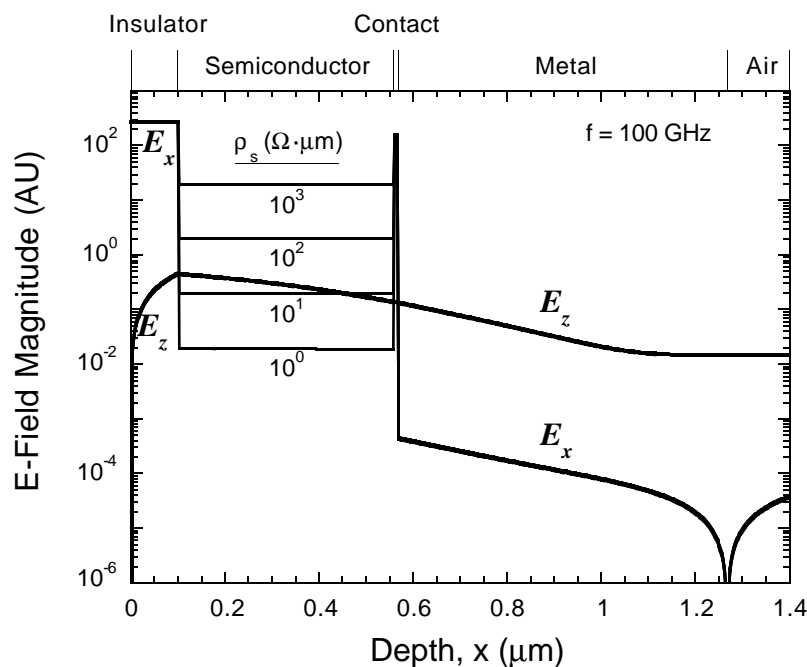


Fig. 2.6 Electric field components in a parallel-plate TWPD at 100 GHz for semiconductor layer resistivities of 1 to 1,000  $\Omega\cdot\mu\text{m}$ .

significantly with semiconductor resistivity. Note that the x- and z-components are nearly equal in the semiconductor layers when the semiconductor resistivity is about 10  $\Omega\cdot\mu\text{m}$ . This is approximately a point of minimum attenuation, evident in the plot of field attenuation constant versus semiconductor resistivity in Fig. 2.7. Also shown for comparison are plots of the attenuation constant of a waveguide with perfect metal rather than gold, and of a gold MIM (metal-insulator-metal) waveguide.

## 2.2 Equivalent-Circuit Model

The fact that  $E_x$  is much larger than  $E_z$  in the insulator, across which most of the voltage appears, together with the fact that the mode is TM establish that propagation on the TWPD is approximately transverse-electromagnetic, or quasi-TEM. A transmission line equivalent-circuit model accurately describes the properties of a quasi-TEM waveguide.

Such a circuit for a TWPD is shown in Fig. 2.8, and the element values for a parallel-plate TWPD are listed in Table 2.1. Fig. 2.8(a) shows the physical origins of

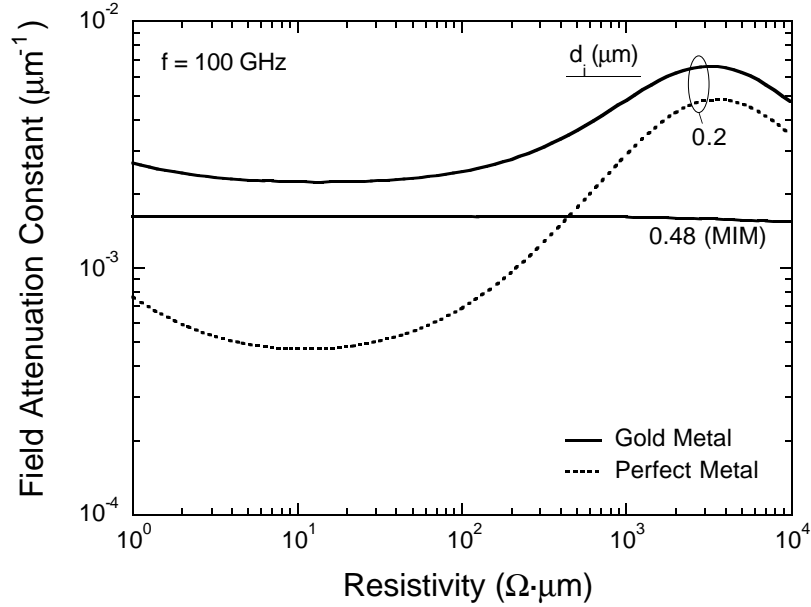


Fig. 2.7 Field attenuation constant as a function of semiconductor layer resistivity at 100 GHz. Curves for gold and perfect conductor metal layers with insulator layer thicknesses of  $0.2 \mu\text{m}$  and a gold metal-insulator-metal (MIM) waveguide with insulator layer thickness of  $0.48 \mu\text{m}$  (giving characteristic impedance of  $50 \Omega$  for a  $1 \mu\text{m}$  wide waveguide) are shown.

the circuit elements. Conduction and displacement currents in the contact and semiconductor layers are accounted for by resistances in parallel with capacitances, as shown in Fig. 2.8(b). At frequencies far below the dielectric relaxation frequencies of the contact and semiconductor layers ( $\omega\rho_c\epsilon_c \ll 1$  and  $\omega\rho_s\epsilon_s \ll 1$ ), the i-layer capacitance dominates the overall transmission line capacitance. While the i-layer capacitance is inversely proportional to the i-layer thickness,  $d_i$ , the inductance per unit length is proportional to the overall thickness,  $D$ . These dependencies on different thicknesses reflect the spatial separation of voltage and current that results in a slow phase velocity and low characteristic impedance.

The z-component of the E-field in the metal layers is much larger than the x-component from Figs. 2.5 and 2.6, so the wave in the metal is nearly transverse. Thus, the transverse wave impedance of the metal-air layers expressed in (2.4) also is the metal impedance listed in Table 2.1 for the equivalent circuit. The parallel

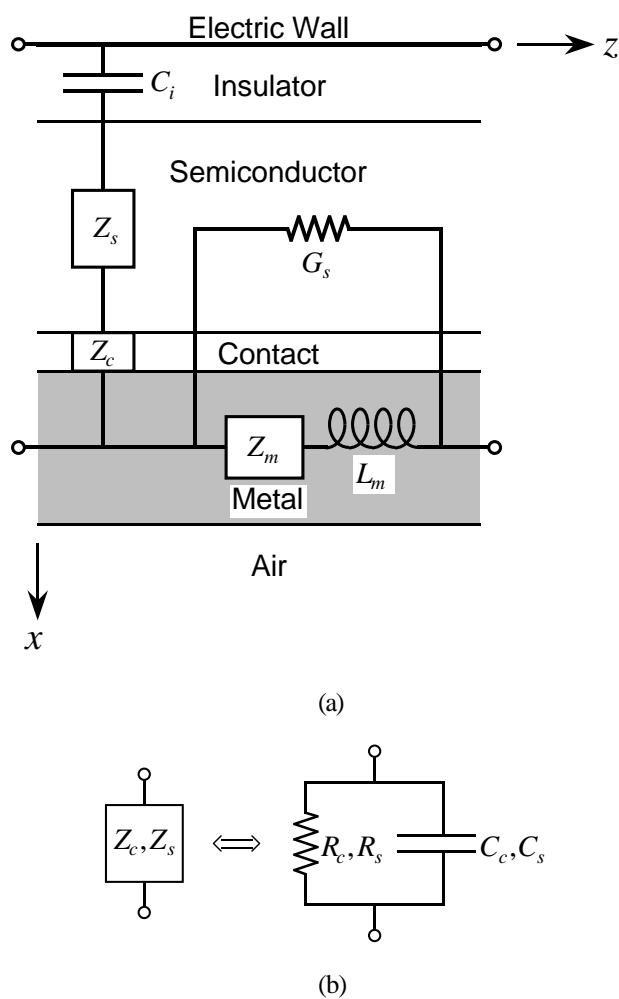


Fig. 2.8 TWPD equivalent-circuit models for (a) transmission line characteristics and (b) semiconductor and contact layer impedances. Circuit elements are identified with their associated layers from Fig. 2.3. Element values for a parallel-plate TWPD are listed in Table 2.1.

conductance of the semiconductor layers,  $G_s$ , includes a divisor of three to account for the current distribution in the semiconductor layers [3].

The transmission line propagation characteristics may be found by comparing the equivalent-circuit model of Fig. 2.8 to the general transmission line equivalent-circuit model of Fig. 2.9. Coupled differential equations for voltage and current wave propagation are written in terms of series impedance,  $Z$ , and shunt admittance,  $Y$ , per unit length of transmission line

$$Z_c = \frac{\rho_c}{1 + j\omega\rho_c\epsilon_c} \cdot \frac{2d_c}{w} \quad Z_m = \eta_{xm0} \frac{2}{w}$$

$$Z_s = \frac{\rho_s}{1 + j\omega\rho_s\epsilon_s} \cdot \frac{2d_s}{w} \quad G_s = \frac{\sigma_s}{3} \cdot \frac{wd_s}{2}$$

$$C_i = \epsilon_i \frac{w}{d_i} \quad L_m = \mu_0 \frac{D}{w}$$

Table 2.1 Parallel-plate TWPD element values for the equivalent-circuit model in Fig. 2.8.  $\rho$  is resistivity and  $\sigma = 1/\rho$  is conductivity;  $\epsilon$  and  $\mu$  are permittivity and permeability. The metal-air transverse wave impedance,  $\eta_{xm0}$ , is defined Fig. 2.3(b) and expressed in Eq. (2.4). The dimensions are indicated in Figs. 2.1 and 2.3(a).

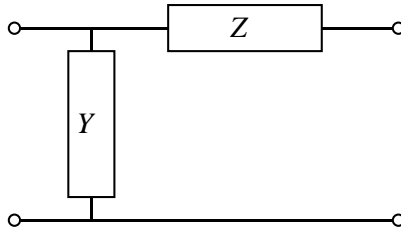


Fig. 2.9 General transmission line equivalent-circuit model.

$$\frac{dV}{dz} = -IZ \quad (2.6a)$$

$$\frac{dI}{dz} = -VY. \quad (2.6b)$$

These equations lead directly to the wave equation,

$$\frac{d^2V}{dz^2} = \gamma^2 V \quad (2.7)$$

where

$$\gamma = \sqrt{YZ} = \alpha_e + j\beta \quad (2.8)$$

is the complex propagation constant of the general solution,  $V(z) = V_0^+ e^{-\gamma z} + V_0^- e^{\gamma z}$ . Microwave loss and propagation velocity are found directly from the field attenuation

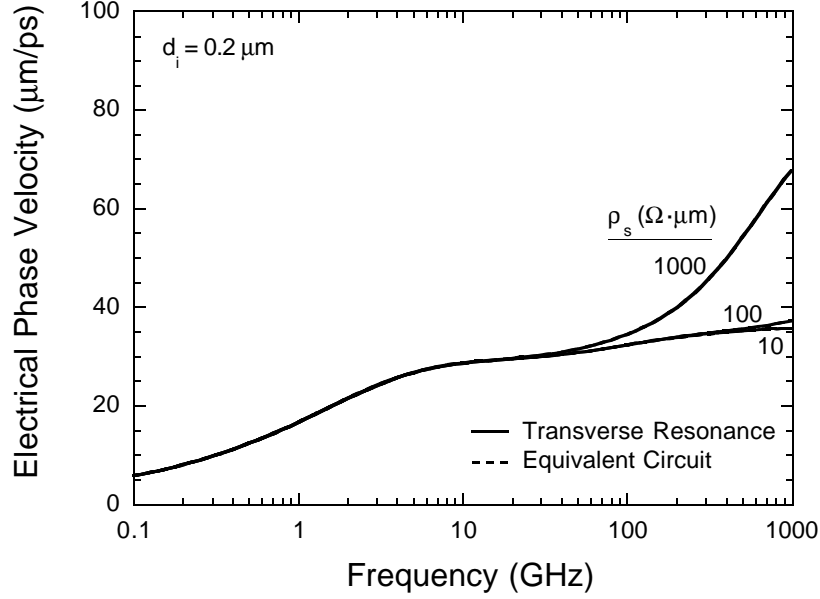


Fig. 2.10 Parallel-plate TWPD electrical velocity vs. frequency from transverse resonance solution and equivalent circuit model for semiconductor layer resistivities of 10, 100, and 1000  $\Omega\cdot\mu\text{m}$ . The full thickness of the insulator layer is 0.2  $\mu\text{m}$ .

constant,  $\alpha_e$ , and the propagation or phase constant,  $\beta$ . The voltage and current waves propagating on the transmission line are related by the characteristic impedance,

$$Z_0 = \sqrt{Z/Y}. \quad (2.9)$$

The electrical wave velocity, field attenuation constant, and characteristic impedance calculated from the equivalent-circuit model are compared with those from the transverse resonance solution in Figs. 2.10 – 2.12 for semiconductor resistivities of 10, 100, and 1000  $\Omega\cdot\mu\text{m}$ . Complex impedances for the contact and semiconductor layers in the equivalent-circuit model enable excellent accuracy for the propagation constant to beyond 1 THz. The equivalent-circuit model predicts characteristic impedance very well, also, aside from some deviation at high frequencies in the  $\rho_s = 1000 \Omega\cdot\mu\text{m}$  traces. The equivalent-circuit model accuracy shown in these plots holds with variations in the insulator layer thickness, as well. Thus, the equivalent-circuit model can be considered accurate to 1 THz for the structures of interest here.

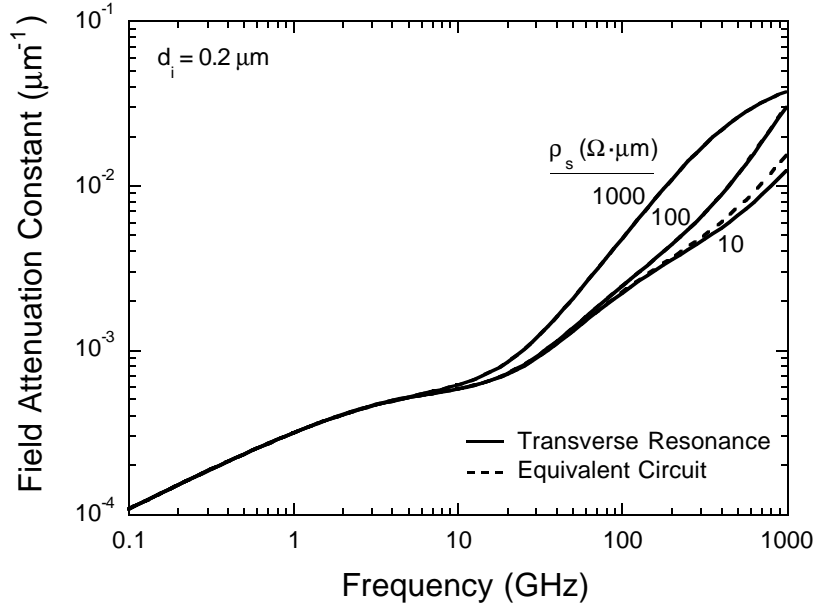


Fig. 2.11 Parallel-plate TWPD field attenuation constant, comparing transverse resonance solution and equivalent circuit model.

Further analysis from the equivalent-circuit model yields some insight into the behavior seen in Figs. 2.10 – 2.12. Assuming the metal conductivity is large compared to the parallel conductance of the semiconductor layers,  $GZ_m \ll 1$ , some simple expressions for the propagation characteristics can be written.

At frequencies far below the dielectric relaxation frequencies of the contact and semiconductor layers, the impedances of those layers are real and it is convenient to represent them as a resistor  $R = R_c + R_s$ . In this frequency range, the transmission line equivalent circuit for the TWPD reduces to that in Fig. 2.13, ignoring the current sources.

At very low frequencies ( $\omega RC \ll 1$ ,  $\omega GL \ll 1$ , and  $\omega L/Z_m \ll 1$ ), the complex propagation constant and characteristic impedance are given by

$$\gamma \approx \sqrt{\frac{\omega Z_m C}{2}}(1 + j) \quad (2.10)$$

$$Z_0 \approx \sqrt{\frac{Z_m}{2\omega C}}(1 - j). \quad (2.11)$$

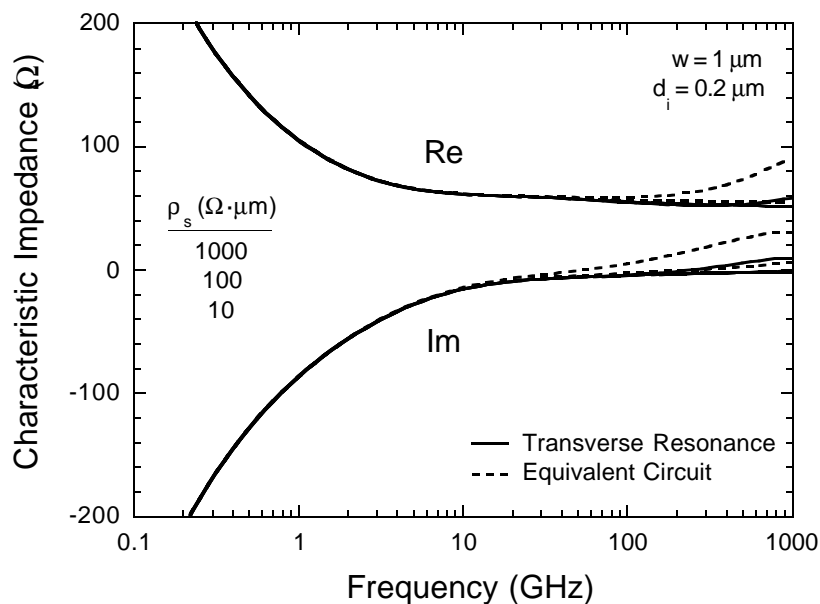


Fig. 2.12 Characteristic impedance of a 1  $\mu\text{m}$  wide, parallel-plate TWPD from transverse resonance solution and equivalent circuit model.

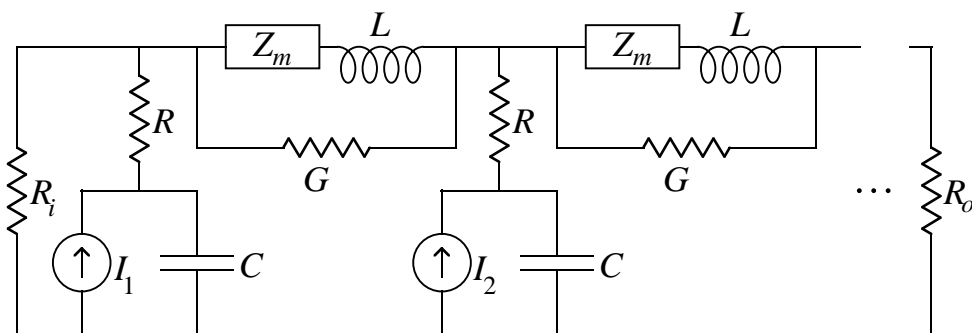


Fig. 2.13 TWPD equivalent-circuit diagram.

The corresponding frequency range in the plots is below about 1 GHz. The highly dispersive propagation in this range is characteristic of diffusion. This is typical of transmission lines at very low frequencies due to the dominance of the metal impedance.

The propagation characteristics in the mid-frequency range ( $\omega RC \ll 1$ ,  $\omega GL \ll 1$ , and  $\omega L/Z_m \gg 1$ ) are of greatest interest for TWPDs, since the device bandwidth falls in this range. The complex propagation constant can be written

$$\gamma \approx \frac{\omega^2}{2v_e} (RC + GL) + j \frac{\omega}{v_e} \quad (2.12)$$

where  $v_e \equiv \omega/\beta = 1/\sqrt{LC}$ . The loss is proportional to the square of frequency, and consists of terms proportional to  $RC$  and  $GL$ . The minimum in Fig. 2.7 occurs when  $RC = GL$ . The characteristic impedance is

$$Z_0 \approx R_0 \left[ 1 + j \frac{\omega}{2} (RC - GL) \right] \quad (2.13)$$

where  $R_0 \equiv \sqrt{L/C}$ . The effect of  $RC$  and  $GL$  on the characteristic impedance is to add a small reactance, which disappears when  $RC = GL$ . Notice that the metal impedance does not significantly affect the propagation characteristics when  $\omega L/Z_m \gg 1$ .

The mid-frequency range covers from about 10 GHz to several hundred gigahertz in Figs. 2.10 – 2.12. It is clear from (2.12) and (2.13) that the standard lossless transmission line equations for phase velocity and characteristic impedance,

$$v_e = 1/\sqrt{LC} \quad (2.14)$$

$$Z_0 = \sqrt{L/C} \quad (2.15)$$

are good approximations for TWPDs over this frequency range.

At high frequencies, the more detailed transmission line equivalent-circuit model of Fig. 2.8 applies, given the semiconductor layer is much thinner than its skin depth. This is true up to 1 THz for the TWPD designs considered here. Far above the dielectric relaxation frequencies of the contact and semiconductor layers ( $\omega \rho_c \epsilon_c \gg 1$  and  $\omega \rho_s \epsilon_s \gg 1$ ), the overall transmission line capacitance is the capacitance of all of the layers between the metal layers,  $C_m = (1/C_i + 1/C_s + 1/C_c)^{-1}$ , and the transverse resistance of those layers,  $R = R_c + R_s$ , is negligible. At high frequencies ( $\omega \rho_c \epsilon_c \gg 1$ ,  $\omega \rho_s \epsilon_s \gg 1$ , and  $\omega G_s L_m \ll 1$ ), the complex propagation constant and characteristic impedance are

$$\gamma \approx \frac{\omega^2}{2v_{em}} G_s L_m + j \frac{\omega}{v_{em}} \quad (2.16)$$

$$Z_0 \approx R_{0m} \left( 1 - j \frac{\omega}{2} G_s L_m \right) \quad (2.17)$$

where  $v_{em} \equiv 1/\sqrt{L_m C_m}$  and  $R_{0m} \equiv \sqrt{L_m/C_m}$ .

In the high frequency regime, the voltage and current are not spatially separated, so the phase velocity and characteristic impedance are not low, as they are at lower frequencies. Additionally, the attenuation is lower due to the elimination of the  $RC$  term in the attenuation constant. These effects explain the different trends of the  $\rho_s = 1000 \text{ } \Omega \cdot \mu\text{m}$  traces in Figs. 2.10 – 2.12 above a few hundred gigahertz. Characteristics of this mode are similar to those of TEM propagation in a lossy dielectric, so it is sometimes called the dielectric quasi-TEM mode [1, 2].

### 2.3 Velocity-Mismatch Impulse Response

The TWPD is a length of matched transmission line with a position-dependent photocurrent source distributed along its length, as represented by the equivalent-circuit diagram in Fig. 2.13. The TWPD velocity-mismatch impulse response is determined by the mismatch between optical group velocity and electrical phase velocity, and by the optical absorption coefficient [19]. In contrast, the RC bandwidth limitation of a lumped-element device, such as a WGPD, is determined by the total junction area [20]. The TWPD characteristic impedance is matched to the load impedance, so electrical waves are not reflected at the load as they are in lumped-element devices. This gives the TWPD a distinct impulse response that is essentially independent of device length.

The velocity mismatch is generally very large in a fully distributed TWPD because electrical waves propagate in the slow-wave mode over the frequency range of interest, as explained in Sections 2.1 and 2.2. The optical group and electrical phase velocities in a TWPD are mismatched by a factor of about 3:1 over the  $i$ -layer thickness range for 100-200 GHz bandwidth operation, as highlighted in the plot of Fig. 2.14. Light is absorbed in the  $i$ -layer, generating electrical waves, as the optical wave propagates on the structure. The impulse response resulting from these effects,

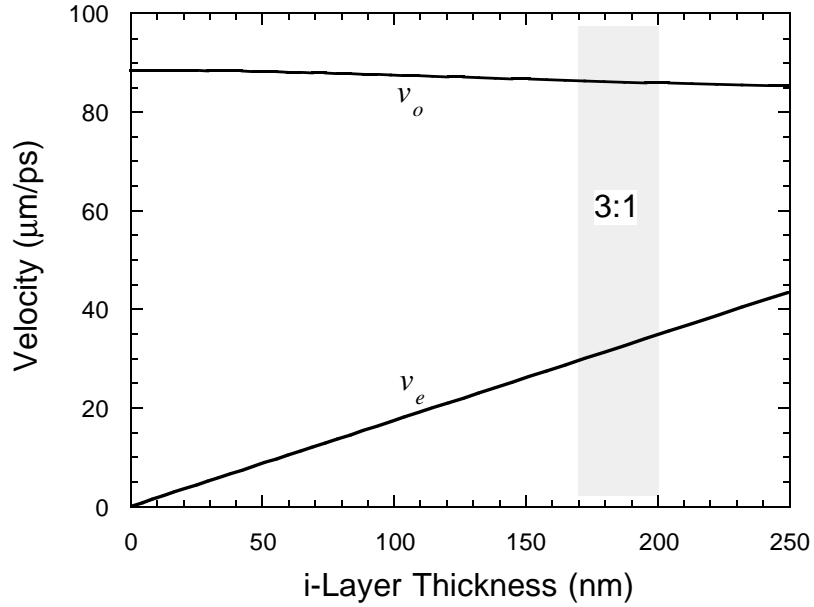


Fig. 2.14 Electrical phase velocity and optical group velocity calculated for a GaAs/AlGaAs parallel-plate TWPD.

and no others, is derived here. Accordingly, the carrier transit times are assumed to be zero.

Consider an impulsive packet of photons travelling in the semiconductor waveguide of a TWPD. The density of photons is given by

$$n_{ph}(z, t) = N_{ph}(z) \delta(z - v_o t) \quad (2.18)$$

where  $N_{ph}$  is the photon number,  $\delta$  is the Dirac delta function, and  $v_o$  is the optical group velocity. The probability of loss of a photon by linear mechanisms such as absorption and scattering is a constant, independent of position, so the change in photon number with distance is proportional to the photon number,  $dN_{ph}(z)/dz = -\Gamma \alpha N_{ph}(z)$ . The photon number then decays exponentially in the device according to  $N_{ph}(z) = N_{ph}(0) e^{-\Gamma \alpha z}$ , where  $\Gamma$  is the optical waveguide confinement factor, and  $\alpha$  is the i-layer material optical power absorption coefficient, which includes all linear loss mechanisms (presumably dominated by absorption with the generation of electron-hole pairs).

There is a direct correspondence between the absorption of photons and the generation of e-h pairs. The density of photogenerated e-h pairs is proportional to the distance rate of change of the photon number,  $n_{eh}(z) = -\eta_i dN_{ph}(z)/dz u(z)$ , where  $\eta_i$  is the fraction of lost photons generating e-h pairs that are collected, and  $u$  is the unit step function. The density of photogenerated e-h pairs is then simply  $n_{eh}(z) = \Gamma\alpha\eta_i N_{ph}(0)e^{-\Gamma\alpha z}u(z)$ .

Electrical waves propagate in both directions on the waveguide, originating from the travelling photocurrent source. Presently assume that the electrical phase velocity is very much smaller than the optical group velocity,  $v_e \ll v_o$ , so the optical impulse passes entirely through the device before the electrical waves have moved a significant distance. The charge density profile of the electrical waves when the optical wave has reached the end of the device is  $\rho(z) = Q\Gamma\alpha e^{-\Gamma\alpha z}u(z)$ , where  $Q = N_{ph}(0)\eta_i q$  is the total charge available in the optical impulse. The total forward-going charge density wave is composed of the wave that originally was forward-travelling, plus the wave that started out reverse-travelling and was reflected at the device input end,

$$\rho(z,t) = \frac{Q}{2} \left[ \Gamma\alpha e^{-\Gamma\alpha(z-v_e t)} u(z-v_e t) + \gamma \Gamma\alpha e^{\Gamma\alpha(z-v_e t)} u(v_e t - z) \right] \quad (2.19)$$

where  $\gamma$  is the electrical reflection coefficient at the device input end.

The current at the device output is the total forward-going charge density wave profile times the electrical velocity

$$i\left(t + \frac{\ell}{v_e}\right) = \rho\left(z, t + \frac{z}{v_e}\right) v_e. \quad (2.20)$$

Substituting (2.19) into (2.20) gives an expression for the current impulse response of a TWPD due to velocity mismatch for  $v_e \ll v_o$ ,

$$i\left(t + \frac{\ell}{v_e}\right) = \frac{Q}{2} \left[ \Gamma\alpha v_e e^{\Gamma\alpha v_e t} u(-t) + \gamma \Gamma\alpha v_e e^{-\Gamma\alpha v_e t} u(t) \right]. \quad (2.21)$$

To consider the case when the electrical velocity is not much smaller than the optical velocity, it is helpful to start in an inertial frame of reference of an electrical wave. The equation for the total forward-going charge density wave is of the same form as (2.19) when viewed in the forward-going electrical wave frame of reference,

$$\rho(z', t) = \frac{Q}{2} \left[ \Gamma \alpha' e^{-\Gamma \alpha' z'} u(z') + \gamma \Gamma \alpha'' e^{\Gamma \alpha'' z'} u(-z') \right] \quad (2.22)$$

where  $z' = z - v_e t$ ,  $\alpha' = \alpha / (1 - v_e / v_o)$ , and  $\alpha'' = \alpha / (1 + v_e / v_o)$ . Converting back to the device rest frame gives the forward-travelling charge density wave

$$\rho(z, t) = \frac{Q}{2} \left[ \frac{\Gamma \alpha}{1 - v_e / v_o} e^{-\frac{\Gamma \alpha}{1 - v_e / v_o} (z - v_e t)} u(z - v_e t) + \gamma \frac{\Gamma \alpha}{1 + v_e / v_o} e^{\frac{\Gamma \alpha}{1 + v_e / v_o} (z - v_e t)} u(v_e t - z) \right] \quad (2.23)$$

Inserting (2.23) into (2.20) and accounting for the (unusual) case when  $v_e > v_o$ , gives the desired expression for the TWPD velocity-mismatch impulse response,

$$i_{vm} \left( t + \frac{\ell}{v_e} \right) = \frac{Q}{2} \left[ \omega_f e^{\omega_f t} u(-\omega_f t) + \gamma \omega_r e^{-\omega_r t} u(t) \right] \quad (2.24)$$

for  $\min(\ell / v_o, \ell / v_e) \leq t \leq \ell / v_o + 2\ell / v_e$  and zero elsewhere, and

$$\omega_f = \Gamma \alpha v_e / (1 - v_e / v_o) \quad (2.25a)$$

$$\omega_r = \Gamma \alpha v_e / (1 + v_e / v_o) \quad (2.25b)$$

are characteristic frequencies of the forward and reverse waves. Equation (2.24) is a general description of the current response of a TWPD to an optical impulse applied at its input considering only velocity mismatch.

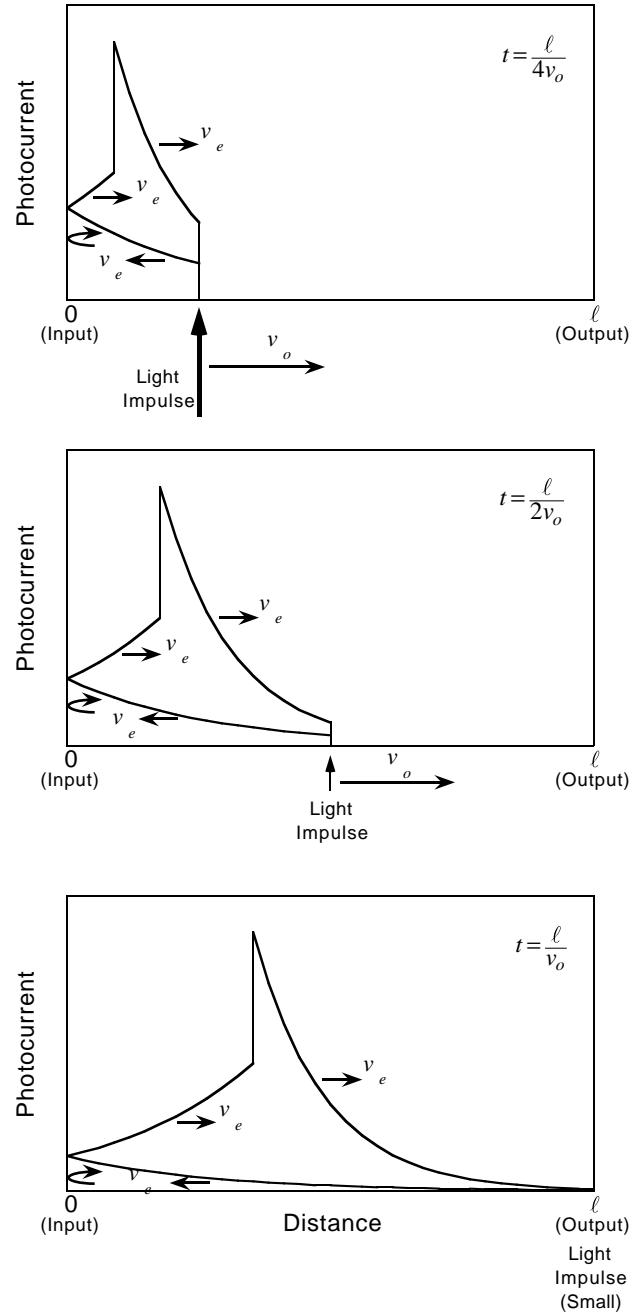


Fig. 2.15 Spatial plots of the velocity-mismatch impulse response when the light impulse is at  $\ell/4$  (top plot), in the middle (center plot), and at the output end (bottom plot) of a TWPD with open-circuit input termination.

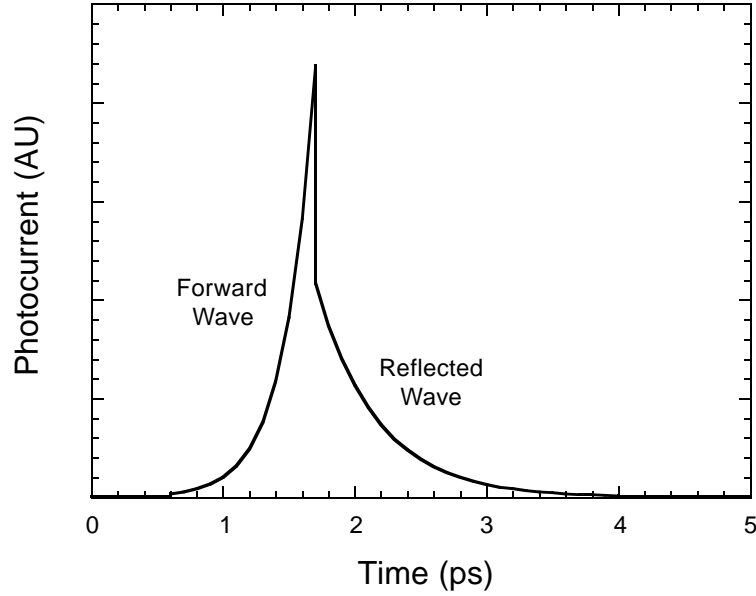


Fig. 2.16 Velocity mismatch impulse response of a TWPD with open-circuit input termination for  $v_o = 86 \mu\text{m/ps}$ ,  $v_e = 29 \mu\text{m/ps}$ ,  $\Gamma\alpha = 0.1 / \mu\text{m}$ , and  $\ell = 50 \mu\text{m}$ .

Fig. 2.15 depicts the propagation of a light impulse and the photogenerated electrical waves on a TWPD, showing the formation of the velocity-mismatch impulse response in space. The temporal velocity-mismatch impulse response from (2.24) is plotted in Fig. 2.16. The response is composed of two exponential components, which in general have different decay constants. Conservation of energy and charge require that the integral of the photocurrent response of an infinitely long TWPD with  $\gamma=1$  equal the total charge available in the optical pulse,  $Q = N_{ph}(0)\eta_i q = E_0 \eta_i q / h\nu$ , where  $E_0$  is the total energy in the optical impulse. Furthermore, conservation of momentum for the electrical waves dictates that the total charge be split equally between the forward- and reverse-travelling photocurrent components. As a result, the heights of these two components are generally different where they meet, forming a discontinuity in the photocurrent response at that point.

The velocity-mismatch impulse response can be made much shorter by placing a matched termination at the input end of the TWPD ( $\gamma = 0$ ). The reflected wave is then absorbed and only the first term in (2.24) remains. Half of the photocurrent is lost in

the termination, however, casting doubt on the value of this approach. This is best evaluated in the frequency domain.

#### 2.4 Velocity-Mismatch Bandwidth Limitation

The velocity-mismatch frequency response is the Fourier transform of the impulse response, (2.24). For long TWPDs, ( $\Gamma\alpha\ell \gg 1$ ), this is given by

$$i_{vm}(\omega) = \frac{Q}{2} \left[ \frac{\omega_f}{\omega_f - j\omega} + \gamma(\omega) \frac{\omega_r}{\omega_r + j\omega} \right] e^{-j\omega \frac{\ell}{v_e}}. \quad (2.26)$$

The fractional photocurrent magnitude frequency response for real values of  $\gamma$  is

$$\left| \frac{i_{vm}(\omega)}{Q} \right|^2 = \frac{1}{4} \cdot \frac{(\omega_f - \gamma\omega_r)^2 \omega^2 + (1 + \gamma)^2 \omega_f^2 \omega_r^2}{(\omega^2 + \omega_f^2)(\omega^2 + \omega_r^2)}. \quad (2.27)$$

In a TWPD with matched input termination ( $\gamma = 0$ ), only the forward-travelling wave contributes to the response since the reverse-travelling wave is absorbed in the input termination. The magnitude photocurrent response (2.27) for  $\gamma = 0$  reduces to the single-pole response,

$$\left| \frac{i_{vm0}(\omega)}{Q} \right|^2 = \frac{1}{4} \cdot \frac{1}{1 + (\omega/\omega_f)^2} \quad (2.28)$$

and the 3 dB bandwidth limitation is  $B_{vm0} = \omega_f/2\pi$ .

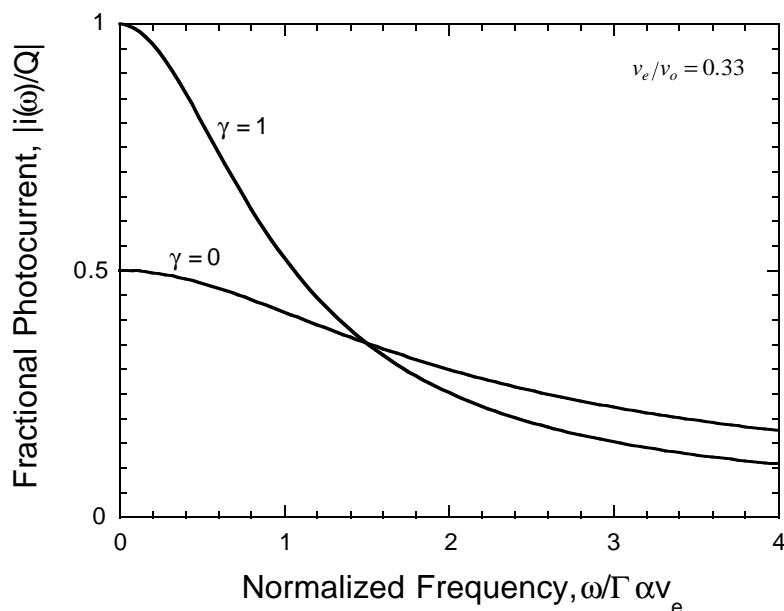


Fig. 2.17 Velocity mismatch frequency response for TWPDs with large velocity mismatch,  $v_e/v_o = 0.33$ , for open-circuit ( $\gamma = 1$ ) and matched ( $\gamma = 0$ ) input terminations.

Fig. 2.17 shows velocity-mismatch frequency response curves for a TWPD with a typical velocity mismatch,  $v_e/v_o = 0.33$ , for open-circuit ( $\gamma = 1$ ) and matched ( $\gamma = 0$ ) input terminations. The quantum efficiency of the device with matched input termination is limited to 50%. In this particular case, the  $\gamma = 1$  curve intersects the  $\gamma = 0$  curve at the -3 dB point of the  $\gamma = 0$  response, so the TWPD response with open-circuit input termination ( $\gamma = 1$ ) is larger than that of the TWPD with matched input termination ( $\gamma = 0$ ) over its entire bandwidth.

The TWPD with matched input termination ( $\gamma = 0$ ) has no bandwidth limitation in the velocity-matched case,  $v_e/v_o = 1$ , but is still limited to 50% efficiency, as shown in Fig. 2.18. The  $\gamma = 1$  curve is always above the  $\gamma = 0$  curve in this plot. The bandwidth of TWPDs are limited by other factors, also (discussed in Chapter 3), and the net bandwidth-efficiency product is generally worse in devices with matched input terminations [19].

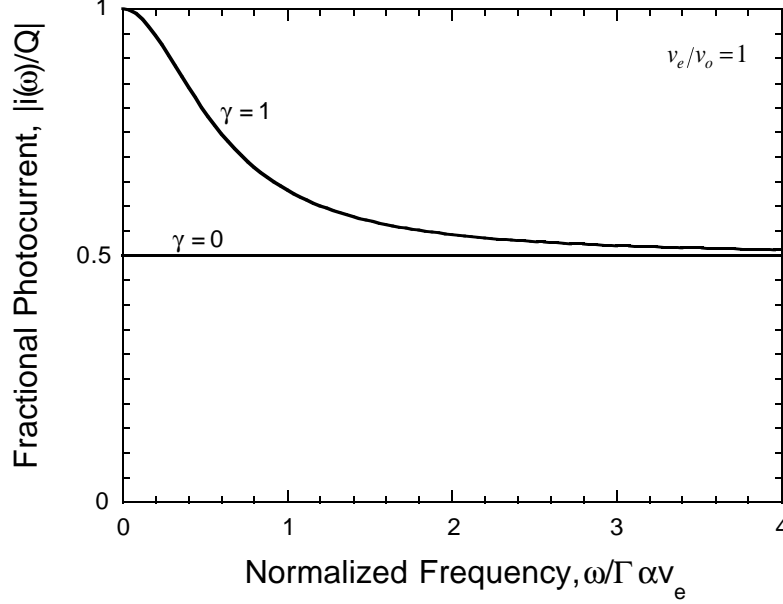


Fig. 2.18 Velocity mismatch frequency response for velocity matched ( $v_e/v_o = 1$ ) TWPDs for open-circuit ( $\gamma = 1$ ) and matched ( $\gamma = 0$ ) input terminations.

Comparing the  $\gamma = 1$  curves in Figs. 2.17 and 2.18, it appears that velocity matching has little effect on their 3 dB bandwidths. The bandwidth for positive real values of  $\gamma$  can be found by solving a quadratic equation for  $\omega_1$ ,

$$\omega_1^4 + \left[ \omega_f^2 + \omega_r^2 - \frac{2}{(1+\gamma)^2} (\omega_f - \gamma\omega_r)^2 \right] \omega_1^2 - \omega_f^2 \omega_r^2 = 0. \quad (2.29)$$

Fig. 2.19 confirms that the  $\gamma = 1$  curve is almost independent of velocity mismatch, while the  $\gamma = 0$  curve is strongly dependent.

The response of a  $\gamma = 1$  TWPD is composed of forward- and reverse-travelling waves. While velocity matching reduces the temporal duration of the forward-travelling wave, it stretches the reverse-travelling wave, so the overall duration of the  $\gamma = 1$  response changes little. The velocity-mismatch bandwidth limitation for a  $\gamma = 1$  TWPD is approximated by

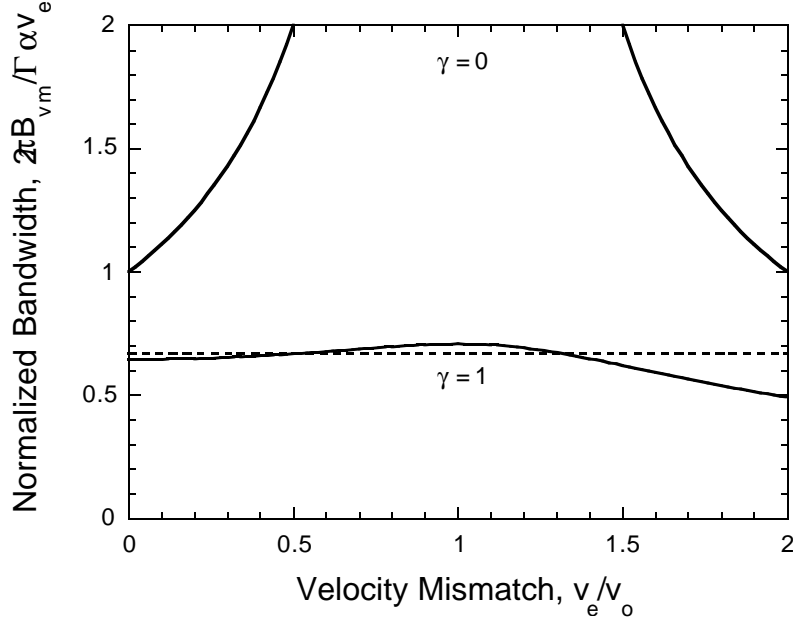


Fig. 2.19 Normalized bandwidth of  $\gamma = 1$  and  $\gamma = 0$  TWPDs versus velocity mismatch. The broken line shows a constant approximation ( $1/1.5$ ) to the  $\gamma = 1$  curve.

$$B_{vm1} \approx \frac{\Gamma \alpha v_e}{3\pi} \quad (2.30)$$

with less than 6% error over the entire range of velocities from completely mismatched to beyond matched,  $0 \leq v_e/v_o \leq 1.47$ . Note that (2.30) is independent of optical velocity. Increasing the electrical velocity increases the velocity-mismatch bandwidth limitation, but velocity-matching is surprisingly of almost no direct value. In fact, the mismatched case, where  $v_e/v_o > 1$ , is preferable to the matched case,  $v_e/v_o = 1$ .

The velocity-mismatch bandwidth limitation for  $\gamma = 1$  in (2.30) can be cast in a more familiar form by using (2.14) and (2.15),

$$B_{vm1} \approx \frac{1}{2\pi Z_0 C} \cdot \frac{\Gamma \alpha}{1.5}. \quad (2.31)$$

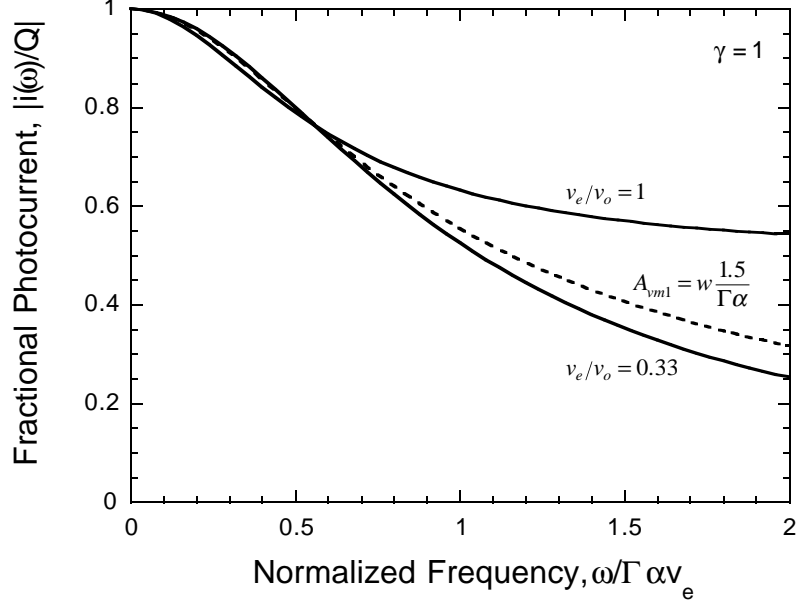


Fig. 2.20 Velocity mismatch frequency responses for  $\gamma = 1$  TWPDs. Effective area approximation (broken line) is compared with velocity matched ( $v_e/v_o = 1$ ) and velocity mismatched ( $v_e/v_o = 0.33$ ) responses.

Evidently, the  $\gamma = 1$  TWPD velocity-mismatch bandwidth limitation is comparable to the RC bandwidth limitation for a WGPD of fixed area,

$$A_{vm1} = w \frac{1.5}{\Gamma \alpha}. \quad (2.32)$$

In fact, this area can be used to approximate the frequency response up to the velocity-mismatch bandwidth limitation with less than 4% error, as illustrated in Fig. 2.20.

The effective area associated with the velocity-mismatch bandwidth limitation for  $\gamma = 1$  TWPDs is independent of length. The effective length,  $\ell_{vm1} = 1.5/\Gamma\alpha$ , would allow only 78% internal quantum efficiency in a WGPD of the same bandwidth. However, the TWPD can be made physically much longer to achieve close to 100% internal quantum efficiency without sacrificing bandwidth.

The velocity-mismatch effective area for the  $\gamma = 0$  TWPD,

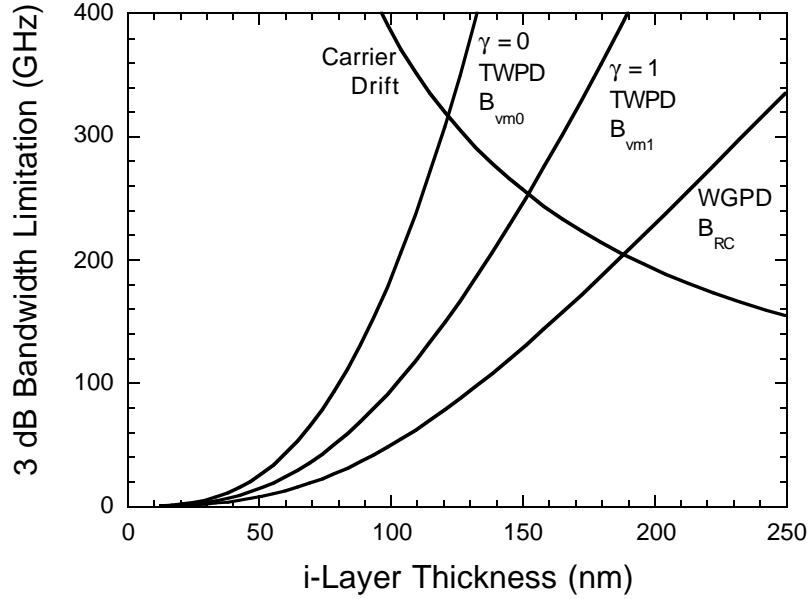


Fig. 2.21 Primary bandwidth limitation of 1  $\mu\text{m}$  wide, parallel-plate, GaAs/AlGaAs p-i-n TWPDs and WGDs. Carrier drift, velocity mismatch, and RC limitations are shown. 100% and 95% internal quantum efficiencies are assumed for the TWPDs and WGDs. The load impedance is 50  $\Omega$ .

$$A_{vm0} = w \frac{1 - v_e/v_o}{\Gamma \alpha}. \quad (2.33)$$

gives the exact velocity-mismatch frequency response (2.28). This area depends strongly on velocity mismatch, and it goes to zero when the velocities are matched, corresponding to infinite bandwidth as shown in Fig. 2.18.

Fig. 2.21 shows the velocity mismatch bandwidth limitations for  $\gamma = 0$  and  $\gamma = 1$  TWPDs, the RC bandwidth limitation for a WGD with 95% internal quantum efficiency, and the carrier drift bandwidth limitation versus i-layer thickness [19]. The internal efficiency of both WGDs and TWPDs is reduced by optical scattering, free carrier loss, absorption outside the collection field, recombination in the active region, and electrical losses. These effects are deemed small and presently ignored. Fig. 2.21 suggests that the TWPDs have larger overall bandwidths than the WGD. Since the  $\gamma = 1$  TWPD has 100% internal quantum efficiency, it also has a larger bandwidth-efficiency product than the WGD.

In practice, TWPD overall bandwidth is found by replacing the device physical junction area in standard lumped-element calculations with the velocity-mismatch effective area in (2.32) or (2.33). This procedure is described in Chapter 3.

## 2.5 Space-Charge Field Screening

A performance metric closely related to the bandwidth-efficiency product is the range of photodetector response linearity. Both parameters are primary factors in system signal-to-noise performance. Field-screening is a fundamental mechanism that limits the range of photodetector linearity at high illumination. A simple model illustrates physical phenomena that mitigate field-screening effects in TWPDs.

Field screening arises when the dipole due to spatial separation of photogenerated charges significantly reduces the drift field, as illustrated conceptually in Fig. 2.22. The electric field in the depletion region (i-layer) is the sum of the built-in field, the field due to photogenerated free charge, and the fields of waves originating elsewhere and propagating on the structure,  $E = E_b + E_f + E_w$ . The free charge field is found by Gauss's law and is proportional to the charge area density,  $E_f = \int \rho_f / \epsilon dx \propto \sigma$ . For simplicity and clarity, the built-in field and the charge densities of the electrons and holes are approximated by rectangle functions in Fig. 2.22. The RC time constant is assumed zero, which is equivalent to ignoring the fields due to the propagating waves in a TWPD. This is a reasonable assumption for photodetectors with transit-time limited small-signal response.

Fig. 2.22 shows three sets of conceptual graphs at successive times after photogeneration of electrons and holes in the depletion region by a short optical pulse. The upper plots show the photogenerated charge density, and the lower plots show the net electric field in the depletion region. Electron and hole velocities are assumed equal. The field resulting from the separation of the free charges opposes the built-in field, and if the charge density is large enough, may actually cancel it, as shown in the third set of graphs. The carriers in the low-field region then travel slower, causing a slow component in the device photocurrent response. Field-screening is said to occur when the device response is perceptibly affected.

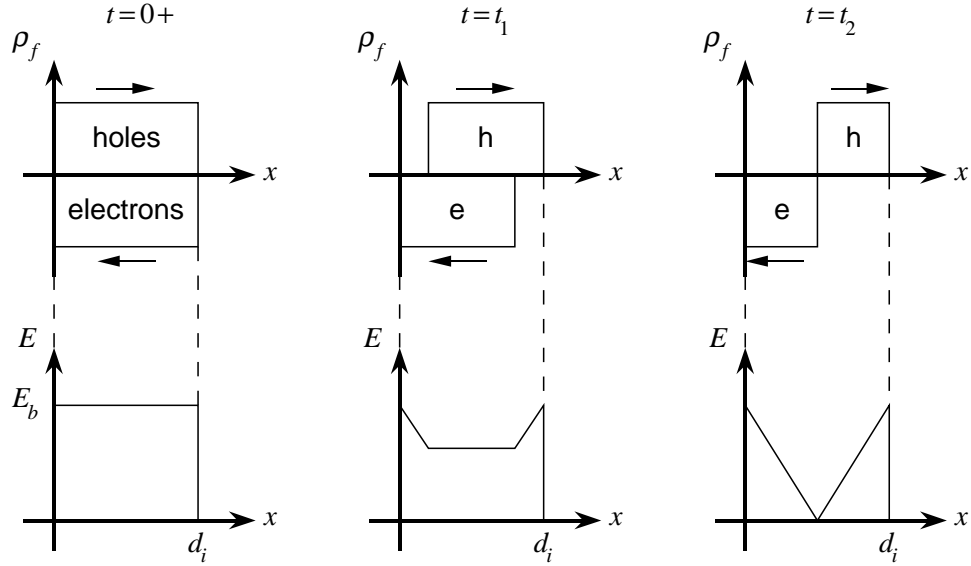


Fig. 2.22 Conceptual illustration of field-screening mechanism. Simplified electron and hole distributions and net electric fields in the depletion region are plotted at three times after photogeneration by a short optical pulse.

Charge build-up at the depletion region edges is ignored in Fig. 2.22, although it may be significant in RC-limited devices. Charge reaching the depletion region edges contributes to the circuit current on a time scale much shorter than the transit time in a transit-time limited photodetector, as assumed in Fig. 2.22. A device can always be made transit-time limited by lowering the load impedance. However, charge lingers at the depletion region edges in the RC-limited case, adding to the screening field. Thus, field-screening effects are more pronounced in an RC-limited device/circuit.

Local field screening occurs when the photogenerated charge area density at a point in the plane of the junction exceeds a critical value,  $\sigma(y,z) > \sigma_{fs}$ . The total charge,  $Q$ , at the field-screening threshold for a thin, uniformly illuminated, vertically illuminated photodetector (VPD) is then

$$Q_{fsV} = \sigma_{fs} A. \quad (2.34)$$

To first order, the photogenerated charge density profile in an in-plane illuminated photodetector, such as a TWPD or WGPD, decays exponentially according to

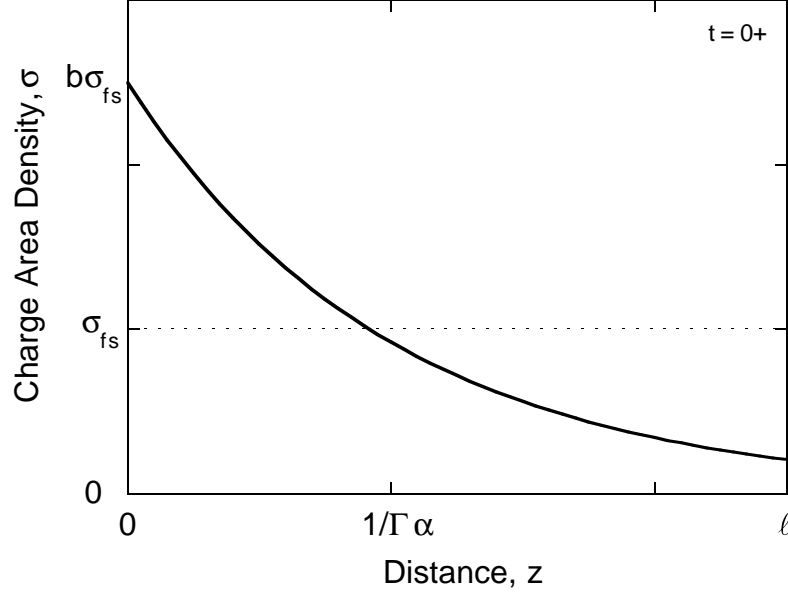


Fig. 2.23 First-order photogenerated charge density profile in an in-plane illuminated photodetector at its field-screening threshold. The dotted line indicates the local field-screening threshold density.

$$\sigma(z) = \sigma(0)e^{-\Gamma\alpha z}u(z) \quad (2.35)$$

as illustrated in Fig. 2.23. This nonuniform distribution gives rise to several phenomena that impact field-screening. These phenomena are accounted for by defining the field-screening threshold as the total charge when the density at the input according to (2.35) is above the threshold density by a factor  $b$ . For a TWPD, this is expressed in terms of the velocity-mismatch effective area

$$Q_{fsT} = \frac{b}{1.5} \sigma_{fs} A_{vm1}. \quad (2.36)$$

Fig. 2.24 outlines effects that impact  $b$ . The dashed line is the simple exponential as in Fig. 2.23. Nonlinear absorption, in which the absorption decreases with increasing volume density of electron-hole pairs, is depicted by the solid line. This effect reduces field screening, although it is compensated some by carrier heating in the drift field [21]. Charges in the unscreened regions are not affected by field

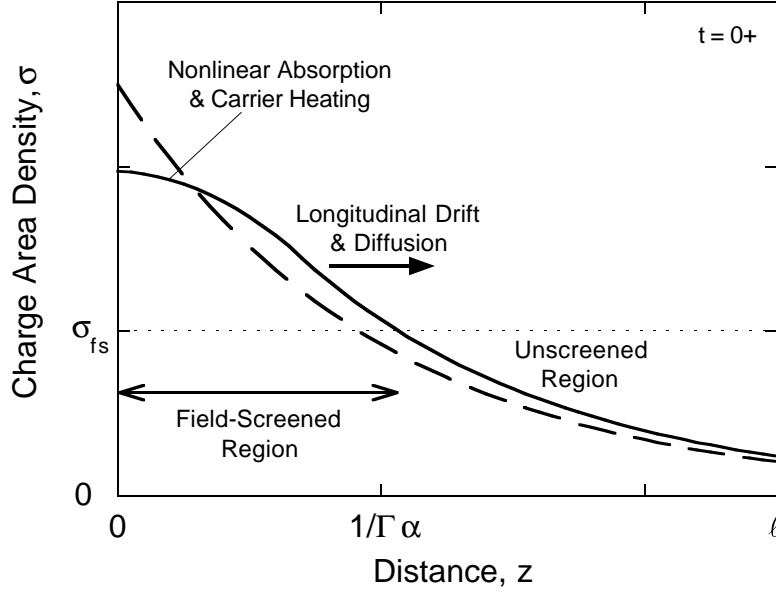


Fig. 2.24 Photogenerated charge density profile in an in-plane illuminated photodetector showing field-screened and unscreened regions, and illustrating effects of longitudinal drift and diffusion, nonlinear absorption, and carrier heating. The first-order exponential profile (dashed line) is also shown for comparison.

collapse elsewhere and are quickly swept out of the depletion region. Only the region of the photodetector where  $\sigma(z) > \sigma_{fs}$  has slowed response from field screening. Large field and carrier density gradients in the  $z$ -direction result in longitudinal drift and diffusion toward regions of higher drift field [22, 23]. This significantly reduces the effects of field screening.

The longitudinal drift and diffusion in a TWPD under high illumination effectively increase the area of the device. This is expressed by combining (2.34) and (2.36) for an effective area for the field-screening threshold of a TWPD,

$$A_{fsT} = \frac{b}{1.5} A_{vm1}. \quad (2.37)$$

The area that determines the field-screening threshold of a TWPD is not the same as the area that determines its bandwidth. In contrast, the two areas are identical in a VPD. Measurement results presented in Chapter 5 suggest that  $A_{fsT} > A_{vm1}$ .

Heating in a photodetector also limits its power handling. However, it is noteworthy that the fractional power dissipation in the load increases as the potential drop across the depletion region decreases. Thus, field-screening reduces heating in the photodetector. The power dissipated in the photodetector is simply expressed as

$$P = i \left( \frac{h\nu}{q} + V_{bias} \right) - i^2 R \quad (2.38)$$

assuming that all absorbed optical power produces photocurrent. The relationship between power dissipated in the photodetector and photocurrent is sub-linear. The power dissipated in the photodetector reaches a maximum value of  $P_{\max} = (h\nu/q + V_{bias})^2 / 4R$  at a photocurrent of  $i = (h\nu/q + V_{bias}) / 2R$ .

In this chapter, it is shown that a transmission line equivalent-circuit model accurately characterizes wave propagation on a parallel-plate TWPD structure. The velocity-mismatch impulse response is derived and the velocity-mismatch bandwidth limitation is quantified. The most important result of this chapter is the expression for velocity-mismatch effective area (2.32), which says that the effective area of a TWPD, defining an effective capacitance, is independent of the device length. This explains why TWPDs can be long for high internal quantum efficiency without sacrificing bandwidth. The last section describes field-screening effects in TWPDs. The theory presented in this chapter will be applied in designing a practical structure in the next chapter and in analyzing measurements presented in Chapter 5.

## References

- [1] H. Guckel, P. A. Brennan, and I. Palócz, "A Parallel-Plate Waveguide Approach to Microminiaturized, Planar Transmission Lines for Integrated Circuits," *IEEE Trans. Microwave Theory Tech.*, vol. 15, no. 8, pp. 468-476, Aug., 1967.
- [2] H. Hasegawa, M. Furukawa, and H. Yanai, "Properties of Microstrip Line on Si-SiO<sub>2</sub> System," *IEEE Trans. Microwave Theory Tech.*, vol. 19, no. 11, pp. 869-881, Nov., 1971.
- [3] D. Jäger, "Slow-Wave Propagation Along Variable Schottky-Contact Microstrip Line," *IEEE Trans. Microwave Theory Tech.*, vol. 24, no. 9, pp. 566-573, Sep., 1976.
- [4] Y. Fukuoka and T. Itoh, "Analysis of slow-wave phenomena in coplanar waveguide on a semiconductor substrate," *Electronics Letters*, vol. 18, no. 14, pp. 598-590, Jul. 8, 1982.

- [5] Y. Fukuoka, Y. C. Shih, and T. Itoh, "Analysis of Slow-Wave Coplanar Waveguide for Monolithic Integrated Circuits," *IEEE Trans. Microwave Theory Tech.*, vol. 31, no. 7, pp. 567-573, Jul., 1983.
- [6] R. Sorrentino, G. Leuzzi, and A. Silbermann, "Characteristics of Metal-Insulator-Semiconductor Coplanar Waveguides for Monolithic Microwave Circuits," *IEEE Trans. Microwave Theory Tech.*, vol. 32, no. 4, pp. 410-416, Apr., 1984.
- [7] C. K. Tzuang and T. Itoh, "Finite-Element Analysis of Slow-Wave Schottky Contact Printed Lines," *IEEE Trans. Microwave Theory Tech.*, vol. 34, no. 12, pp. 1483-1489, Dec., 1986.
- [8] T. G. Livernois and P. B. Katehi, "A Generalized Method for Deriving the Space-Domain Green's Function in a Shielded, Multilayer Substrate Structure with Applications to MIS Slow-Wave Transmission Lines," *IEEE Trans. Microwave Theory Tech.*, vol. 37, no. 11, pp. 1761-1767, Nov., 1989.
- [9] J. C. Liou and K. M. Lau, "A Solution to Characteristics of Planar Transmission Lines Made of Finite-Thickness Metal on Multi-Layer Media," in *1990 IEEE MTT-S Microwave Symposium Digest*, pp. 179-182, May 8-10, 1990.
- [10] K. Wu and R. Vahldieck, "Hybrid-Mode Analysis of Homogeneously and Inhomogeneously Doped Low-Loss Slow-Wave Coplanar Transmission Lines," *IEEE Trans. Microwave Theory Tech.*, vol. 39, no. 8, pp. 1348-1360, Aug., 1991.
- [11] J. P. K. Gilb and C. A. Balanis, "MIS Slow-Wave Structures Over a Wide Range of Parameters," *IEEE Trans. Microwave Theory Tech.*, vol. 40, no. 12, pp. 2148-2154, Dec., 1992.
- [12] J. C. Liou and K. M. Lau, "Analysis of Slow-Wave Transmission Lines on Multi-Layered Semiconductor Structures Including Conductor Loss," *IEEE Trans. Microwave Theory Tech.*, vol. 41, no. 5, pp. 824-829, May, 1993.
- [13] C. Seguinot, P. Kennis, P. Pribetich, J. F. Legier, "Analytical Model of the Schottky Contact Coplanar Line," in *Proc. 14th European Microwave Conf.*, pp. 160-165, Sep., 1984.
- [14] Y. R. Kwon, V. M. Hietala, and K. S. Champlin, "Quasi-TEM Analysis of "Slow-Wave" Mode Propagation on Coplanar Microstructure MIS Transmission Lines," *IEEE Trans. Microwave Theory Tech.*, vol. 35, no. 6, pp. 545-551, Jun., 1987.
- [15] V. M. Hietala, "A Study of MIS Coplanar Slow-Wave Transmission Lines on Silicon," University of Minnesota, Minneapolis, MN, Ph.D. Dissertation, Aug., 1988.
- [16] V. M. Hietala and K. S. Champlin, "Measurement of the Microwave Properties of Micron-Sized Coplanar Transmission Lines," *Journal of Electromagnetic Waves and Applications*, vol. 5, no. 4/5, pp. 439-452, 1991.
- [17] E. Tuncer and D.P. Neikirk, "Highly Accurate Quasi-Static Modeling of Microstrip Lines Over Lossy Substrates," *IEEE Microwave Guided Wave Lett.*, vol. 2, no. 10, pp. 409-411, Oct., 1992.
- [18] The MathWorks, Inc., *The Student Edition of Matlab Version 4*. Englewood Cliffs, NJ: Prentice Hall, 1995.

- [19] K. S. Giboney, M. J. W. Rodwell, and J. E. Bowers, "Traveling-Wave Photodetectors," *IEEE Photon. Technol. Lett.*, vol. 4, no. 12, pp. 1363-1365, Dec., 1992.
- [20] J. E. Bowers and C. A. Burrus, Jr., "Ultrawide-Band Long-Wavelength p-i-n Photodetectors," *J. Lightwave Technol.*, vol. 5, no. 10, pp. 1339-1350, Oct., 1987.
- [21] A. V. Uskov, J. R. Karin, R. Nagarajan, and J. E. Bowers, "Dynamics of Carrier Heating and Sweepout in Waveguide Saturable Absorbers," *IEEE J. Quantum Electron.*, submitted.
- [22] K. J. Williams, R. D. Esman, and M. Dagenais, "Effects of High Space-Charge Fields on the Response of Microwave Photodetectors," *IEEE Photon. Technol. Lett.*, vol. 6, no. 5, pp. 639-641, May, 1994.
- [23] K. S. Giboney, M. J. W. Rodwell, and J. E. Bowers, "Field-Screening Effects in Travelling-Wave and Vertically Illuminated p-i-n Photodetectors," presented at 1995 Conf. Lasers Electro-Optics, Baltimore, MD, May, 1995, CFB4.

## CHAPTER 3

# DESIGN & FABRICATION

A prototype fully distributed travelling-wave photodetector (TWPD) with verifiable performance is produced by applying the theory of distributed photodetection presented in Chapter 2, semiconductor device physics and processing technologies, and appropriate measurement considerations. The theory for parallel-plate TWPD is extended to a more practical "hybrid-coplanar TWPD."

A simplified approach to device design is enabled by making use of the velocity-mismatch effective area derived in Section 2.4. Velocity-mismatch and carrier drift bandwidth limitations determine the overall device bandwidth. A device design is optimized for high bandwidth using this model together with material properties and fabrication considerations.

The devices are fabricated using a standard self-aligned ridge waveguide laser process with some modifications. The substrate is semi-insulating and proton implantation is employed to render epitaxial layers semi-insulating under coplanar transmission lines, which are realized with an interconnect metal layer.

The choice of material systems is restricted by measurement system resources. A short-pulse laser source suitable for very high-speed electro-optic (EO) sampling was available only in the 700-1000 nm wavelength range. The AlGaAs/GaAs material system is an obvious choice except that the GaAs substrate is opaque to the measurement wavelength. This is overcome by growing an AlGaAs sub-layer and removing the substrate.

### 3.1 Hybrid-Coplanar Travelling-Wave Photodetector

The device geometry chosen for fabrication, the hybrid-coplanar TWPD, is drawn in cross-section in Fig. 3.1. Alternatively, the parallel-plate TWPD design of Fig. 2.1 could be fabricated in a microstrip (MS) form. It has two advantages over the hybrid-coplanar design: the overall series resistance could be made significantly lower, and

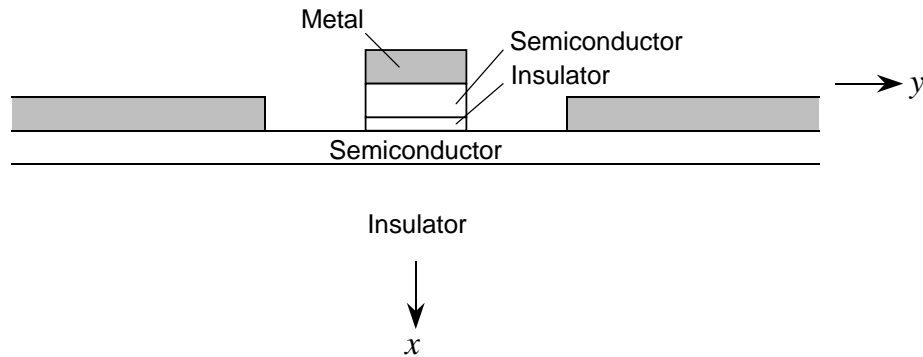


Fig. 3.1 Hybrid-coplanar TWPD structure.

the simple waveguide model of Sections 2.1 and 2.2 directly applies. However, the MS form has the major disadvantage that its fabrication would require significant development of new semiconductor device processing technologies in order to fabricate a structure with very high bandwidth.

The hybrid-coplanar design is compatible with coplanar waveguide (CPW), facilitating measurements, and a high-bandwidth design can be fabricated using well-established processing techniques. Microwave probes interface with CPW, and signals in CPW are easily measured by EO sampling. The fabrication of the ridge-waveguide structure is similar to that for high-speed lasers [1].

Equivalent-circuit models accurately describe the propagation characteristics of metal-insulator-semiconductor (MIS) coplanar structures like the ones drawn in Fig. 3.2, according to comparisons with measurements and full-wave simulations [2-7]. It was shown in Chapter 2 that characteristics of wave propagation on a parallel-plate TWPD are essentially identical to those on a parallel-plate MIS structure. CPW also being a quasi-TEM waveguide, it is reasonable to assume that the same similarity applies in the coplanar geometry.

The designation "hybrid-coplanar" TWPD derives from the fact that its propagating mode has characteristics of both MS and CPW modes. As in the parallel-plate TWPD, the currents are primarily carried in the metal and nearly all of the voltage drops across the i-layer. Thus, in the hybrid-coplanar TWPD, the magnetic field distribution is that of CPW, while the electric field pattern is similar to that of an MS structure.

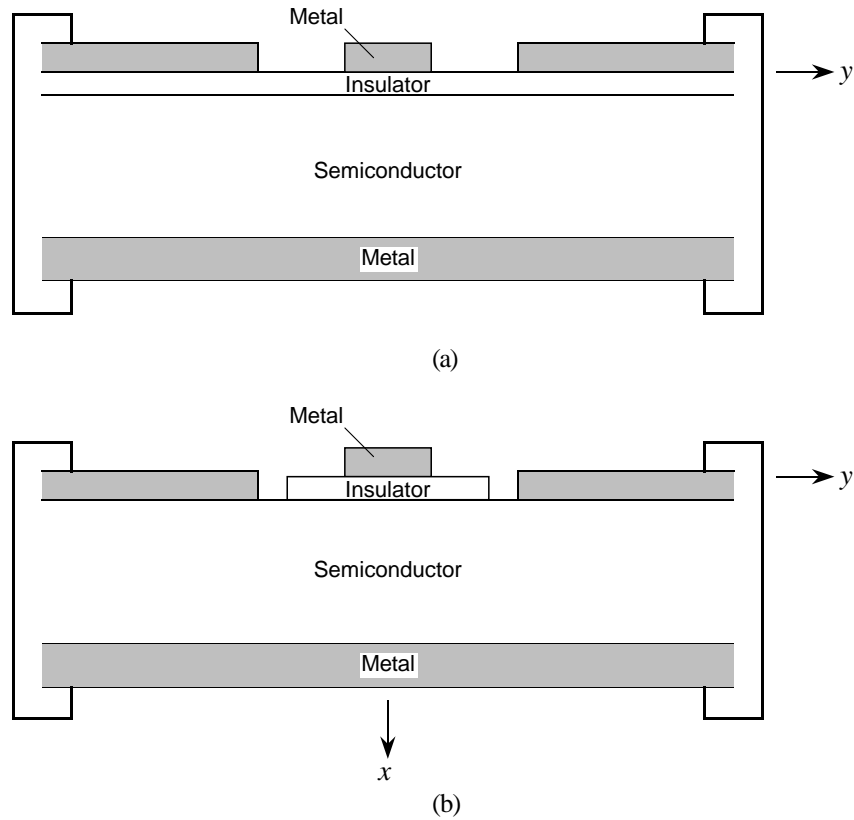


Fig. 3.2 Examples of coplanar metal-insulator-semiconductor (MIS) structures.

Fig. 3.3 defines the structure dimensions and material properties that lead to the equivalent-circuit of Fig. 3.4. The element values used to design and analyze the propagation characteristics of the hybrid-coplanar TWPDP, hereafter simply referred to as "TWPDP" are listed in Table 3.1. The upper and lower layers are distinguished by the designations "t" and "b" for top and bottom. The metal impedance of the bottom metal is ignored because the impedance of the top metal,  $Z_{mt}$ , is much greater. Similarly, the conductance of the bottom semiconductor layer is neglected because the conductance of the top semiconductor layer,  $G_{st}$ , is much less.

The impedance of the bottom layer is composed of terms for the spreading resistance under the top layer mesa, the bulk resistance of the gap between the mesa and the bottom contact, and the resistance of the bottom contact. The spreading resistance includes a factor of 1/2 for the structural symmetry and a factor of 1/3 that results from the current distribution. The bottom contact resistance is proportional to

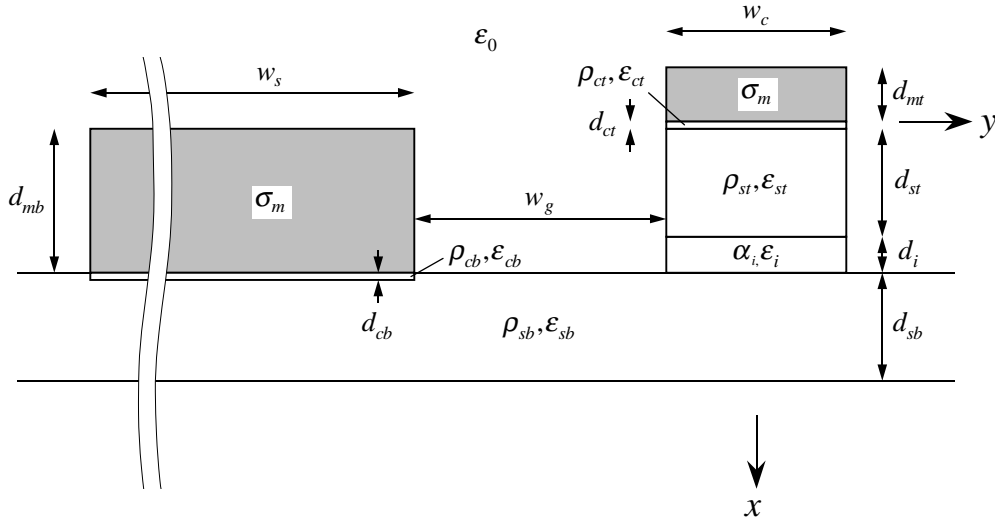


Fig. 3.3 Hybrid-coplanar TWPD structural dimensions and material properties.

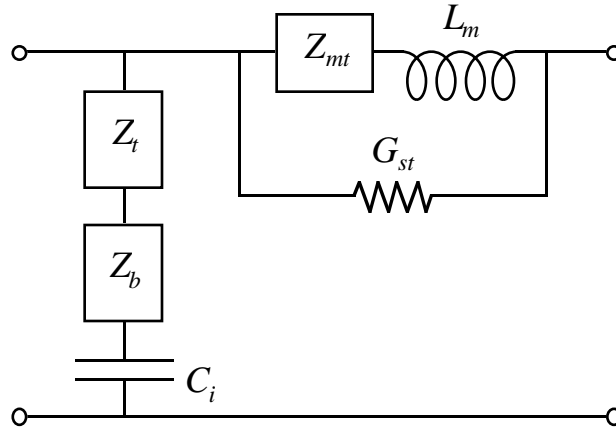


Fig. 3.4 TWPD equivalent-circuit model for transmission line characteristics. Circuit elements are identified with their associated layers in Fig. 3.3. Element values are listed in Table 3.1.

the transfer length,  $w_T$ . The whole expression is divided by two because of the bilateral symmetry.

The inductance,  $L_m$ , is equal to that of CPW with identical metal pattern, and can be found from a commercial program such as LineCalc [8]. The elements of the equivalent circuit that are important for TWPD design are  $L_m$  and  $C_i$ , which give the characteristic impedance,  $Z_0$ , and electrical phase velocity,  $v_e$ . In fact, if the optical absorption length,  $1/\Gamma\alpha_i$ , is very much shorter than the electrical attenuation length,

$$\begin{aligned}
Z_i &= \left( \frac{\rho_{ct} d_{ct}}{1 + j\omega\rho_{ct}\epsilon_{ct}} + \frac{\rho_{st} d_{st}}{1 + j\omega\rho_{st}\epsilon_{st}} \right) / w_c & Z_{mt} &= \frac{\eta_{xm0t}}{w_c} \\
Z_b &= \frac{\rho_{sb}}{1 + j\omega\rho_{sb}\epsilon_{sb}} \cdot \frac{(w_c/6 + w_g + w_T)}{2d_{sb}} & G_{st} &= \frac{\sigma_{st}}{3} w_c d_{st} \\
w_T &= \sqrt{\frac{\rho_{cb}}{\rho_{sb}} \cdot \frac{1 + j\omega\rho_{sb}\epsilon_{sb}}{1 + j\omega\rho_{cb}\epsilon_{cb}} d_{cb} d_{sb}} & & \\
C_i &= \epsilon_i \frac{w_c}{d_i} & L_m &= L_{CPW}
\end{aligned}$$

Table 3.1 Hybrid-coplanar TWPD element values for the equivalent-circuit model in Fig. 3.4.  $\rho$  is resistivity and  $\sigma = 1/\rho$  is conductivity;  $\epsilon$  and  $\mu$  are permittivity and permeability. The metal-air transverse wave impedance,  $\eta_{xm0t}$ , is expressed in Eq. (2.4). The coplanar waveguide inductance,  $L_{CPW}$ , is found from a numerical model. The dimensions and material characteristics are indicated in Fig. 3.3.

$1/\alpha_e$ , then the device can be made electrically short,  $\alpha_e \ell \ll 1$ , and optically long,  $\Gamma\alpha_i \ell \gg 1$ . In this case, details of the electrical propagation characteristics can be ignored, and optical dispersion and chirp can be neglected, also.

### 3.2 Bandwidth Model

Given an electrically short, optically long TWPD, Eq. (2.32) is used to reduce the design procedure to that of a vertically illuminated photodetector (VPD) of equal area. This important equation is repeated here using the dimensions of Fig. 3.3,

$$A_{vm1} = w_c \frac{1.5}{\Gamma\alpha_i}. \quad (3.1)$$

The velocity-mismatch bandwidth limitation of a TWPD is functionally equivalent to an RC bandwidth limitation of a VPD. The same design equations and considerations apply with the simple substitution of (3.1) for the junction area.

Photodetector bandwidth is limited by carrier drift, carrier diffusion, and carrier trapping, in addition to the RC time [9-11]. Double-heterostructure epitaxial design eliminates carrier diffusion contributions to the response resulting from

photogeneration in low-field regions, and graded bandgap layers minimize carrier trapping at the hetero-interfaces [12-14]. The primary bandwidth limitations for well-designed devices result from velocity-mismatch or RC, and carrier drift times.

Carrier drift times are determined by the detailed dynamics of electrons and holes in a high electric field. Velocity overshoot of electrons is considered an important effect in high-speed electronic devices [15]. Velocity overshoot or ballistic transport occurs in semiconductors due to the fact that the momentum relaxation time is much shorter than the energy relaxation time. Electrons accelerate with the low-field mobility for a period of less than the energy relaxation time in response to a step in the drift field. This makes it possible for electrons to attain peak velocities greater than the steady-state velocity before scattering events bring the distribution to its steady state [16-18].

The energy standard deviation of a one picosecond transform-limited optical pulse is about 1 meV. Electrons excited in a direct bandgap semiconductor by such a pulse will have the same energy spread, and the momentum will be distributed about a spherical shell in k-space. A bandgap energy optical pulse will generate a spherical electron velocity distribution centered at zero with a standard deviation of approximately the saturated drift velocity. The scattering times of a large fraction of this distribution are much shorter than one picosecond, so transient velocity overshoot effects will not be observable in the optically generated response.

An approximate carrier drift photocurrent impulse response is derived by assuming uniform illumination and constant, uniform carrier drift velocity in the depletion region, which is roughly the i-layer,  $d_d \approx d_i$  [10]. This gives a one-sided triangle function for each carrier type,

$$i_d(t) = \frac{2Q}{\tau_d} \left( 1 - \frac{t}{\tau_d} \right) \quad (3.2)$$

for  $0 \leq t \leq \tau_d$  and zero elsewhere.  $\tau_d \equiv d_d/v_d$  is the time required to traverse the entire depletion layer at the carrier drift velocity. The carrier drift photocurrent frequency response is the Fourier transform of (3.2),

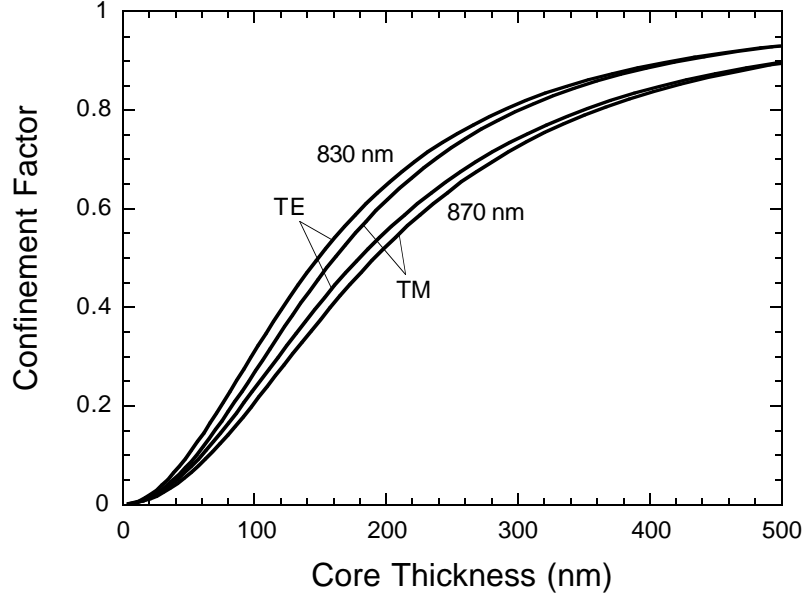


Fig. 3.5 Confinement factor of TE and TM modes of an  $\text{Al}_{0.22}\text{Ga}_{0.78}\text{As}/\text{GaAs}$  symmetric slab waveguide at 830 nm and 870 nm wavelengths.

$$i_d(\omega) = Q \left\{ \text{Sa}^2 \left( \frac{\omega\tau_d}{2} \right) + j \frac{2}{\omega\tau_d} [\text{Sa}(\omega\tau_d) - 1] \right\}, \quad (3.3)$$

where  $\text{Sa}(\omega\tau) \equiv \sin(\omega\tau)/\omega\tau$ . The carrier drift 3 dB bandwidth limitation,

$$B_d = \frac{0.55v_d}{d_d} \quad (3.4)$$

is used in Fig. 2.21.

### 3.3 Device Design

The confinement factor in (3.1) is the product of transverse and lateral components,  $\Gamma = \Gamma_x\Gamma_y$ . The transverse confinement factor,  $\Gamma_x$ , is calculated for a three-layer symmetric slab dielectric waveguide, and plotted in Fig. 3.5 [19, 20]. The lateral confinement factor is assumed to be unity,  $\Gamma_y = 1$ .

	Resistivity of $\text{Al}_{0.22}\text{Ga}_{0.78}\text{As}$ Layers ( $\Omega \cdot \mu\text{m}$ )	Carrier Velocity in Depletion Layer (nm/ps)
n-type/electrons	70	90
p-type/holes	90	70

Table 3.2 Resistivities of semiconductor layers and carrier velocities in depletion region.

	Contact Resistance ( $\Omega \cdot \mu\text{m}^2$ )	
	n	p
Top (GaAs)	50	300
Bottom ( $\text{Al}_{0.22}\text{Ga}_{0.78}\text{As}$ )	700	700

Table 3.3 Specific contact resistance ( $\rho_c d_c$ ) to n- and p-type top and bottom layers.

Since very high efficiency is ancillary to demonstrating TWPDs, only moderate effort is expended in optimizing the optical waveguide for high coupling efficiency. A large optical mode gives good coupling efficiency and is obtained by using a small index difference between the core and cladding layers. A GaAs/ $\text{Al}_{0.22}\text{Ga}_{0.78}\text{As}$  double heterostructure gives a small index difference of 0.22 at  $\lambda = 830$  nm while maintaining an optical bandwidth of greater than 100 nm [21].

AlAs fractions below 0.24 also can have relatively low resistivity and low contact resistance [22, 23], so the dielectric relaxation frequencies of the heavily-doped semiconductor cladding layers are larger than the photodetector bandwidth. This means that the frequency dependence associated with the semiconductor layers in the equations for  $Z_t$  and  $Z_b$  in Table 3.1 can be ignored over the device bandwidth. Assuming a specific contact resistance of  $700 \Omega \cdot \mu\text{m}^2$  and a contact layer thickness of 10 nm, the dielectric relaxation frequency of the bottom contact layer is about 20 GHz. This is far below the expected device bandwidth; however, a more conservative design results from ignoring all frequency dependencies in  $Z_t$  and  $Z_b$ .

The top cladding layer is made thick enough that the optical field is small at the metal interface. This is to prevent excess optical loss from absorption and scattering at

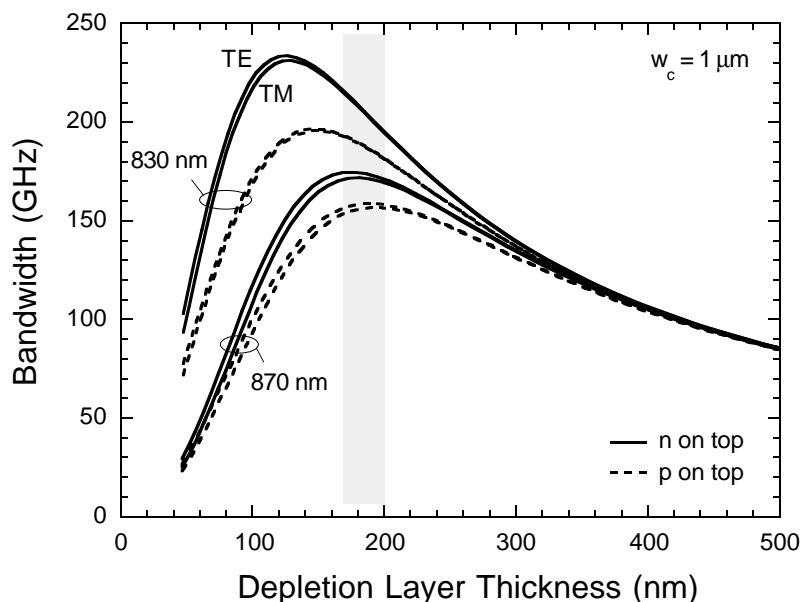


Fig. 3.6 Net bandwidths of one micron wide TWPDs vs. depletion layer thickness for TE and TM mode illumination at 830 and 870 nm wavelengths. Calculations are shown for two different epitaxial arrangements: n on top, and p on top. The optical absorption coefficients of the i-layer are  $\alpha_i = 1, 0.2 \mu\text{m}^{-1}$  at 830, 870 nm. Other material properties are listed in Tables 3.2 and 3.3.

the rough, alloyed interface. A top semiconductor layer thickness of  $0.6 \mu\text{m}$  is sufficient to keep the fraction of optical energy in the mode intersecting this interface to less than  $10^{-3}$ .

The overall device thickness is restricted by the maximum range of the proton implant used for isolation, effectively limiting the bottom cladding layer thickness. The commercial ion implanter machine used has a maximum accelerating voltage of 200 kV. The projected range of 200 keV protons in GaAs is roughly  $1.6 \mu\text{m}$  [24-26]. A quarter micron of gold on top of the GaAs reduces the range in the GaAs to about  $1.2 \mu\text{m}$ , but the projected standard deviation is about  $0.2 \mu\text{m}$  [27]. Thus, doped semiconductor layers can extend to about  $1.4 \mu\text{m}$  deep from the wafer surface.

For the highest possible bandwidth, the lateral geometry of the device is determined by lithographic limitations. The velocity mismatch bandwidth limitation is inversely proportional to the width,  $w_c$ , so the width is designed to be  $1 \mu\text{m}$ , which is close to the minimum possible with the available contact lithography. The lateral

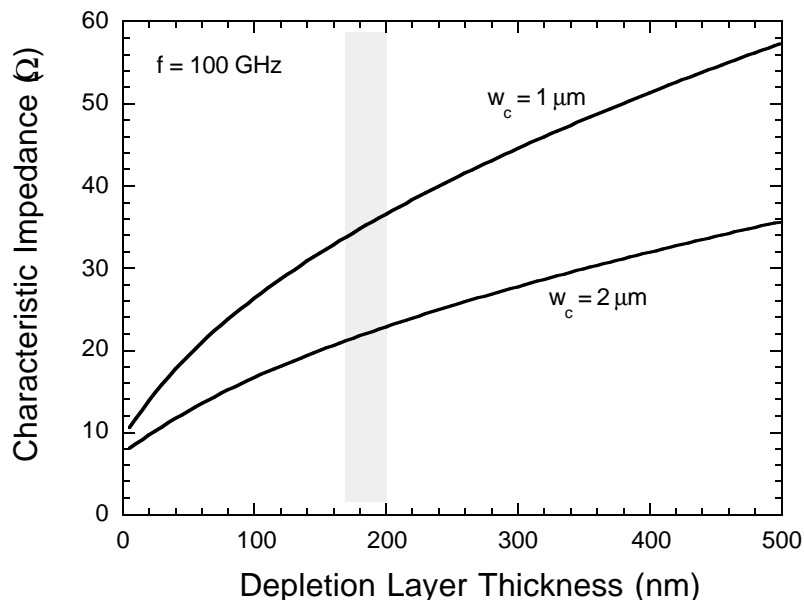


Fig. 3.7 Characteristic impedances of one and two micron wide TWPDs vs. depletion layer thickness.

coupling to a  $1 \mu\text{m}$  ridge at GaAs wavelengths can be nearly 100%, but further reduction of the width to much below  $1 \mu\text{m}$  would adversely affect coupling efficiency. It is clear that series resistance is decreased and velocity mismatch bandwidth limitation is increased by reducing the gap, so  $w_g$  is determined by the  $2 \mu\text{m}$  alignment tolerance.

The velocity mismatch bandwidth limitation is directly proportional to the confinement factor, while the carrier drift bandwidth limitation is inversely proportional to the depletion layer thickness. This tradeoff is assessed in Fig. 3.6 by plotting the net bandwidth of one micron wide devices as a function of depletion layer thickness, which is approximately equal to the core thickness. Values of material properties are listed in Tables 3.2 and 3.3.

Bandwidths for TE and TM mode illumination at 830 nm and 870 nm wavelengths are compared for two different epitaxial designs: n on top, and p on top. The top AlGaAs layer can be graded to a heavily doped GaAs layer at the surface for low contact resistance, but this is not possible for the bottom contacts. The

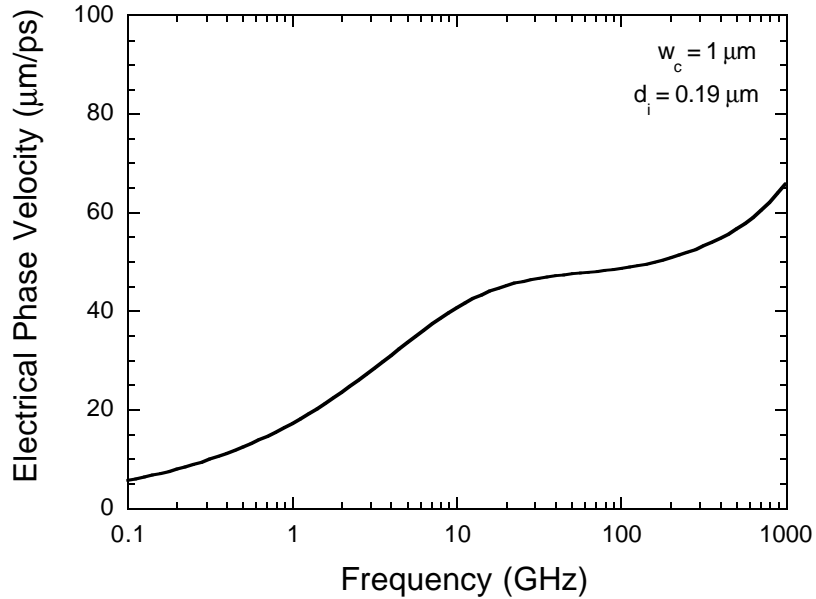


Fig. 3.8 One micron wide TWPD electrical phase velocity vs. frequency for depletion layer thickness of 0.19  $\mu\text{m}$ .

bandwidths are significantly worse for the p on top design because the contact resistance to p-type GaAs is much higher than to n-type GaAs.

There are no free parameters left to constrain the characteristic impedance, which is plotted as a function of depletion layer thickness for one and two micron wide devices in Fig. 3.7. A depletion layer thickness of 380 nm is required for a 50  $\Omega$ , 1  $\mu\text{m}$  wide TWPD, but from Fig. 3.6, this would limit the bandwidth to 110 GHz. Much higher bandwidths would be possible by designing for a lower impedance environment. As indicated on the plots, a one micron TWPD of 36  $\Omega$  characteristic impedance could have bandwidth exceeding 200 GHz.

The propagation characteristics of a one micron TWPD with 190 nm depletion layer thickness are plotted in Figs. 3.8 – 3.10. They display similar features as the corresponding plots for parallel-plate TWPDs in Figs. 2.10 – 2.12.

CPW transmission lines connecting to the devices are designed with two different characteristic impedances, about 40 and 50  $\Omega$ , that result in reflection coefficients at the 1  $\mu\text{m}$  TWPD/transmission line interfaces of 0.05 and 0.16. The 2  $\mu\text{m}$  wide devices are waveguide photodetectors (WGPDs) because their low characteristic

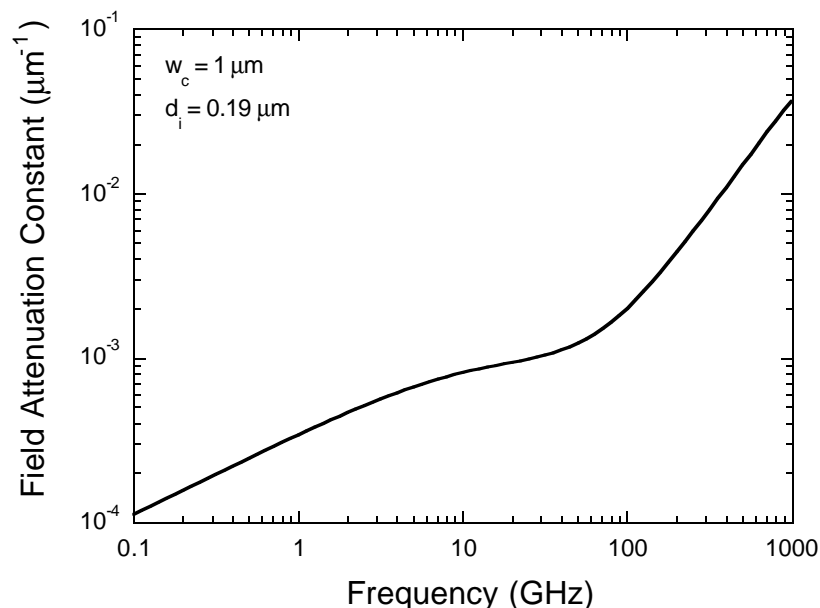


Fig. 3.9 Field attenuation constant of one micron wide TWPD.

impedance of about  $22 \Omega$  results in large reflection coefficients of 0.29 and 0.39 at the transmission line connections.

Long transmission lines assure that the load seen by the device is constant at the design value over a specified measurement time window. Reflections from discontinuities beyond this initial length of transmission line arrive after the measured response and can simply be ignored. The transmission lines connecting to the TWPDs and WGPLDs are over  $800 \mu\text{m}$  long. Assuming the EO sampling measurement point is  $100 \mu\text{m}$  from the device, signals propagate a round-trip distance of  $1.4 \text{ mm}$  before reflections reach the measurement point. The CPW propagation velocity, after the substrate is removed for EO sampling, is about  $140 \mu\text{m}/\text{ps}$ , so this leaves about a  $10 \text{ ps}$  measurement window.

The CPW dimensions are kept small according to criteria discussed in Section 4.3 on optical transit time in EO sampling measurements. Small dimensions are also necessary to maintain the desired characteristic impedance after the substrate has been removed and the chip attached to lower dielectric constant glass. LineCalc is used to

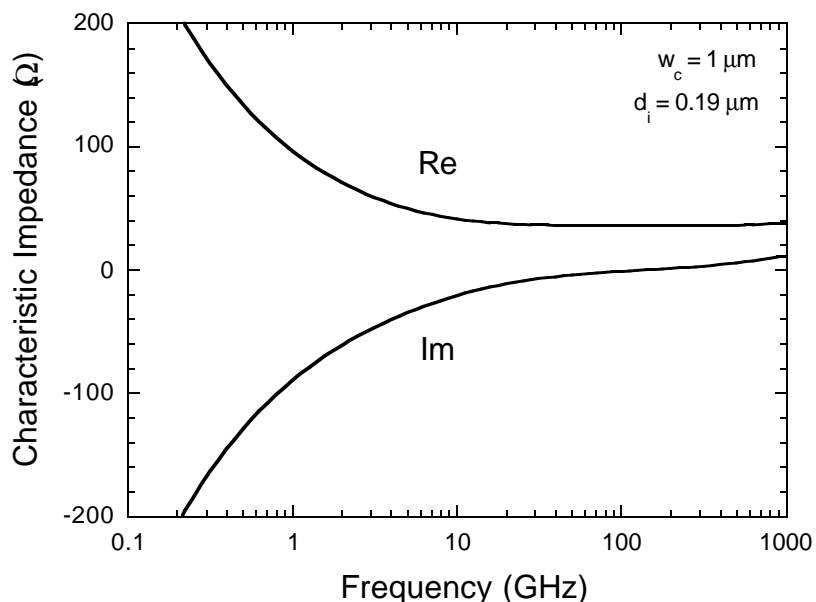


Fig. 3.10 Characteristic impedance of one micron wide TWPD.

design the CPW on the very thin sublayer for the desired characteristic impedances [8].

The mask is designed using commercial layout software [28]. It is produced in chrome on quartz by an outside vendor using electron-beam lithography with 0.25  $\mu\text{m}$  spot size [29].

The GaAs/AlGaAs p-i-n graded double heterostructure layers, designed with the aid of a program that calculates band structure, are listed in Table 3.4 [30, 31]. The band diagram at zero bias is plotted in Fig. 3.11(a). The AlAs fraction and doping are both graded in the n-contact graded layer to reduce the heterojunction barrier compared to an abrupt interface, as shown in Fig. 3.11(b). Figs. 3.11(c) and 3.11(d) show that the barrier at each core-cladding heterointerface is minimized by linear grading of the AlAs fraction and an abrupt doping step.

The p grade benefits from the fact that the valence band offset is about half of the conduction band offset for low AlAs fractions [16]. In fact, grading is probably unnecessary because of the small valence band offset. The grading of the n-interfaces

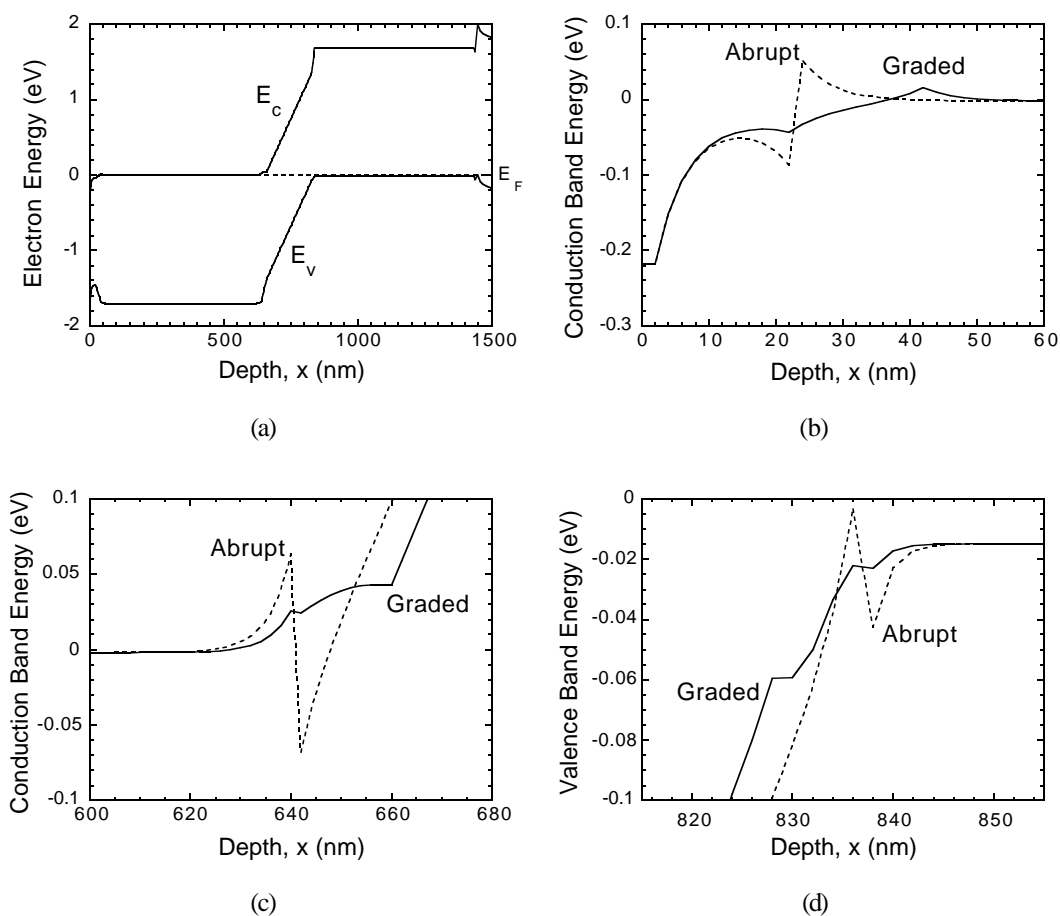


Fig. 3.11 TWPD (a) band diagram, and (b) contact, (c) n-i, and (d) i-p graded and abrupt interfaces.

reduces the barriers to electrons by a factor of four from the abrupt barrier heights of about  $2kT$ .

The GaAs substrate must be etched away for EO sampling measurements because it is opaque to the probe beam. An  $\text{Al}_{0.5}\text{Ga}_{0.5}\text{As}$  sublayer is an etch stop for substrate removal, provides mechanical strength after the substrate is removed, and is an electro-optic crystal for the EO sampling measurements.

### 3.4 Fabrication

The design optimization yields the structure and epitaxy drawn in Fig. 3.12. Fabrication is based on a ridge-waveguide laser process [1] with steps added for proton implant isolation, substrate removal, and anti-reflection coating. New

Layer Name	Thickness (nm)	AlAs Mole Fraction	Doping (cm <sup>-3</sup> )
n Contact	20	0	7·10 <sup>18</sup>
n Contact Grade	18	Linearly Graded	Linearly Graded
n Cladding	600	0.22	4·10 <sup>18</sup>
n Grade	18	Linearly Graded	Abrupt – 140 Å setback
i (Core)	170	0	0
p Grade	8	Linearly Graded	Abrupt – 40 Å setback
p Cladding	600	0.22	5·10 <sup>19</sup>
Sublayer	3 μm	0.5	0
Substrate	150 μm	0	SI

Table 3.4 AlGaAs TWPD layer design.

processes are developed for the proton implant isolation, and for substrate removal and device mounting. The detailed process plan is listed in Appendix B.

The GaAs/AlGaAs p-i-n graded double heterostructure is grown by molecular-beam epitaxy (MBE) on a semi-insulating GaAs substrate using Be and Si as p- and n-type dopants. The graded regions are digital alloys with 2 nm period. The p- and n-layers are grown at about 570 C and the i-layer at roughly 590 C.

Since the doping gradient in a p-i-n diode is very steep at the interfaces, dopant diffusion is a concern. Significant displacement of dopants results in a need for higher bias voltage to fully deplete the low field regions and achieve high speed photoresponse. Furthermore, dopant displacement will spoil the grading scheme for reducing the heterojunction barriers.

The diffusion coefficient of Be in GaAs is over three orders of magnitude larger than that of Si at MBE growth temperatures [32]. The n on top configuration is more likely than the p on top to suffer the effects of dopant diffusion because it is at the growth temperature after growth of the p-i interface longer by the time necessary to grow the i-layer. Since the i-layer is thin in comparison to the cladding layers, the fractional time difference is small. In fact, the fastest photoresponses, presented in

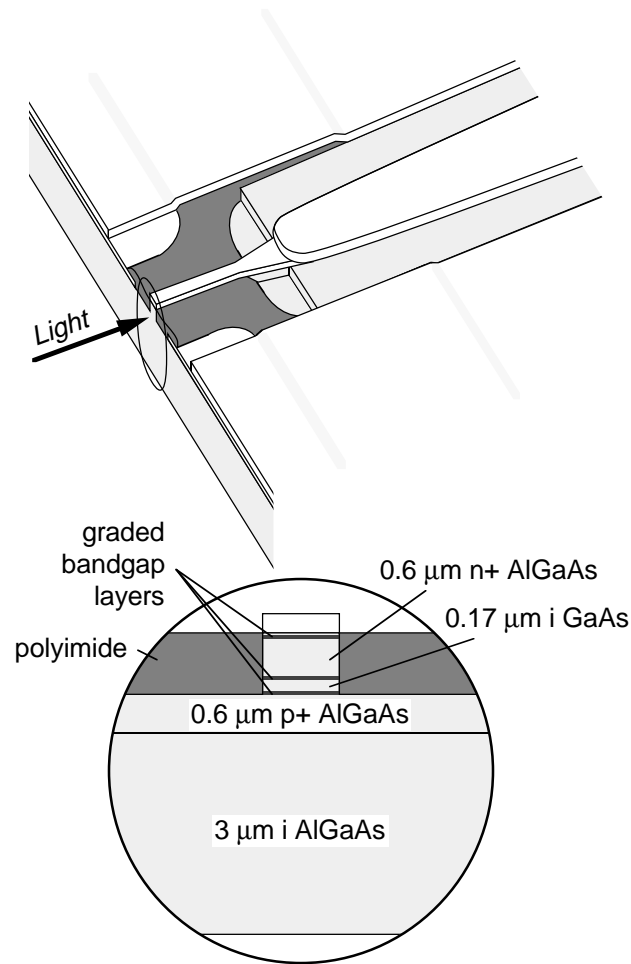


Fig. 3.12 Schematic drawing of TWPD structure and epitaxy.

Chapter 5, occur at only 1 V bias, indicating that dopant diffusion does not affect these devices.

The top ohmic contact metallization is standard NiAuGe composition, deposited by electron-beam evaporation [1, 33]. The ridge waveguides and mesas are defined by Cl reactive-ion etching, self aligned to the top ohmic contacts [34]. The interferometric signal from a HeNe laser beam reflected from the wafer layers during etching produces a characteristic pattern that corresponds to the epitaxy [1, 35]. The trace is used as a monitor to enable reproducible etch depths. The etch is stopped

immediately after it goes through the i-layer. The top contact is then annealed at 380 C for 15 s.

The CrAuZn bottom ohmic contact metallization is deposited by thermal evaporation [36]. After annealing at 405 C for 20 s, the wafer is ready for proton implant isolation.

PMGI polymer is used as a lift-off layer for the implant mask, which protects the devices while the rest of the wafer is rendered semi-insulating [37]. A thick Ti/Au implant mask is deposited by electron-beam evaporation using a special fixture to hold the sample closer to the material source than the standard sample holder. This fixture exposes the sample to higher flux, by a factor of 3.1, and conserves on expensive source material when thick layers are deposited. The 1.6  $\mu\text{m}$  thick Au assures that the protons will not penetrate the mask [27].

A simple method is developed to calculate the implant dose and energy. First, the energy is found by converting all layers to equivalent thicknesses of GaAs. For low energies, where the projected range is in the layer, the thickness of each layer is scaled by the ratio of the projected range for GaAs to the projected range for that layer. For high energies, where the projected range is much greater than the layer thickness, the thickness of each layer is scaled by the ratio of the energy loss rate in that layer to the energy loss rate in GaAs. A linear combination of these two results is formed for intermediate energies. This conversion does not account for projected standard deviation, but results in a sufficiently good approximation for most semiconductors and metals.

With the layers converted to equivalent thicknesses of GaAs, multiple implants are aligned according to the projected ranges and standard deviations. The damage profile is assumed coincident with the proton profile. The standard Pearson IV distribution drops roughly 0.5 decades in the first standard deviation either side of the projected range. It then decreases at a rate of about 0.6 decades/standard deviation to the surface, and at a rate of about 2.5 decades/standard deviation toward the substrate [26, 38]. For multiple implants designed to isolate material of constant carrier density, a simple rule of thumb is to align the edges of the projected standard deviations. When the carrier density is nonuniform, the above rates can be used to align the implants relative to each other.

The dose is designed to over-damage the material, and then the damage is partially annealed to achieve maximum isolation. Carrier conduction in the bands decreases with dose while "hopping conduction" increases with dose. Hopping conduction consists of carrier transport along damage sites. The two trends result in a maximum sheet resistance as a function of damage. Annealing removes shallow gap states that are more likely to be centers for hopping conduction [26, 37-39].

The carrier removal efficiency of protons is about 3-5 carriers per ion [26]. The dose is determined by the constant

$$\frac{\phi}{\sigma_p N} = 20 \quad (3.5)$$

where  $\phi$  is the proton dose,  $\sigma_p$  is the projected standard deviation, and  $N$  is the donor or acceptor concentration at the projected range.

The rate at which the dose is delivered is limited by the temperature of the PMGI layer, which becomes difficult to remove if it gets too hot. The implant current density times the energy gives the intensity (power per unit area) dissipated in the target. Heat is conducted away from shallow implants roughly half as efficiently as for deep implants due to the high thermal resistance at the surface. Also, since shallow implants are closer to the PMGI, the power dissipation should be further limited. The limits on current effectively limit the maximum practical dose because dose/current = time = money.

The implant was performed by a commercial service [40]. The isolation mask is removed by first etching the exposed PMGI in oxygen plasma. After the exposed PMGI is completely removed, the PMGI under the mask is dissolved in NMP [41].

Polyimide is used for passivation and to bridge the interconnect-metal coplanar-transmission lines to the ohmic contacts [42]. A planarization and etch back technique is used to connect bias pads to optical preamplifier ridges [1]. The surface is planarized with photoresist, which is also patterned. The exposed polyimide is etched away in low-frequency (directional) oxygen plasma. Photoresist etches at about the same rate as polyimide, so polyimide on small and narrow mesas is simultaneously uncovered and etched some. This tends to planarize the polyimide. After the photoresist is stripped, the polyimide is etched further in high-frequency (less

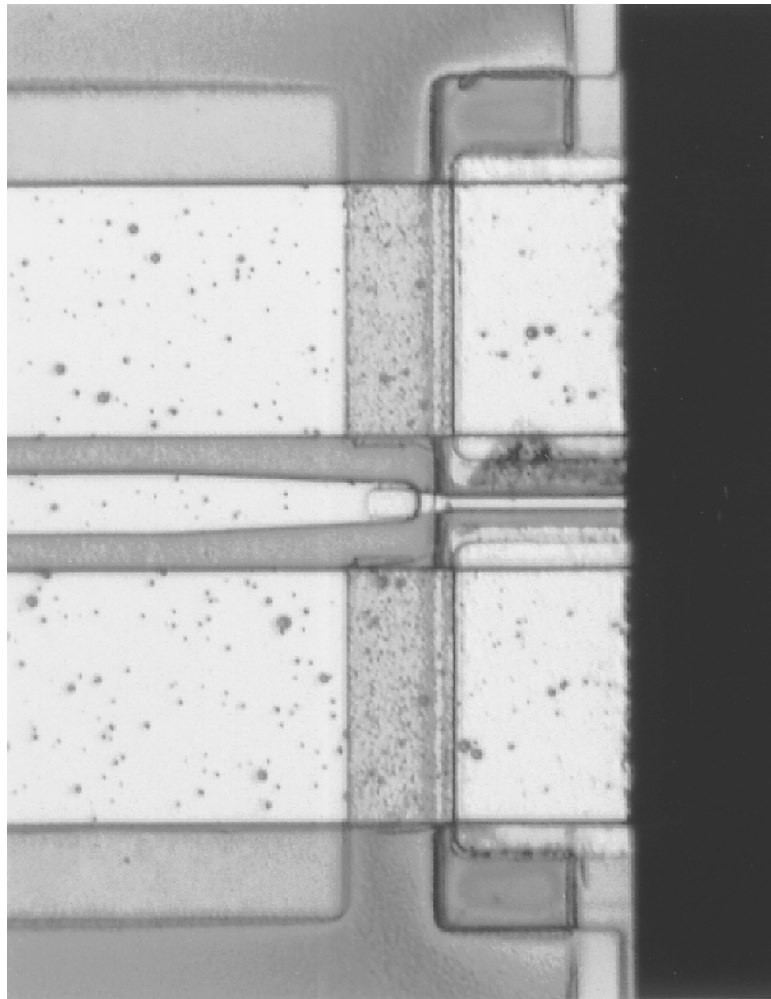


Fig. 3.13 Close-up photograph of a TWPD. TWPD is in right half of photograph, left half shows connecting CPW transmission line.

directional) oxygen plasma to expose narrow mesas and round the edges of the polyimide that are used to bridge interconnect metal.

The implant is annealed during the polyimide bake. The field resistivity increased from about  $25 \text{ M}\Omega\cdot\mu\text{m}$  for all layers as implanted to  $400\text{-}1500 \text{ M}\Omega\cdot\mu\text{m}$ , depending on the layer and implant depth, after annealing. This is an improvement by a factor of 16 to 60, and greatly reduces the leakage current in the long CPW transmission lines. Even with the high surface resistance of  $2.2 \text{ G}\Omega/\text{square}$ , leakage in the transmission lines is about  $2 \mu\text{A}$  at  $5 \text{ V}$ , much larger than the reverse current of a TWPD.

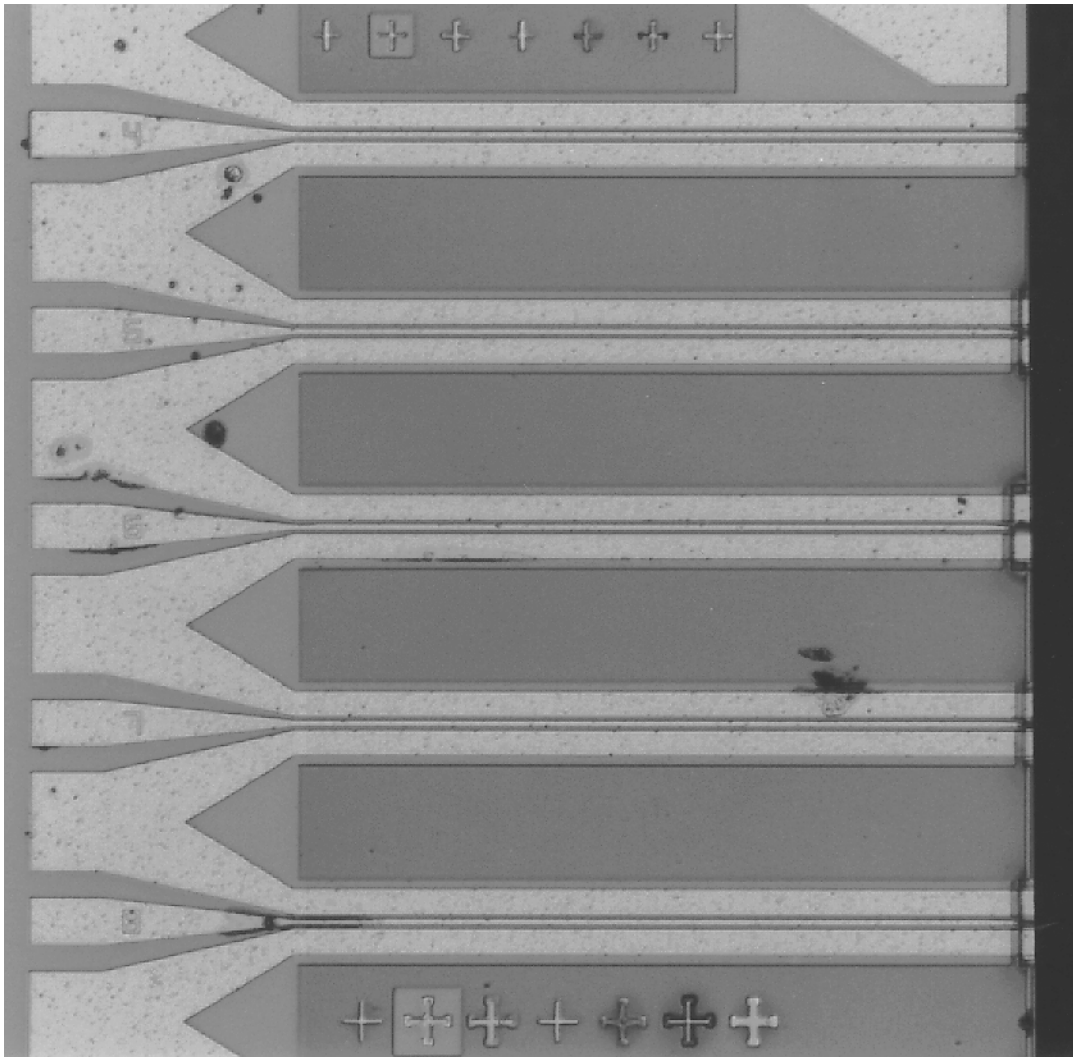


Fig. 3.14 Photograph of several TWPDs and connecting CPW transmission lines. Photodetectors are at the right edge of the chip. CPW transmission lines extend from the devices to the coplanar microwave probe pads on the left side.

The CPW transmission lines are formed by the Ti/Au interconnect metal, which is  $0.75\ \mu\text{m}$  thick for low series resistance in the long lines. The titanium layer is necessary for adhesion of the gold. The polyimide bridges the interconnect metal into the well left by the mesa etch, and then the interconnect metal overlays the bottom ohmic contact metal over the length of the TWPD, as shown in Fig. 3.12. The interconnect metal contacts the end of the TWPD top ohmic contact metal.

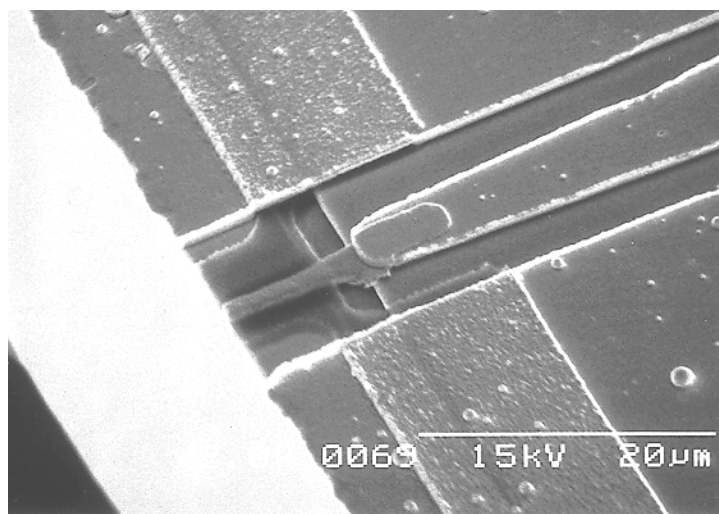


Fig. 3.15 SEM photograph of a TWPD. CPW transmission line extends to the left.

The EO sampling probe beam is reflected from the backside of the interconnect metal. The reflectivity of a thick layer of titanium on semiconductor is only 0.21 at 0.85  $\mu\text{m}$  wavelength, while gold is 0.94. Other materials used as adhesion layers, such as Cr and Ni, also have very poor reflectivities. The overall reflectivity of Au on a standard Ti layer thickness of 20 nm is 0.35. This reflectivity is doubled to 0.71 by reducing the Ti layer thickness to 5.6 nm, effectively doubling the signal-to-noise ratio and sensitivity of the EO sampling measurements.

Fig. 3.13 shows a close-up view of a TWPD, at right, and the connecting CPW transmission line. The long CPW transmission lines of several devices are evident in Fig. 3.14. The devices are at the right, and pads for coplanar microwave probe are at the left. Fig. 3.15 shows a scanning electron microscope (SEM) photograph of a finished device. The CPW transmission line extends to the right in this figure. The spheroidal defects in the CPW gold are due to contamination in the evaporator source material.

The GaAs substrates of chips selected for electro-optic sampling are etched away to the 3  $\mu\text{m}$  thick  $\text{Al}_{0.5}\text{Ga}_{0.5}\text{As}$  sub-layer. After securing the chip face down to a silicon mechanical piece with crystal wax, the 200  $\mu\text{m}$  substrate is removed with a citric acid etch in 10-11 hours [43-45]. Surface roughness from the wafer lapping is

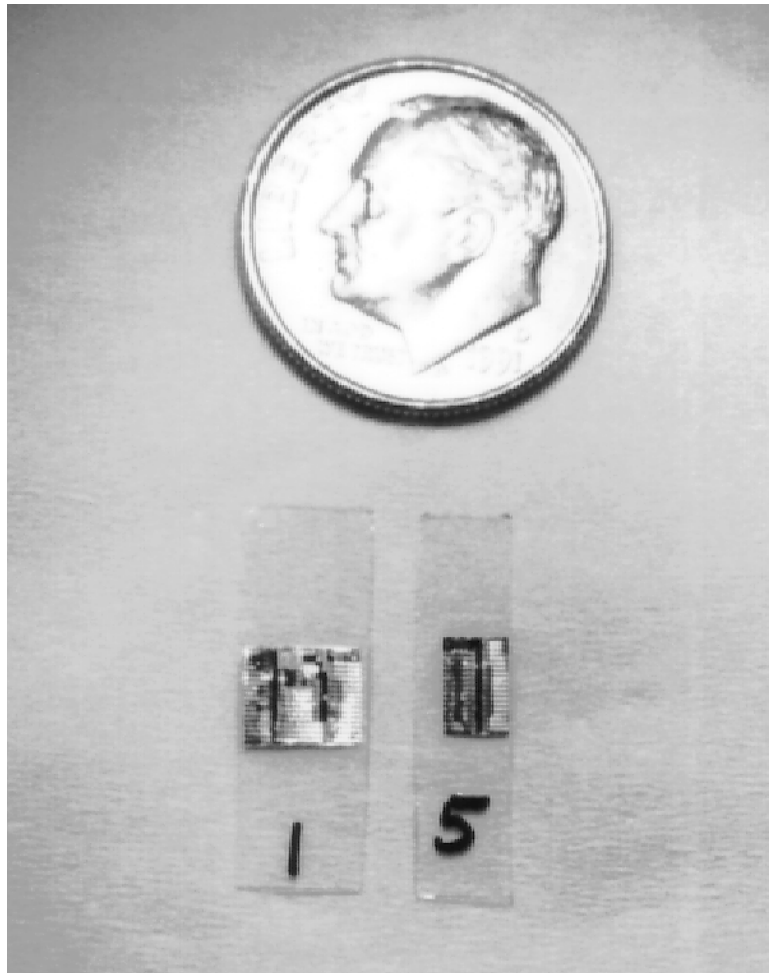


Fig. 3.16 TWPD chips mounted on glass slides after substrate removal.

reduced by the etch selectivity, which is estimated to be better than 500:1 for GaAs/ $\text{Al}_{0.5}\text{Ga}_{0.5}\text{As}$ . The resulting finish appears to be of optical quality.

Thin glass slides are attached to the 4  $\mu\text{m}$  thick chips with UV-curable epoxy while the chips are still secured to the mechanical silicon pieces [46]. The epoxy is exposed with a mask so that it remains only in areas where the EO sampling probe beam will not pass through it. The heat from laser absorption in the metal burns the epoxy. The remaining crystal wax and the unexposed epoxy are washed away in acetone. Fig. 3.16 shows TWPD chips attached to glass slides for EO sampling.

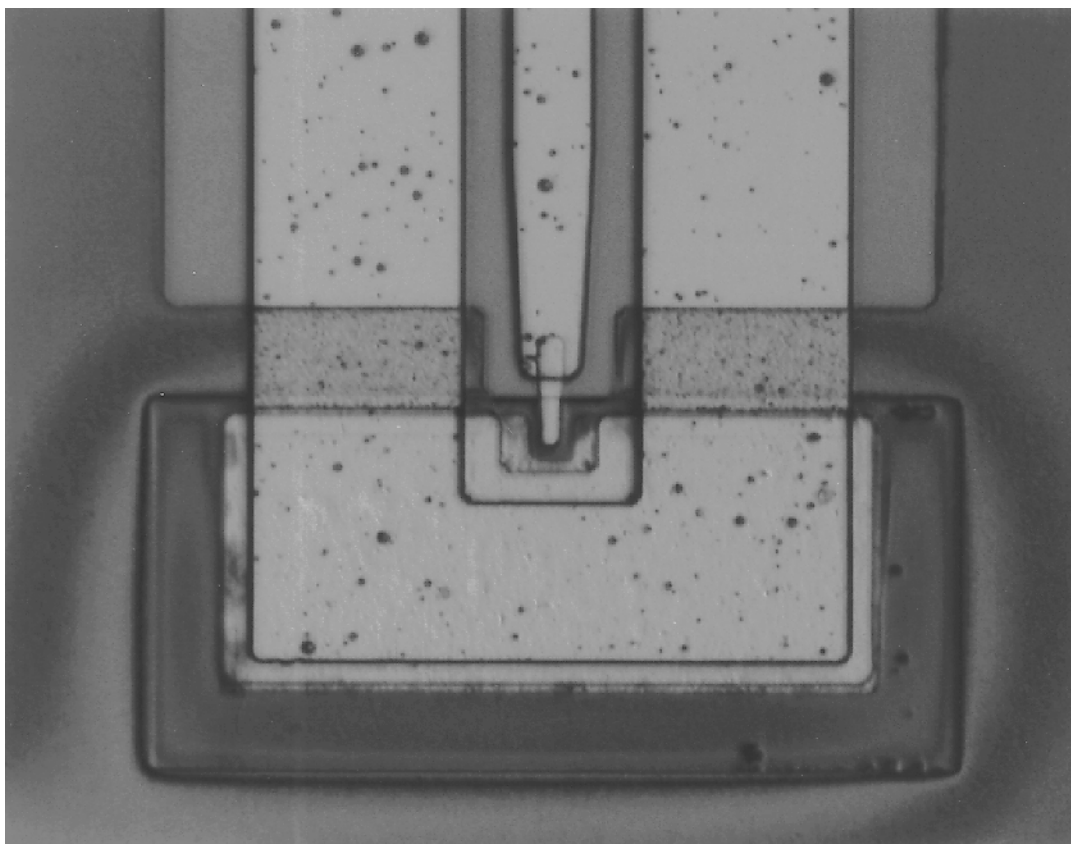


Fig. 3.17 Close-up photograph of a vertically illuminated photodetector.

An anti-reflection coating is applied to samples not used for EO sampling measurements. It is incompatible with the substrate removal process. The quarter-wavelength sputtered silicon nitride anti-reflection coating reduces the reflectivity to less than 1% over the 800-900 nm wavelength range.

One micron wide TWPDs, two and five micron wide WGDs, and two micron to ten micron square VPDs are on the same mask for direct comparison of their performance. The devices are fabricated on quarters of two inch wafers. The VPDs are illuminated through the sublayer and the light is reflected from the top contact metal for two passes through the absorber. Substrate removal is required for them to function. A close-up photograph of a VPD is in Fig. 3.17.

Design and fabrication of hybrid-coplanar TWPDs is detailed in this chapter. A bandwidth model is used to optimize the device structure. A modified ridge-waveguide laser process is used to fabricate TWPDs, WGPLDs, and VPDs on the same wafer for direct comparison. Special features that enable very high bandwidth measurements are incorporated into the design and fabrication process. Techniques for performing such measurements are explained in the next chapter.

## References

- [1] R. L. Nagarajan, "Carrier Transport Effects in High Speed Quantum Well Lasers," University of California, Santa Barbara, CA, Ph.D. Dissertation, Jul., 1992.
- [2] H. Hasegawa and H. Okizaki, "M.I.S. and Schottky slow-wave coplanar striplines on GaAs substrates," *Electronics Letters*, vol. 13, no. 22, pp. 663-664, Oct. 27, 1977.
- [3] C. Seguinot, P. Kennis, P. Pribetich, J. F. Legier, "Analytical Model of the Schottky Contact Coplanar Line," in *Proc. 14th European Microwave Conf.*, pp. 160-165, Sep., 1984.
- [4] C. K. Tzuang and T. Itoh, "Finite-Element Analysis of Slow-Wave Schottky Contact Printed Lines," *IEEE Trans. Microwave Theory Tech.*, vol. 34, no. 12, pp. 1483-1489, Dec., 1986.
- [5] Y. R. Kwon, V. M. Hietala, and K. S. Champlin, "Quasi-TEM Analysis of "Slow-Wave" Mode Propagation on Coplanar Microstructure MIS Transmission Lines," *IEEE Trans. Microwave Theory Tech.*, vol. 35, no. 6, pp. 545-551, Jun., 1987.
- [6] V. M. Hietala, "A Study of MIS Coplanar Slow-Wave Transmission Lines on Silicon," University of Minnesota, Minneapolis, MN, Ph.D. Dissertation, Aug., 1988.
- [7] V. M. Hietala and K. S. Champlin, "Measurement of the Microwave Properties of Micron-Sized Coplanar Transmission Lines," *Journal of Electromagnetic Waves and Applications*, vol. 5, no. 4/5, pp. 439-452, 1991.
- [8] EEsof, Inc., *LineCalc*. Westlake Village, CA: EEsof, 1991.
- [9] K. S. Giboney, M. J. W. Rodwell, and J. E. Bowers, "Traveling-Wave Photodetectors," *IEEE Photon. Technol. Lett.*, vol. 4, no. 12, pp. 1363-1365, Dec., 1992.
- [10] J. E. Bowers and C. A. Burrus, Jr., "Ultrawide-Band Long-Wavelength p-i-n Photodetectors," *J. Lightwave Technol.*, vol. 5, no. 10, pp. 1339-1350, Oct., 1987.
- [11] A. Alping, "Waveguide pin Photodetectors: Theoretical Analysis and Design Criteria," *IEE Proc. J*, vol. 136, no. 3, pp. 177-182, Jun., 1989.
- [12] Y. G. Wey, D. L. Crawford, K. Giboney, J. E. Bowers, M. J. Rodwell, P. M. Sylvestre, M. J. Hafich, and G. Y. Robinson, "Ultrafast Graded Double-Heterostructure GaInAs/InP Photodiode," *Appl. Phys. Lett.*, vol. 58, no. 19, pp. 2156-2158, May 13, 1991.

- [13] J. G. Wasserbauer, J. E. Bowers, M. J. Hafich, P. Silvestre, L. M. Woods, and G. Y. Robinson, "Specific Contact Resistivity Of InGaAs/InP p-Isotype Heterojunctions," *Electron. Lett.*, vol. 28, no. 17, pp. 1568-1570, Aug. 13, 1992.
- [14] Y. G. Wey, K. Giboney, J. Bowers, M. Rodwell, P. Silvestre, P. Thiagarajan, and G. Robinson, "110 GHz GaInAs/InP Double Heterostructure p-i-n Photodetectors," *J. Lightwave Technol.*, vol. 13, no. 7, pp. 1490-1499, Jul., 1995.
- [15] S. Luryi, "Hot-Electron Transistors," in *High-Speed Semiconductor Devices*, S. M. Sze, ed. New York: John Wiley & Sons, 1990, pp. 399-461.
- [16] S. Tiwari, *Compound Semiconductor Device Physics*. San Diego: Academic Press, 1992.
- [17] J. Singh, *Physics of Semiconductors and Their Heterostructures*. New York: McGraw-Hill, 1993.
- [18] S. Luryi, "Device Building Blocks," in *High-Speed Semiconductor Devices*, S. M. Sze, ed. New York: John Wiley & Sons, 1990, pp. 57-136.
- [19] D. Lee, *Electromagnetic Principles of Integrated Optics*. New York: John Wiley & Sons, 1986.
- [20] D. Marcuse, *Theory of Dielectric Optical Waveguides*, 2nd ed. San Diego: Academic Press, 1991.
- [21] S. Adachi, "Optical Properties of AlGaAs: Transparent and Interband-Transition Regions (Tables)," in *Properties of Aluminium Gallium Arsenide*, S. Adachi, Ed. London: INSPEC, 1993, pp. 125-140.
- [22] N. Chand, T. Henderson, J. Klem, W. T. Masselink, R. Fischer, Y. C. Chang, H. Morkoç, "Comprehensive analysis of Si-doped  $\text{Al}_x\text{Ga}_{1-x}\text{As}$  ( $x = 0$  to 1): Theory and experiments," *Phys. Rev. B*, vol. 30, no. 8, pp. 4481-4492, Oct. 15, 1984.
- [23] T. C. Shen, G. B. Gao, and H. Morkoç, "Recent developments in ohmic contacts for III-V compound semiconductors," *J. Vac. Sci. Technol. B*, vol. 10, no. 5, pp. 2113-2132, Sep./Oct., 1992.
- [24] B. J. Sealy, "Ion Ranges in GaAs: Discussion," in *Properties of Gallium Arsenide*, 2nd ed. London: INSPEC, 1990, pp. 689-691.
- [25] R. P. Webb and B. J. Sealy, "Range Profile Statistics for Ions in GaAs," in *Properties of Gallium Arsenide*, 2nd ed. London: INSPEC, 1990, pp. 692-697.
- [26] F. Ren, S. J. Pearton, W. S. Hobson, T. R. Fullowan, J. Lothian, and A. W. Yanof, "Implant isolation of GaAs-AlGaAs heterojunction bipolar transistor structures," *Appl. Phys. Lett.*, vol. 56, no. 9, pp. 860-862, Feb. 26, 1990.
- [27] J. F. Gibbons, W. S. Johnson, and S. W. Mylroie, *Projected Range Statistics*, 2nd ed. Stroudsburg: Dowden, Hutchinson & Ross, 1975.
- [28] EEsof, Inc., *Academy*. Westlake Village, CA: EEsof, 1991.

- [29] Photo Sciences, Torrance, CA.
- [30] G. L. Snider, *1D Poisson/Schrödinger*, University of California, Santa Barbara, CA.
- [31] I-H. Tan, G. L. Snider, L. D. Chang, and E. L. Hu, "A self-consistent solution of Schrödinger-Poisson equations using a nonuniform mesh," *J. Appl. Phys.*, vol. 68, no. 8, pp. 4071-4076, Oct. 15, 1990.
- [32] B. L. Sharma, "Diffusion Data for Semiconductors," in *CRC Handbook of Chemistry and Physics*, D. R. Lide, Ed., 74th ed. Boca Raton, FL: CRC Press, 1993, pp. 12-89 - 12-99.
- [33] R. E. Williams, *Modern GaAs Processing Methods*. Boston: Artech House, 1990.
- [34] G. A. Vawter, L. A. Coldren, J. L. Merz, and E. L. Hu, "Nonselective etching of GaAs/AlGaAs double heterostructure laser facets by Cl<sub>2</sub> reactive ion etching in a load-locked system," *Appl. Phys. Lett.*, vol. 51, no. 10, pp. 719-721, Sep. 7, 1987.
- [35] Y. G. Wey, "High-Speed Double Heterostructure GaInAs/InP p-i-n Photodiodes: Theory, Fabrication, and Measurement," University of California, Santa Barbara, CA, Ph.D. Dissertation, Feb., 1993.
- [36] Y. Lu, T. S. Kalkur, and C. A. Paz de Araujo, "Rapid Thermal Alloyed Ohmic Contacts to p-Type GaAs," *J. Electrochem. Soc.*, vol. 136, no. 10, pp. 3123-3129, Oct., 1989.
- [37] SAL-110, Shipley, Marlborough, MA.
- [38] S. J. Pearton, M. P. Iannuzzi, C. L. Reynolds, Jr., and L. Peticolas, "Formation of thermally stable high-resistivity AlGaAs by oxygen implantation," *Appl. Phys. Lett.*, vol. 52, no. 5, pp. 395-397, Feb. 1, 1988.
- [39] S. J. Pearton, J. M. Poate, F. Sette, J. M. Gibson, D. C. Jacobson, and J. S. Williams, "Ion Implantation in GaAs," *Nucl. Instrum. Methods*, vol. B19/20, pp. 369-380, 1987.
- [40] IICO Corp., Santa Clara, CA.
- [41] Microposit 1165 Remover, Shipley, Marlborough, MA.
- [42] Probamide 284, CIBA-GEIGY Corp., Santa Clara, CA.
- [43] M. Otsubo, T. Oda, H. Kumabe, and H. Miki, "Preferential Etching of GaAs Through Photoresist Masks," *J. Electrochem. Soc.*, vol. 123, no. 5, pp. 676-680, May, 1976.
- [44] G. C. DeSalvo, W. F. Tseng, and J. Comas, "Etch Rates and Selectivities of Citric Acid/Hydrogen Peroxide on GaAs, Al<sub>0.3</sub>Ga<sub>0.7</sub>As, In<sub>0.2</sub>Ga<sub>0.8</sub>As, In<sub>0.53</sub>Ga<sub>0.47</sub>As, In<sub>0.52</sub>Al<sub>0.48</sub>As, and InP," *J. Electrochem. Soc.*, vol. 139, no. 3, pp. 831-835, Mar., 1992.
- [45] C. Juang, K. J. Kuhn, and R. B. Darling, "Selective etching of GaAs and Al<sub>0.30</sub>Ga<sub>0.70</sub>As with citric acid/hydrogen peroxide solutions," *J. Vac. Sci. Technol. B*, vol. 8, no. 5, pp. 1122-1124, Sep./Oct., 1990.
- [46] Norland Optical Adhesive 61, Norland Products, Inc., New Brunswick, NJ.

## CHAPTER 4

# ELECTRO-OPTIC MEASUREMENT TECHNIQUES

The goal of a measurement is to accurately characterize a performance aspect of a component or system in a specified environment, usually that of the final application. This means that the device under test (DUT) and the measurement system together must form a system that approximates the device in its application environment. With this in mind, the design of any component or system should include provisions for characterization.

Measurement considerations demand particular attention when novel ideas are to be demonstrated since new measurement techniques may be required. The interactions of device and measurement are accounted for in all phases of development of the travelling-wave photodetector (TWPD). A detailed understanding of the measurement technologies is prerequisite not only to interpreting the measurement results, but also to appreciating critical design and fabrication features.

The construction of an electro-optic (EO) sampling system was integrated into this thesis work. EO sampling is uniquely suited to photodetector measurements and is used to measure photodetector impulse responses up to bandwidths of greater than 1 THz. Some excellent summary articles describe EO sampling and some of its applications [1-3]. The basics and new developments important for photodetector measurements will be presented here.

### 4.1 Electro-Optic Probe Station

A critical part of a microelectronic measurement system is the physical interface between the DUT and the measurement instrument. Through this interface, the measurement system is incorporated into the circuit of the DUT. This circuit can be completed via wires or cables connected to needle probes contacting pads on a microcircuit. This arrangement is sufficient at low frequencies because the interface distances can be short compared to the wavelengths of concern.

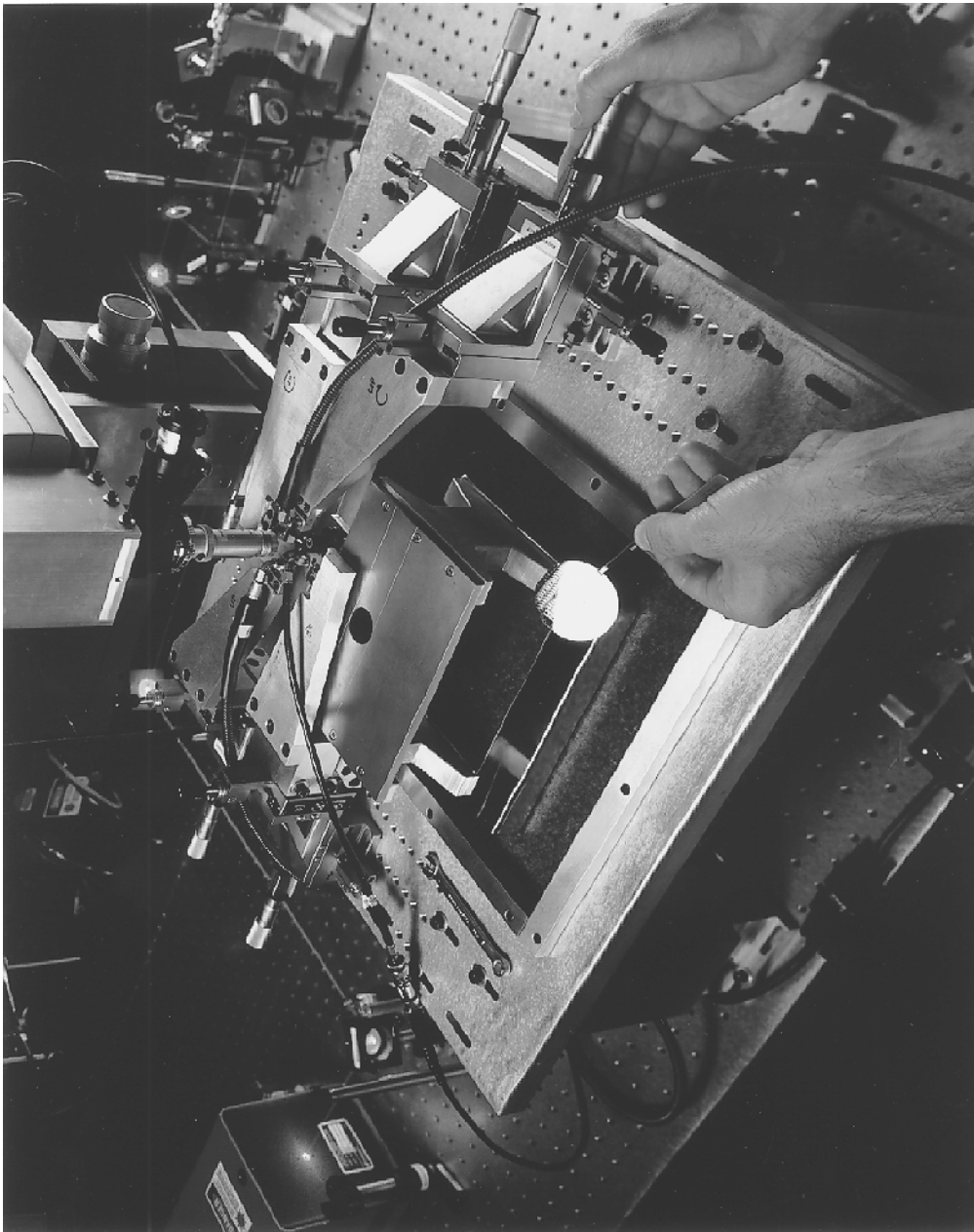


Fig. 4.1 EO probe station on an optical bench. This measurement platform provides for precision positioning of four microwave probes, optical inputs and outputs from the top and bottom, and an optical input from the side.

Wave propagation effects become important when distances exceed a quarter wavelength. Guiding structures are generally used to make connections in this regime. Microwave probes became commercially available in the mid 1980s to facilitate measurements of microwave circuits [4]. Microwave probe stations greatly increased the efficiency and accuracy of monolithic microwave integrated circuit

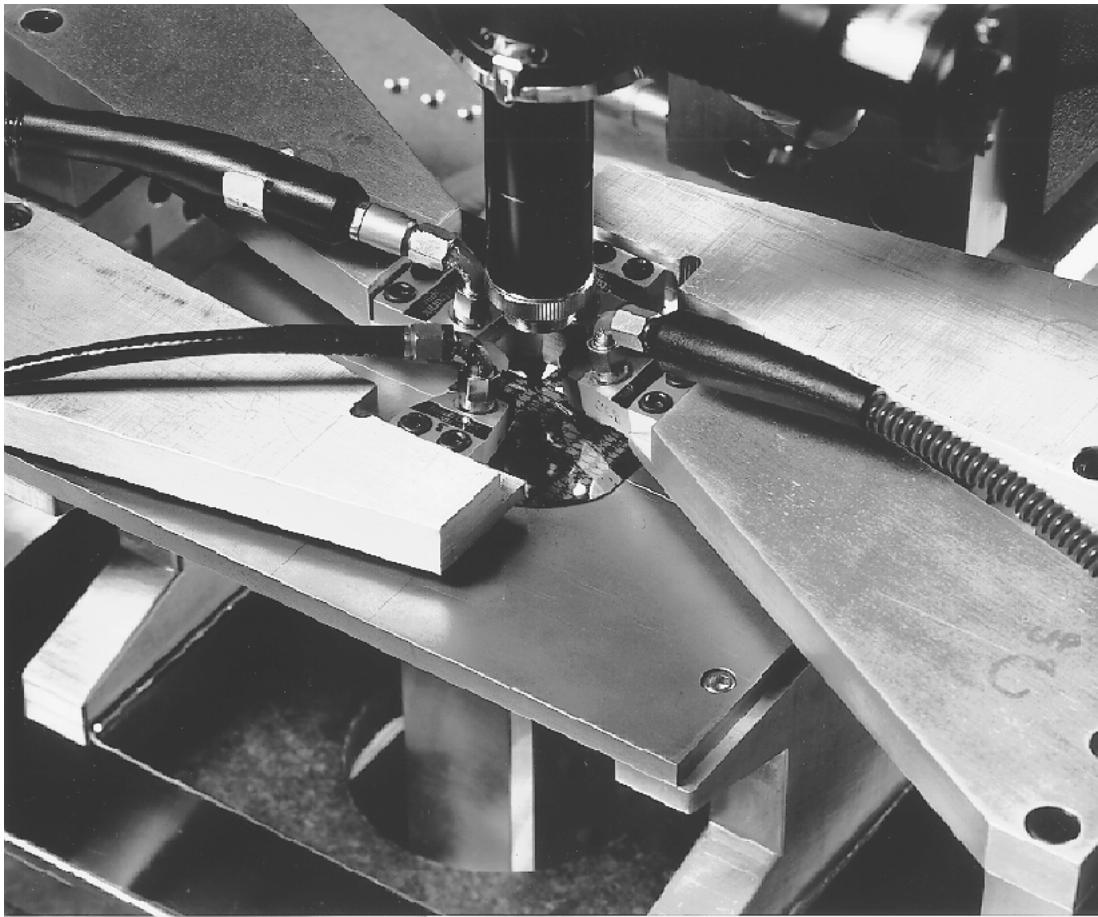


Fig. 4.2 Close-up of EO probe station, showing microwave probes and a wafer DUT on the stage. The objective for the viewing microscope is above.

development by encouraging standardization of microcircuit layout and eliminating the need for special fixturing to make measurements.

At the inception of this work, measurement platforms that accommodated both electrical and optical signals were not commercially available, so a custom EO probe station was designed and constructed. This probe station, shown in Fig. 4.1, attaches to the top of an optical bench and accommodates several electrical and optical inputs and outputs in a variety of configurations. Its intended purpose is to provide a universal EO measurement platform. Versatility, ease of use, stability, and maximum use of standardized hardware were of prime concern in its design. This station has

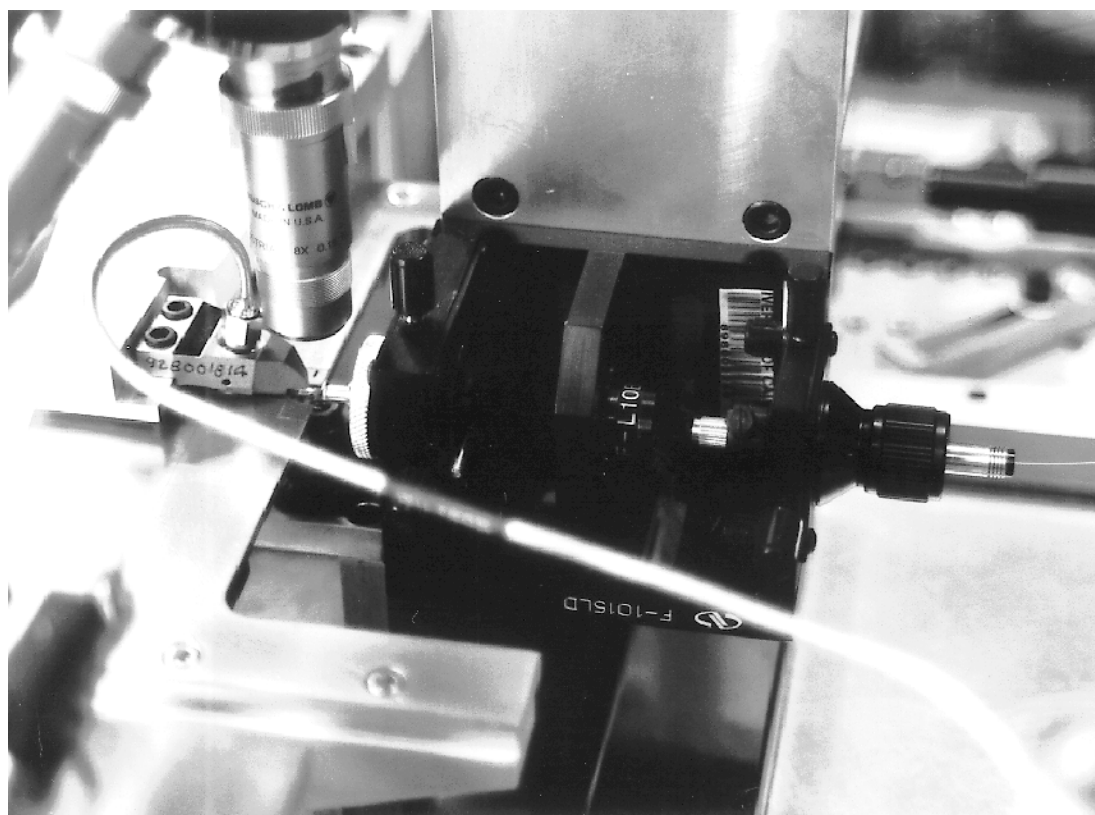


Fig. 4.3 In-plane coupler for delivering light to in-plane-illuminated devices. The fiber can be seen at right. A collimating lens is located in the middle of the black mount. The focussing lens housing is the thin, bright, silver-colored protrusion on the left side of the black mount. The negative translation lens is inside the black housing immediately to the right of the focussing lens.

been a used for a variety of projects [5-16], and it should adapt easily to future applications.

Up to four microwave probes can be installed on the EO probe station, as shown in Fig. 4.2. They mount on custom arms attached to precision linear translation stages with micrometer actuators. A screw and lock rotational adjustment provides for planarization. Magnetic base needle probe positioners can be mounted on platforms.

A free-space optical path from below the sample is used as the input and output for an EO sampling beam and as the input for bottomside-illuminated devices. The two beams are simultaneously directed through the same optics, and the angle between the two beams determines the separation of the focussed spots. The absolute position of the beams in the plane of the DUT is adjusted by two turning mirrors

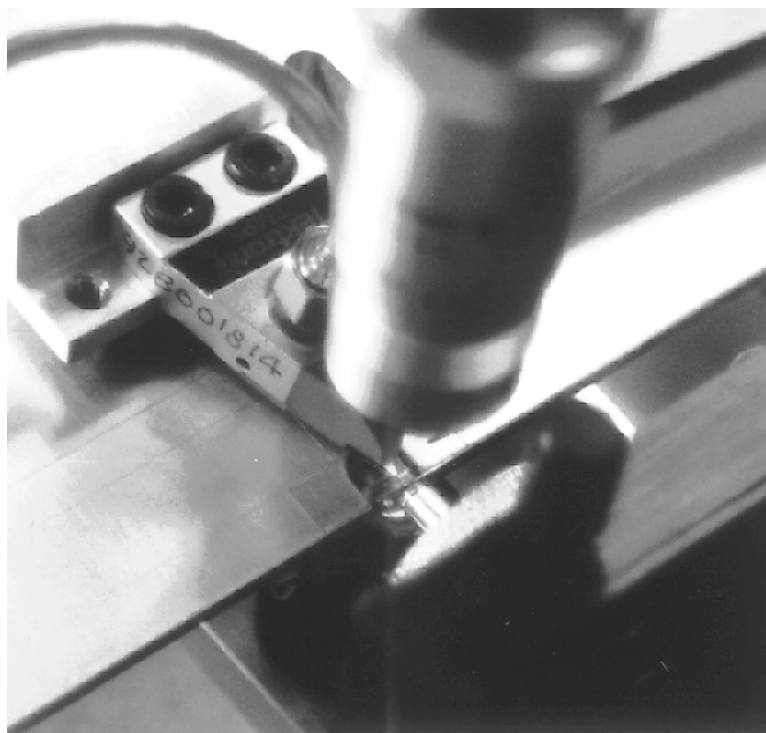


Fig. 4.4 Close-up showing focussing lens of in-plane coupler and TWPD sample. The bottomsides focussing lens can be partially seen underneath the TWPD sample.

attached to two precision linear translation stages mounted one on the other. The focussing lens distance from the DUT is adjusted by another stage mounted to the second turning mirror stage. This bottomsides beam path is used for EO sampling of coplanar waveguide circuits [5-9] and for pump-probe EO sampling of backside-illuminated optoelectronic devices [10-12].

A topside optical input/output path is coaxial with the microscope viewing optics. An optical fiber carries light from the beam level on the optical bench to an output coupler that directs the beam path through the viewing optics. Infrared light passes through a long-pass dichroic beamsplitter also used as a turning mirror to direct the DUT image toward a video camera. A second beamsplitter is used to reflect diffuse viewing illumination onto the DUT from an incandescent bulb. This beamsplitter also provides an output port for light coming from the DUT. Light is focussed onto the DUT by the microscope objective lens. The focus of the beam relative to the microscope image is adjustable with a lens in the fiber output coupler. This topside

beam path is used to measure topside-illuminated photodetectors [13-14], and surface-normal reflection modulators [15].

An additional capability of doing EO sampling from the topside was included in an EO probe station designed for Hughes Research Laboratories in Malibu, CA. Polarization optics and a photoreceiver required for EO sampling were built into the microscope arrangement of this probe station, allowing EO probing of microstrip circuits.

A side-illumination path provides delivery of light to in-plane illuminated devices. Similarly to the topside arrangement, an optical fiber carries light from the beam level on the optical bench to a coupler. A molded aspheric lens [17] at the coupler output focusses the beam onto the DUT. The coupler, shown in Figs. 4.3 and 4.4, is mounted to a three-axis linear translation stage with manual micrometer actuators on two axes. A DC servo actuator is mounted on the axis of the translation stage parallel to the beam propagation to give submicron resolution necessary for the short depth of field of the focussing lens. Submicron positioning perpendicular to the beam propagation is achieved by placing a long focal length negative lens on a two-axis stage near the back focal plane of the focussing lens. When the negative lens is moved, the focussed beam spot moves with a translational reduction equal to the ratio of the focal lengths of the lenses [18]. This side-illumination path is used to stimulate TWPDs and WGPDs [16].

The DUT is placed on a stage that slides freely on a slab of ultraflat black granite. The granite is flat to within 1/10,000 of an inch to eliminate wobble or variation in the angle or height of the stage when it is moved. The stage is positioned directly by hand, and can be seen clearly in Figs. 4.1 & 4.2. A modified version for use with the in-plane illuminated devices can be seen in Fig. 4.3.

## 4.2 Electro-Optic Sampling

A photodetector is characterized as a two port device with an optical input and an electrical output. As a linear system, a photodetector is completely described by the impulse response in units of (electrical current)/(optical energy), or alternatively by the frequency response in units of (electrical charge)/(optical energy) or (electrical current)/(optical power). These descriptions are dual if the frequency response is a

complex quantity. The objective of a photodetector measurement is to yield such a description.

The duration of a state-of-the-art high-speed photodetector impulse response is of the order of a few picoseconds, having significant frequency components extending to hundreds of gigahertz. Mode-locked laser sources that deliver sub-picosecond light pulses are now common, however instruments for measuring electrical signals on such a short time scale are not commercially available.

Electrical measurement bandwidths appear to be currently limited by the interface, i.e. probes, connectors, cables. These issues are being addressed in current research [19-25]. Most electrical measurement techniques are aimed at all-electrical systems, with which synchronization is relatively easy. The measurement system must be synchronized with the stimulus to simultaneously achieve large bandwidth and good sensitivity [9]. Subpicosecond timing synchronization of most mode-locked lasers with an independent electrical system currently requires an optoelectronic feedback circuit [26]. High repetition rate mode-locked semiconductor lasers, however, do not require such a circuit [27].

Pump-probe type measurements solve the timing synchronization dilemma by deriving stimulus and sampling pulses from the same source, so they are inherently synchronized. For photodetector measurements, a high-bandwidth method for converting electrical signals to optical signals or vice versa is then required. The electro-optic effect provides such a means for converting an electrical signal to an optical signal, and it is the basis for EO sampling.

The electro-optic effect is the modulation of the index ellipsoid by an applied electric field. Much of the following description of electro-optic modulation is detailed in [28]. This electro-optic effect occurs in non-centrosymmetric crystals due to redistribution of bound charges in the presence of an electric field. Many materials that are popular for high-speed electronics and optoelectronics such as GaAs, AlAs, and InP are electro-optic. Silicon is not. Ionic response contributes at low frequencies (<100 kHz) through the piezoelectric and elasto-optic effects. The bound electronic contribution is constant from DC to near the lattice resonance frequency, which is greater than 7.6 THz in all AlGaAs alloys [29].

The index ellipsoid is proportional to the surfaces of constant energy in  $D$  space, and describes the index of refraction as a function of polarization. In the principle coordinate system, the index ellipsoid is given by

$$\frac{x^2}{n_x^2} + \frac{y^2}{n_y^2} + \frac{z^2}{n_z^2} = 1 \quad (4.1)$$

where  $1/n_x^2$ ,  $1/n_y^2$ , and  $1/n_z^2$  are the principle values of the impermeability tensor,  $\eta_{ij}$ . The index ellipsoid can alternatively be written in terms of the impermeability tensor,  $\eta_{ij}x_i x_j = 1$ , where  $x_i$  and  $x_j$  refer to the coordinate axes.

The linear electro-optic or Pockels effect is defined as a first order perturbation of the impermeability tensor by the electric field. A term proportional to the electric field is included in the impermeability tensor, and the index ellipsoid becomes

$$\left[ \eta_{ij}(0) + r_{ijk} E_k \right] x_i x_j = 1 \quad (4.2)$$

with the proportionality constant given by the electro-optic tensor,  $r_{ijk}$ . The high- and low-frequency electro-optic tensors are distinguished by the labels "S" and "T". The "T" values include the ionic contribution.

If the medium is not optically active or absorbing, the impermeability tensor must be symmetric. This implies that the first two indices of the electro-optic tensor can be permuted. Thus, the indices can be contracted,  $r_{(ij)k} \rightarrow r_{ij}$ , and the number of elements is reduced from 27 to 18. Crystal symmetry further requires that many of these elements be zero.

Zinc-blende crystals, such as GaAs and AlAs, belong to the  $\bar{4}3m$  symmetry group with index ellipsoid given by

$$\frac{x^2 + y^2 + z^2}{n^2} + 2r_{41}(E_x yz + E_y xz + E_z xy) = 1 \quad (4.3)$$

where  $n$  is the unperturbed index of refraction. An electric field only in the x or [100] direction causes the index ellipsoid to become,

$$\frac{x^2}{n^2} + \left( \frac{1}{n^2} + r_{41} E_x \right) y^2 + \left( \frac{1}{n^2} - r_{41} E_x \right) z^2 = 1 \quad (4.4)$$

where the primed principle axes are rotated by  $\pi/4$  about the x-axis. The indices of the polarization eigenmodes are  $n_x = n$ ,  $n_{y'} \approx n - n^3 r_{41}^S E_x / 2$ , and  $n_{z'} \approx n + n^3 r_{41}^S E_x / 2$ . Electric field components in the [011] direction do not modulate the index for beams propagating in the [100] direction.

The phase retardation between the two eigenpolarizations of the propagation direction,  $\Gamma = \pi V / V_\pi$ , is proportional to the potential difference along the path through the electro-optic medium.  $V_\pi = \lambda / 2n^3 r_{41}^S$  is the half-wave voltage. At wavelength,  $\lambda = 0.96 \mu\text{m}$ ,  $n = 3.5$  and  $r_{41}^S = -1.73 \text{ pm/V}$  in GaAs, so  $V_\pi = 6.2 \text{ kV}$  [30].  $\text{Al}_{0.5}\text{Ga}_{0.5}\text{As}$  is used in measurements at  $\lambda = 0.83 \mu\text{m}$  described in later chapters. Values of  $r_{41}^S$  for AlGaAs or AlAs have not been reported, however it has been postulated that values for GaP should be a reasonable approximation for AlAs due to the similarity in band structure [30]. In GaP,  $r_{41}^S \approx -0.88 \text{ pm/V}$  at  $\lambda = 0.83 \mu\text{m}$ . The index of  $\text{Al}_{0.5}\text{Ga}_{0.5}\text{As}$  is 3.3 at that wavelength, so  $V_\pi \approx 8.1 \text{ kV}$  in  $\text{Al}_{0.5}\text{Ga}_{0.5}\text{As}$  at  $\lambda = 0.83 \mu\text{m}$ .

The optical phase modulation can be converted to amplitude modulation by polarization optics, yielding a photocurrent consisting of a DC term plus a term proportional to the potential difference along the beam path,

$$i_{photo} = I_0 [1 + \sin(\Gamma)] \approx I_0 \left( 1 + \frac{\pi V}{V_\pi} \right). \quad (4.5)$$

Thus, the measured photocurrent is linearly related to the potential difference along the optical path through the electro-optic crystal.

Signals on coplanar waveguide (CPW) can be probed using the scheme shown in Fig. 4.5. Elliptically polarized light is focussed through the backside of the sample and the beam reflects from the center conductor, returning on the same path. The eigenpolarizations accumulate relative phase shift as they pass through field regions in the substrate in both directions. The double pass reduces  $V_\pi$  by one half.

Short pulses of light sample a repetitive electrical signal in EO sampling. The measured signal is downconverted by synchronous sampling, as depicted in Fig. 4.6. The sampled frequency is the offset or difference frequency between the signal frequency and the closest harmonic of the sampling pulse repetition rate,

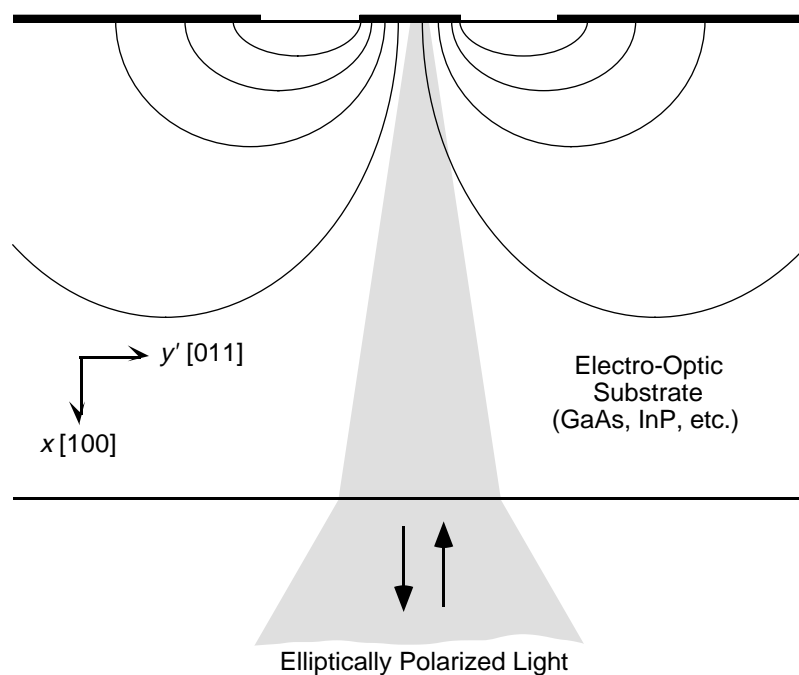


Fig. 4.5 Scheme for electro-optic probing of signals on coplanar waveguide.

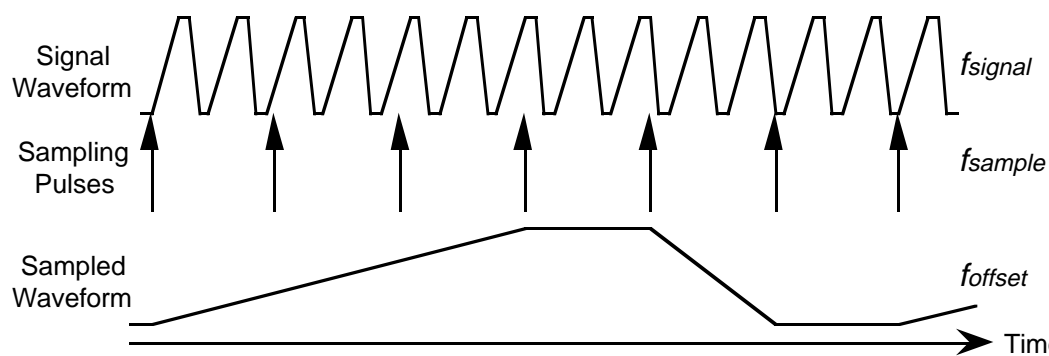


Fig. 4.6 Illustration of synchronous sampling. A repetitive signal is downconverted to a lower frequency by sampling and integrating across signal waveform periods.

$f_{offset} = f_{signal} - mf_{sample}$ . In the case of pump-probe measurements, which are used for measuring photodetectors,  $m = 1$ .

### 4.3 System Response

The EO sampling system response can be limited by any of several effects. The major components are the optical pulse profile, timing and frequency jitter, electro-optic interaction response, and signal processing response. The stimulus (pump) and sampling (probe) pulses originate from the same source in pump-probe measurements used for photodetectors. Thus, the pulses are inherently synchronized, and timing and frequency jitter are nil. The signal processing scheme is designed to achieve the desired sensitivity and signal-to-noise ratio with negligible effect on the system response. The remaining effects are significant for EO sampling measurements of photodetectors: optical pulse profile and electro-optic interaction response.

The electro-optic interaction response is determined by the time required for modulation of the polarization state of the probe beam. It is composed of the electro-optic effect response, the electrical transit response, and the optical transit response. The electro-optic effect response is determined by the lattice resonance frequency mentioned in Sec. 4.2, and can be safely ignored. The electrical signal usually travels normal to the optical sampling beam path at greater than  $100 \mu\text{m}/\text{ps}$ , so it passes across the beam cross-section in the electrical transit time, less than 30 fs for an average beam spot size of less than  $3 \mu\text{m}$ . This response component can also be neglected. The dominant electro-optic interaction response component for most geometries is the optical transit response, and it is determined by the time required for the sampling beam to traverse the electric fields extending into the electro-optic crystal, as depicted in Fig. 4.5 [2, 31].

The optical transit impulse response for CPW is derived by considering electrical impulses travelling on the transmission line and optical sampling impulses in a beam of impulsive spatial cross-section. Given pure TEM-mode propagation, the fields from the electrical impulses extend into the electro-optic substrate in a plane and they cross the beam path in an infinitesimal time. The electric field is sampled at the location of the optical impulse at that time. The resulting waveform from EO sampling is then the electric field profile under the transmission line.

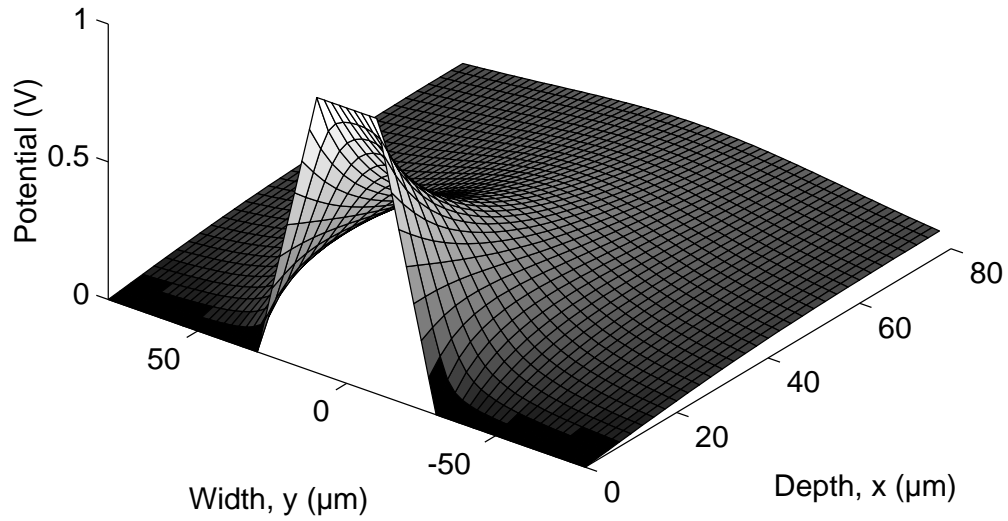


Fig. 4.7 Potential under coplanar waveguide with center conductor width and gap width of 20  $\mu\text{m}$ .

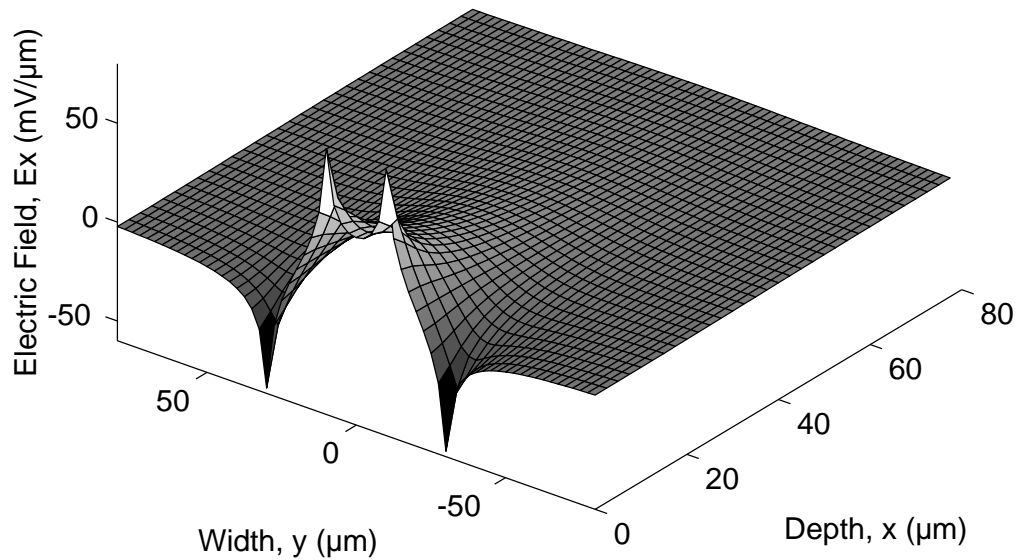


Fig. 4.8 Electric field x-component under coplanar waveguide with center conductor width and gap width of 20  $\mu\text{m}$ .

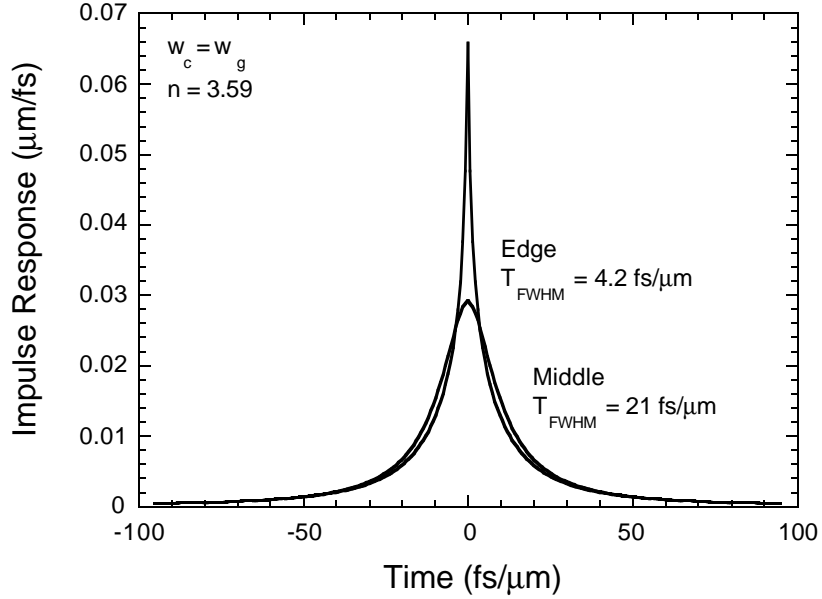


Fig. 4.9 Optical transit impulse responses for substrate probing at the edge and in the middle of coplanar waveguide on GaAs.

For direct EO sampling in a (100) substrate, the optical transit impulse response is found from the normal electric field profile,  $\vec{E}_x(x)$ , with the substitution  $t = |x|/v_o$ , where  $v_o \approx c/n$  is the optical group velocity in the substrate. A quasi-static solution of the potential under CPW for a simple case can be found by solving Laplace's equation,  $\nabla^2 V = 0$ , in the regions of the dielectric. For the ideal case of infinitesimally thick, perfect conductors and semi-infinite dielectrics, the boundary conditions are determined by the potential in the plane of the conductors and at infinity. The solution is a sum of modes expressed by an inverse Fourier transform  $v(x, y) = F_y^{-1}\{Y(k)e^{-kx}\}$ , where  $Y(k) = F_y\{v(0, y)\}$ .

The potential and x-component of the electric field in the region under CPW are plotted in Figs. 4.7 and 4.8. The sharp peaks in the plot of  $\vec{E}_x$  suggest radically different optical transit responses from probing at an edge and in the middle of the center conductor [31]. This is verified by comparing the optical transit impulse responses at the edge and middle in Fig. 4.9. However, the differences in impulse responses have little effect on the step or frequency responses, plotted in Figs. 4.10

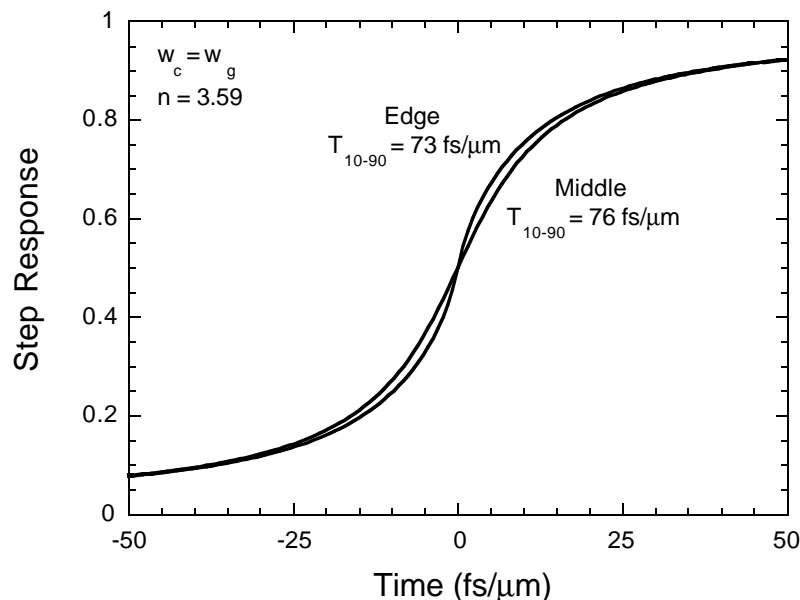


Fig. 4.10 Optical transit step responses for substrate probing at the edge and in the middle of coplanar waveguide on GaAs.

and 4.11. The step and frequency responses are much more meaningful gauges of the limitations on fidelity.

The optical transit step/frequency response is directly/inversely proportional to the transmission line dimensions. Figs. 4.9-4.11 are plotted using normalized scales so that characteristic times/frequencies for CPW of arbitrary dimensions can be found by multiplying/dividing by a characteristic width, given by  $w' = (w_c + w_g)/2$ , where  $w_c$  and  $w_g$  are the center conductor and gap widths in microns. This method will give approximate results for center conductor width to gap width ratios of 1:1/2 to 1:2 or greater. For more accurate solutions, a numerical model accounting for finite conductor and dielectric layer thicknesses should be employed.

#### 4.4 Deconvolution

Distortions due to system response components such as optical pulse shape and optical transit response can be removed by deconvolving them from the measured waveform. Synchronous sampling can be viewed mathematically as correlation of the signal and sampling pulses and downconversion of the resultant waveform.

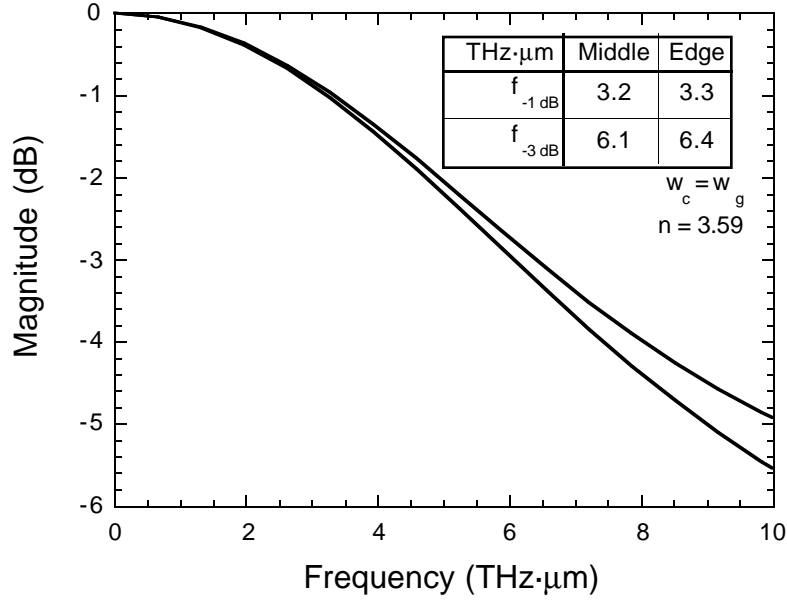


Fig. 4.11 Optical transit frequency responses for substrate probing at the edge and in the middle of coplanar waveguide on GaAs.

However, the signal being sampled is not simply the signal propagating on the transmission line, but rather that signal convolved with the optical transit impulse response.

A conceptual system diagram for pump-probe measurement is drawn in Fig. 4.12(a). Ignoring the downconversion, the system equation is

$$m = p_1 * h_{DUT} * h_{OT} \otimes p_2 \quad (4.6)$$

where  $m$  is the measured waveform,  $p_1$  and  $p_2$  represent the pump and probe optical pulses,  $h_{DUT}$  and  $h_{OT}$  represent the DUT and optical transit responses, and  $*$  and  $\otimes$  designate convolution and correlation operations. By considering the input to the system to be the DUT response, as depicted in Fig. 4.12(b), the pump-probe EO sampling system response is

$$h_{PP} = p_1 \otimes p_2 * h_{OT}. \quad (4.7)$$

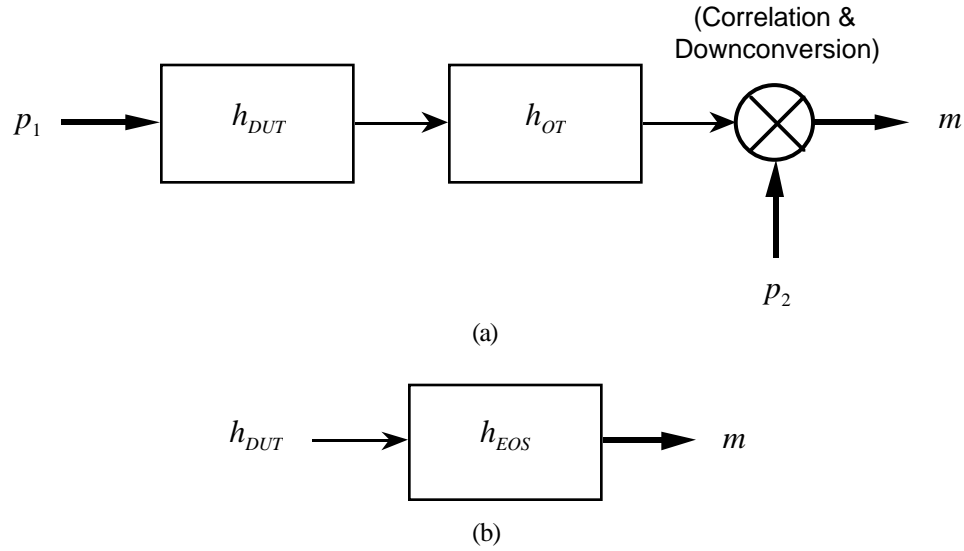


Fig. 4.12 Conceptual system diagrams for pump-probe EO sampling showing (a) individual system components, and (b) EO sampling system response.

While very short optical pulses are not directly measurable, autocorrelation measurements of such pulses are routine and cross-correlations are done, as well [32-33]. The most common type of optical correlation measurement makes use of sum frequency generation in a nonlinear optical crystal to perform synchronous sampling. This measurement technique is completely analogous to pump-probe EO sampling except that all inputs and outputs are optical. Using the results of such a measurement and the calculated optical transit response, the pump-probe EO sampling system response in (4.7) can be determined.

The DUT impulse response can now be found by deconvolving the pump-probe EO sampling system response from the measured signal. This is most easily performed by dividing in the frequency domain,

$$H_{DUT} = \frac{M}{H_{PP}} = \frac{M}{P_1 P_2^* H_{OT}} \quad (4.8)$$

and then inverse transforming for the time-domain result.

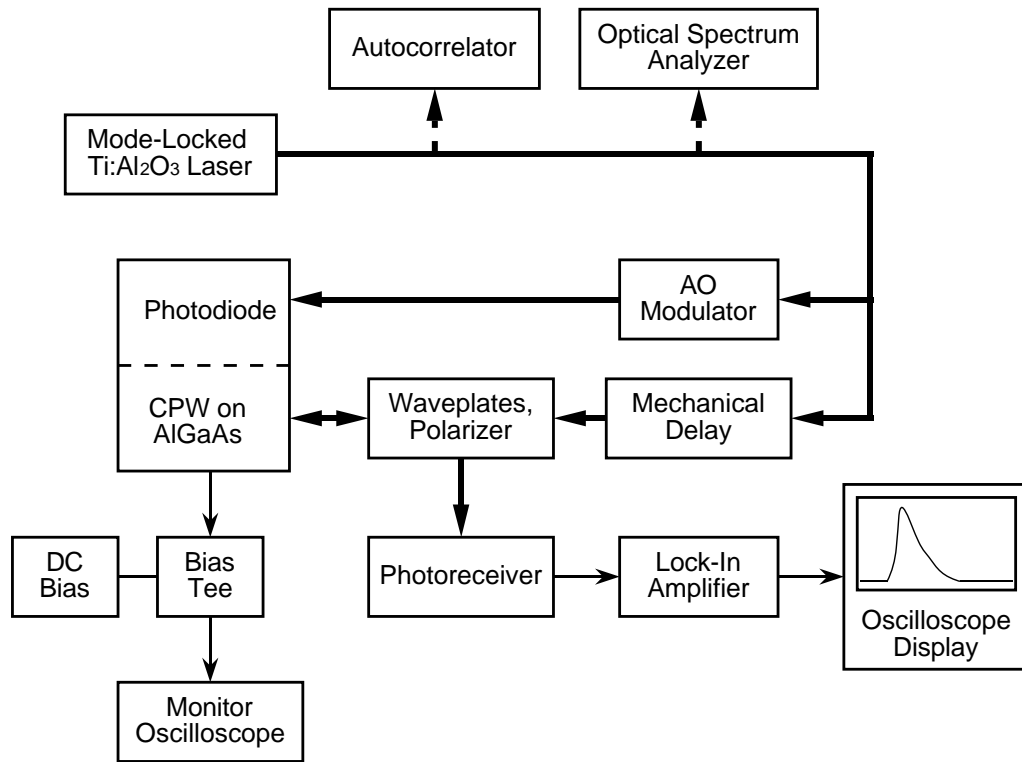


Fig. 4.13 Pump-probe EO sampling system for measuring high-speed photodetectors. The lock-in amplifier and acousto-optic (AO) modulator share a common frequency reference.

#### 4.5 Noise & Interference

The signal magnitude from EO sampling is very small in the usual case when  $V \ll V_{\pi}/\pi$ . In addition, low-frequency amplitude noise from laser systems is generally many orders of magnitude larger than the shot-noise limit. As a result, some type of noise reduction scheme is requisite for signal recovery.

There are several methods for eliminating amplitude noise. Reasonable candidates for EO sampling include chopping with lock-in detection [3], probe beam polarization modulation [34], and noise subtraction [35]. The lock-in technique is a standard laboratory method for which commercial equipment is available to perform the more complex and delicate tasks of demodulating and amplifying the signal. Probe beam polarization modulation is a technique specific to EO sampling that is claimed to offer a factor of two signal-to-noise ratio improvement over conventional methods. Noise

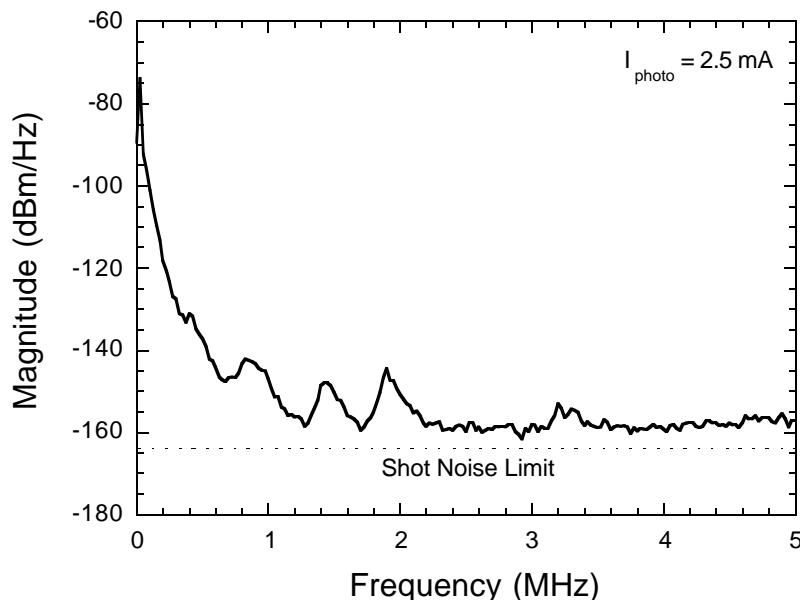


Fig. 4.14 Typical amplitude noise spectrum of the Ti:sapphire laser used for EO sampling measurements.

subtraction cancels noise electronically using a reference beam. This method has the advantages of low cost and compatibility with the other noise reduction schemes.

The chopping and lock-in detection scheme used for measurements in this work is depicted in the EO sampling system diagram in Fig. 4.13. The light source is a passively mode-locked Ti:sapphire laser [36]. The pump light is chopped via an acousto-optic (AO) modulator [37]. The mechanical delay provides the offset frequency for sampling. The waveplates convert the incoming sampling beam to a prescribed elliptical polarization state, and then the waveplates and polarizer convert the optical phase modulation of the return beam to amplitude modulation. The photoreceiver converts the optical signal to electrical and amplifies it. The lock-in amplifier demodulates and further amplifies the signal for viewing on a low-speed oscilloscope.

The amplitude noise spectrum of the Ti:sapphire laser at 2.5 mA photocurrent is shown in Fig. 4.14. The noise drops to a floor about 5 dB above the shot-noise limit at around 2.2 MHz. A chopping frequency of 1 MHz was chosen for convenience.

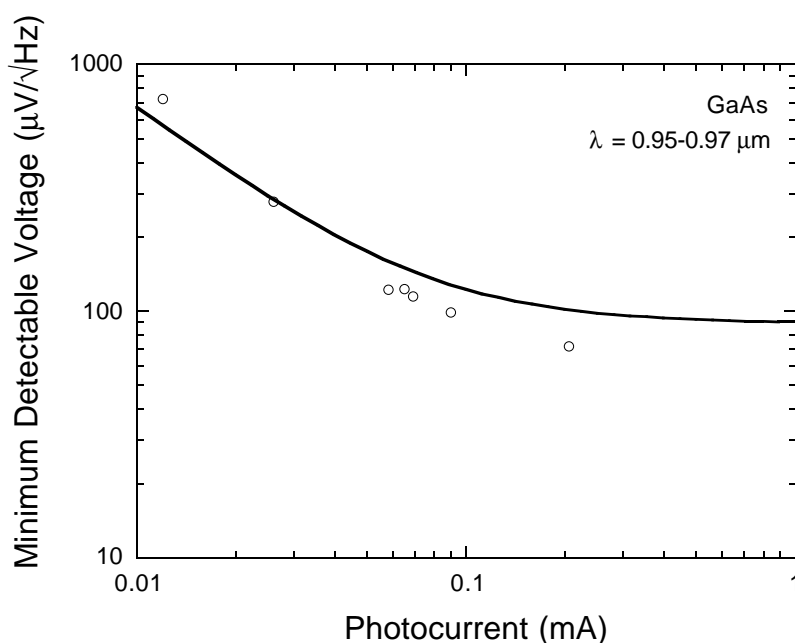


Fig. 4.15 Minimum detectable voltage of EO sampling system in GaAs at 1 MHz versus DC photocurrent detected by system photoreceiver. Line is calculated from theory and measured system parameters. Data points are direct measurements.

The amplitude noise is 18 dB above the shot noise at this frequency in Fig. 4.14, although it varies considerably depending on the laser tuning.

The photoreceiver is custom-built and uses a high-bias silicon photodetector with a net resistive load of 1.6 k $\Omega$  and about 24 dB of gain. The bandwidth is estimated to be greater than 5 MHz. The rms input-referred noise current is 6.5 pA/ $\sqrt{\text{Hz}}$ , so the photoreceiver noise is equal to the beam shot noise at a photocurrent of 0.13 mA.

The measurement sensitivity is limited by photoreceiver noise, shot noise of the detected light, and laser amplitude noise. The minimum detectable voltage is expressed as

$$v_{min} = \frac{V_{\pi}}{\pi} \sqrt{\frac{\overline{i_{Nin}^2}}{I_0^2} + \frac{2q}{I_0} + M_{AM}^2} \quad (4.9)$$

where  $\overline{i_{Nin}^2}$  is the mean-square input-referred noise current of the photoreceiver, and  $M_{AM}$  is the photocurrent modulation index of the laser amplitude noise. The minimum

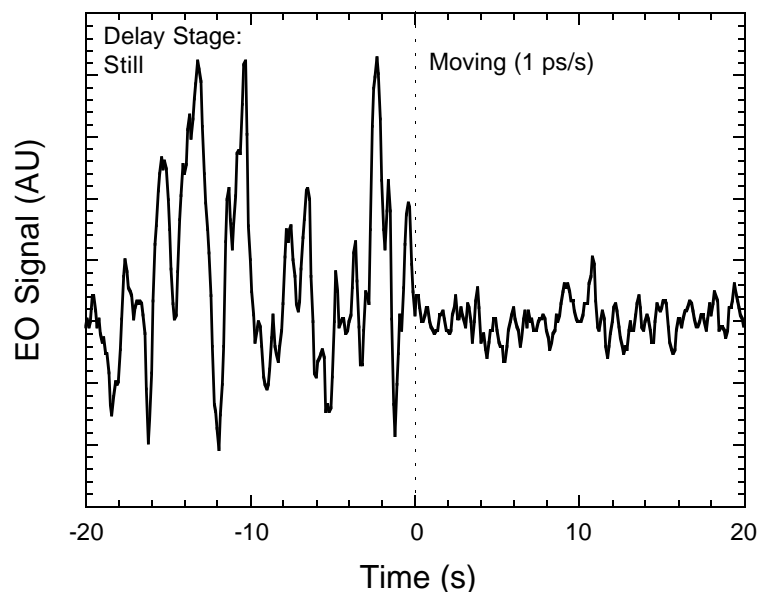


Fig. 4.16 EO sampling measurement of a null signal where the delay stage is kept still for the first half of the trace. About 14 dB excess noise is believed to be due to optical feedback into the Ti:sapphire laser when the stage is still. The moving stage produces a Doppler shift that reduces the feedback instability.

detectable voltage in GaAs at 1 MHz is plotted in Fig. 4.15 from (4.9) as a function of DC photocurrent,  $I_0$ . Directly measured values are also plotted for comparison. The disagreement at higher photocurrents can be accounted for by variations in the laser amplitude noise, which limits  $v_{min}$  at higher photocurrents.

Low frequency amplitude noise can be enhanced by instabilities in the laser resulting from even a very small amount of optical feedback. For this reason, it is often advisable to insert an optical isolator in the beam near the laser output. This was the done in an older Nd:YAG laser based system, but not in the Ti:sapphire laser based system.

Fig. 4.16 shows a null signal measured by the Ti:sapphire laser based system where the delay stage is kept still until the halfway through the trace. When the delay stage is moving at velocity  $v_s/2$ , the changing optical path length results in a Doppler shift of the optical frequency and pulse repetition rate by a factor of  $2v_s/c$  for light reflected back in to the laser. It is likely that the excess noise when the delay stage is

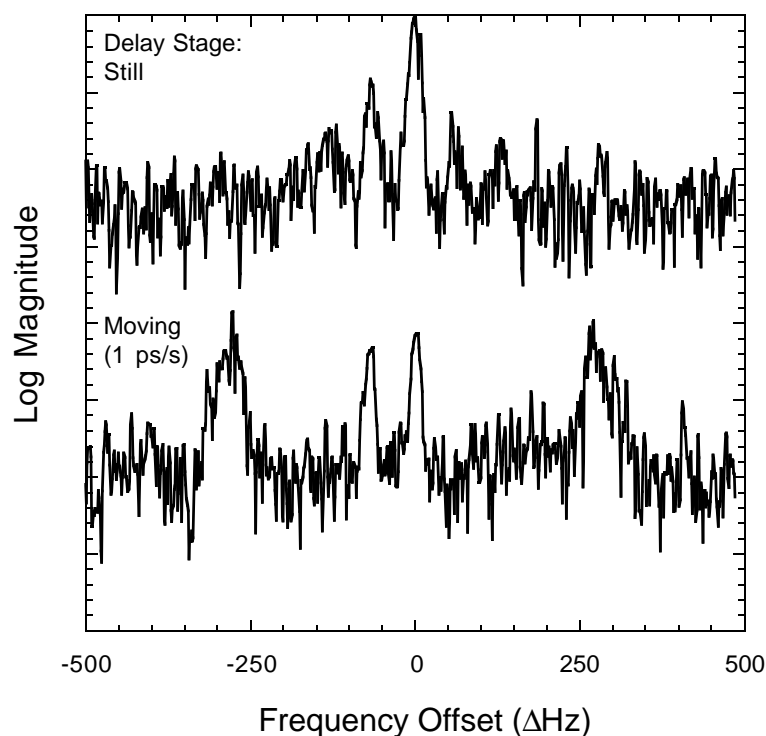


Fig. 4.17 Spectrum of signal at photoreceiver showing Doppler shift of pump beam interference signal while delay stage is moving.

still is due to optical feedback. When the delay stage is moving, the Doppler frequency shift is apparently sufficient to reduce the feedback instabilities.

Pump beam interference, resulting from the mixing of the pump and probe beams at the system photoreceiver, potentially reduces the signal-to-noise ratio of VPD measurements. The pump beam is directly modulated by the AO modulator and thus has three orders of magnitude larger modulation depth than that of the probe beam. Thus, a small amount of pump light can cause a significant interference signal. The pump and probe beams are nearly collinear in VPD measurements and pump light is inevitably scattered into the photoreceiver.

The pump beam interference signal is Doppler shifted by a factor of  $v_s/c$  (the time-scaling factor) when the delay stage is moving at velocity  $v_s/2$ . This is demonstrated in the spectrum plots of Fig. 4.17, where the time-scaling factor of 1

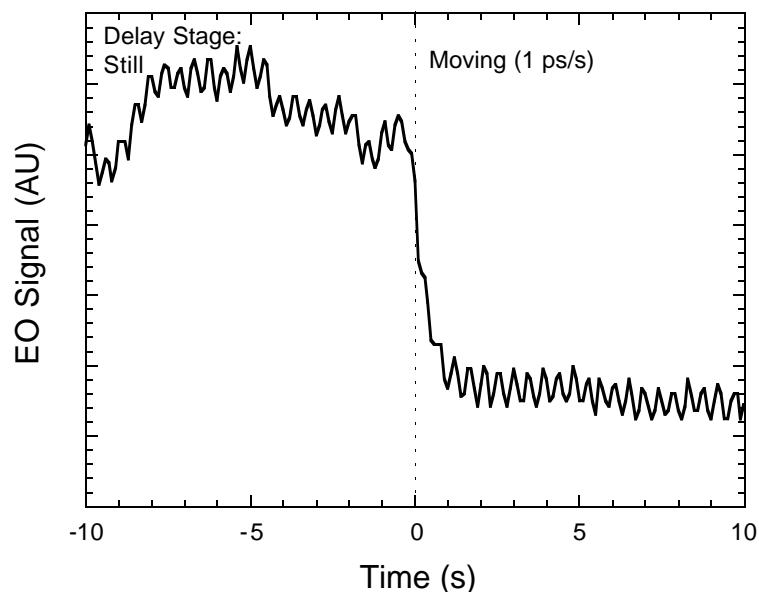


Fig. 4.18 EO sampling measurement of a null signal where the delay stage is kept still for the first half of the trace. System is configured for pump-probe measurements of VPDs. Pump beam interference present when the delay stage is still is Doppler shifted out of the measurement filter band when the stage is moving.

ps/s results in a Doppler shift of 282 Hz at 1064 nm. This frequency shift puts the interference signal well out of the lock-in amplifier bandwidth of about 1 Hz. The EO sampling measured signal in Fig. 4.18 confirms that the interference signal disappears when the stage is moving.

In this chapter, high-speed electro-optic measurement techniques are described. A new electro-optic probe station provides a universal electro-optic measurements platform. After the fundamentals of electro-optic sampling are described, measurement bandwidth limitations are analyzed. It is shown optical transit response is very important for the design of the transmission lines on the DUT. The optical transit response is quantified for CPW and a procedure for dimensional scaling is specified. Deconvolution is a useful tool for photodetector measurements. High sensitivity is needed for measuring the linear response of photodetectors, so the chapter concludes with descriptions of noise and interference affecting photodetector

measurements. The techniques described in this chapter are used for the measurements and analysis presented in the next chapter.

## References

- [1] J. A. Valdmanis and G. Morou, "Subpicosecond Electrooptic Sampling: Principles and Applications," *IEEE J. Quantum Electron.*, vol. 22, no. 1, pp. 69-78, Jan., 1986.
- [2] B. H. Kolner and D. M. Bloom, "Electrooptic Sampling in GaAs Integrated Circuits," *IEEE J. Quantum Electron.*, vol. 22, no. 1, pp. 79-93, Jan., 1986.
- [3] K. J. Weingarten, M. J. W. Rodwell, and D. M. Bloom, "Picosecond Optical Sampling of GaAs Integrated Circuits," *IEEE J. Quantum Electron.*, vol. 24, no. 2, pp. 198-220, Feb., 1988.
- [4] Cascade Microtech, Inc., Beaverton, OR.
- [5] M. Case, M. Kamegawa, K. Giboney, M. Rodwell, J. Franklin, and J. E. Bowers, "62.5 ps to 5.5 ps Soliton Compression on a Monolithic Nonlinear Transmission Line," presented at 48th Annual Device Res. Conf., Santa Barbara, CA, Jun., 1990, VA-2.
- [6] E. Carman, K. Giboney, M. Case, M. Kamegawa, R. Yu, K. Abe, M. J. W. Rodwell, and J. Franklin, "28–39 GHz Distributed Harmonic Generation on a Soliton Nonlinear Transmission Line," *IEEE Microwave Guided Wave Lett.*, vol. 1, no. 2, pp. 28-31, Feb., 1991.
- [7] M. Case, E. Carman, M. Kamegawa, K. Giboney, R. Yu, K. Abe, M. J. W. Rodwell, and J. Franklin, "Impulse Generation and Frequency Multiplication Using Soliton Effects in Monolithic GaAs Circuits," in *OSA Proc. Picosecond Electron. Optoelectron.*, vol. 9, pp. 140-144, 1991.
- [8] E. Carman, M. Case, M. Kamegawa, R. Yu, K. Giboney, and M. J. W. Rodwell, "V-Band and W-Band Broad-Band, Monolithic Distributed Frequency Multipliers," *IEEE Microwave Guided Wave Lett.*, vol. 2, no. 6, pp. 253-254, Jun., 1992.
- [9] K. S. Giboney, S. T. Allen, M. J. W. Rodwell, and J. E. Bowers, "Picosecond Measurements by Free-Running Electro-Optic Sampling," *IEEE Photon. Technol. Lett.*, vol. 6, no. 11, pp. 1353-1355, Nov., 1994.
- [10] Y. G. Wey, D. L. Crawford, K. Giboney, J. E. Bowers, M. J. Rodwell, P. M. Sylvestre, M. J. Hafich, and G. Y. Robinson, "Ultrafast graded double-heterostructure GaInAs/InP photodiode," *Appl. Phys. Lett.*, vol. 58, no. 19, pp. 2156-2158, May 13, 1991.
- [11] Y. G. Wey, K. S. Giboney, J. E. Bowers, M. J. W. Rodwell, P. Silvestre, P. Thiagarajan, and G. Y. Robinson, "108 GHz GaInAs/InP p-i-n Photodiodes with Integrated Bias Tees and Matched Resistors," *IEEE Photon. Technol. Lett.*, vol. 5, no. 11, pp. 1310-1312, Nov., 1993.
- [12] Y. G. Wey, K. Giboney, J. Bowers, M. Rodwell, P. Silvestre, P. Thiagarajan, and G. Robinson, "110 GHz GaInAs/InP Double Heterostructure p-i-n Photodetectors," *J. Lightwave Technol.*, vol. 13, no. 7, pp. 1892-, Jul., 1995.

- [13] M. Kamegawa, K. Giboney, J. Karin, S. Allen, M. Case, R. Yu, M. J. W. Rodwell, and J. E. Bowers, "Picosecond GaAs Monolithic Optoelectronic Sampling Circuit," *IEEE Photon. Technol. Lett.*, vol. 3, no. 6, pp. 567-569, Jun., 1991.
- [14] C. C. Barron, C. J. Mahon, B. J. Thibeault, G. Wang, W. Jiang, L. A. Coldren, and J. E. Bowers, "Resonant-Cavity-Enhanced p-i-n Photodetector with 17 GHz Bandwidth-Efficiency Product," *Electron. Lett.*, vol. 30, no. 21, pp. 1796-1797, Oct. 13, 1994.
- [15] C. C. Barron, C. J. Mahon, B. J. Thibeault, G. Wang, W. Jiang, L. A. Coldren, and J. E. Bowers, "Asymmetric Fabry-Perot Modulators with Millimeter-Wave (37 GHz) Frequency Response," *IEEE Transactions on Electron Devices*, vol.40, no.11, pp. 2146-2147, Nov., 1993.
- [16] K. S. Giboney, R. L. Nagarajan, T. E. Reynolds, S. T. Allen, R. P. Mirin, M. J. W. Rodwell, and J. E. Bowers, "Travelling-Wave Photodetectors with 172 GHz Bandwidth and 76 GHz Bandwidth-Efficiency Product," *IEEE Photon. Technol. Lett.*, vol. 7, no. 4, pp. 412-414, Apr., 1995.
- [17] Model 350150 MLBB-B, Corning, Inc., Corning, NY.
- [18] The 1994 Newport Catalog, Newport Corp., Irvine, CA, p. 3.34.
- [19] R. Y. Yu, M. Reddy, J. Puhl, S. T. Allen, M. Case, and M. J. W. Rodwell, "Millimeter-Wave On-Wafer Waveform and Network Measurements Using Active Probes", *IEEE Trans. Microwave Theory Tech.*, vol. 43, no. 4, pp. 721-729, Apr., 1995.
- [20] M. S. Shakouri, A. Black, B. A. Auld, and D. M. Bloom, "500 GHz GaAs MMIC sampling wafer probe," *Electron. Lett.*, vol. 29, no. 6, pp. 557-558, Mar. 18, 1993.
- [21] M. D. Feuer, S. C. Shunk, P. R. Smith, M. C. Nuss, and H. H. Law, "100 GHz Wafer Probes Based on Photoconductive Sampling," *IEEE Photon. Technol. Lett.*, vol. 5, no. 3, pp. 361-364, Mar., 1993.
- [22] T. Pfeifer, H.-M. Heiliger, E. Stein von Kamienski, H. G. Roskos, and H. Kurz, "Fabrication and characterization of freely positionable silicon-on-sapphire photoconductive probes," *Journal of the Optical Society of America B (Optical Physics)*, vol. 11, no. 12, pp. 2547-2552, Dec., 1994.
- [23] J. Kim, S. Williamson, J. Nees, S. Wakana, and J. Whitaker, "Photoconductive sampling probe with 2.3-ps temporal resolution and 4- $\mu$ V sensitivity," *Appl. Phys. Lett.*, vol. 62, no. 18, pp. 2268-2270, May 3, 1993.
- [24] F. Ho, A. S. Hou, and D. M. Bloom, "High-speed integrated circuit probing using a scanning force microscope sampler," *Electron. Lett.*, vol. 30, no. 7, pp. 560-562, Mar. 31, 1994.
- [25] S. Weiss, D. F. Ogletree, D. Botkin, M. Salmeron, and D. S. Chemla, "Ultrafast scanning probe microscopy," *Appl. Phys. Lett.*, vol. 63, no. 18, pp. 2567-2569, Nov. 1, 1993.
- [26] M. J. W. Rodwell, D. M. Bloom, and K. J. Weingarten, "Subpicosecond Laser Timing Stabilization," *IEEE J. Quantum Electron.*, vol. 25, no. 4, pp. 817-827, Apr., 1989.

- [27] D. J. Derickson, P. A. Morton, J. E. Bowers, and R. L. Thornton, "Comparison of timing jitter in external and monolithic cavity mode-locked semiconductor lasers," *Appl. Phys. Lett.*, vol. 59, no. 26, pp. 3372-3374, Dec. 23, 1991.
- [28] A. Yariv and P. Yeh, *Optical Waves in Crystals: Propagation and Control of Laser Radiation*. New York: John Wiley & Sons, 1984, Ch. 7-8.
- [29] V. Swaminathan and A. T. Macrander, *Materials Aspects of GaAs and InP Based Structures*. Englewood Cliffs: Prentice Hall, 1991, p. 326.
- [30] S. Adachi, "Linear Electro-Optic Effects in AlGaAs," in *Properties of Aluminium Gallium Arsenide*, S. Adachi, Ed. London: INSPEC, 1993, pp. 151-154.
- [31] T. Shibata, T. Nagatsuma, and E. Sano, "Effective optical transit time in direct electro-optic sampling of GaAs coplanar integrated circuits," *Electron. Lett.*, vol. 25, no. 12, pp. 771-773, Jun. 8, 1989.
- [32] R. L. Fork and F. A. Beisser, "Real-time intensity autocorrelation interferometer," *Applied Optics*, vol. 17, no. 22, pp. 3534-3535, Nov. 15, 1978.
- [33] J. D. Kafka, J. W. Pieterse, and M. L. Watts, "Two-color subpicosecond optical sampling technique," *Opt. Lett.*, vol. 17, no. 18, pp. 1286-1288, Sep. 15, 1992.
- [34] R. Takahashi and T. Kamiya, "Noise suppression by a novel probe beam polarization modulation in electro-optic sampling," *Appl. Phys. Lett.*, vol. 58, no. 20, pp. 2200-2202, May 20, 1991.
- [35] P. C. D. Hobbs, "Reaching the Shot Noise Limit for \$10," *Opt. Photon. News*, pp. 17- 23, Apr., 1991.
- [36] Model NJA-3, Clark Instrumentation, Rochester, NY.
- [37] Model EFL-M080A06, Matsushita Corp., Japan.



## CHAPTER 5

# MEASUREMENTS & ANALYSIS

Theory, design, and fabrication culminate in measurements. Ideally, measurements identify successes and failings of each step in the development. More practically, the evaluation of certain performance attributes are the goals. The goals for the following presentation are to establish that the travelling-wave photodetector (TWPD) is a distinctly new device with identifiable characteristics, and to demonstrate that the TWPD has performance advantages over conventional photodetectors.

The TWPDs are distinguished by comparing their performance to that of lumped-element devices, waveguide photodetectors (WGPDs), and vertically illuminated photodetectors (VPDs) fabricated on the same wafer. Higher bandwidths and larger bandwidth efficiency products, along with the relative length independence of the TWPDs is evidence in direct support of the theory of distributed photodetection. TWPDs can also be differentiated from lumped-element devices using propagation constants derived from the electro-optic (EO) sampling measurements.

Accuracy is improved by correcting for distortion introduced by the measurement system. The EO sampling system response is deconvolved using the methods described in Sections 4.3 and 4.4. Similar techniques can be used to eliminate electrical reflections under certain circumstances. Reflection deconvolution proves useful in the analysis of the longer responses in the last section on field-screening effects.

### 5.1 Travelling-Wave Photodetector Performance

Materials growth and device processing resulted in close to design values for most properties. Typical capacitance and derived depletion depth versus reverse bias are plotted in Fig. 5.1. Evidently, the i-layer and p- and n-graded layers are very close to their design thicknesses and doping profiles. Mean n and p layer surface

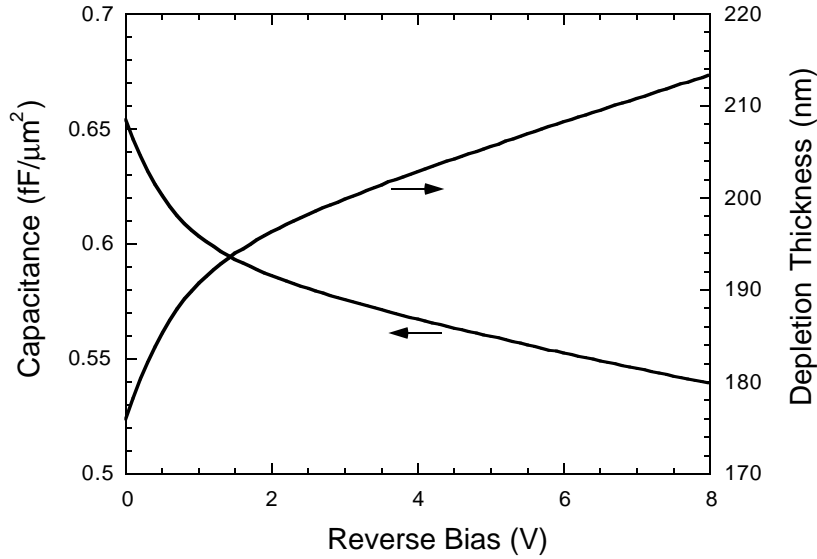


Fig. 5.1 Typical capacitance-voltage characteristics from measurements on  $100\ \mu\text{m} \times 100\ \mu\text{m}$  p-i-n diodes. The depletion layer thickness is calculated from the capacitance.

resistances across a quarter of a two inch wafer are 111 and  $147\ \Omega/\text{square}$ , corresponding to bulk resistivities of 73 and  $89\ \Omega\cdot\mu\text{m}$ . The n and p specific contact resistances are 46 and  $660\ \Omega\cdot\mu\text{m}^2$ . Isolation surface resistance is  $2.2\ \text{G}\Omega/\text{square}$ .

The averages of several large area ( $100\ \mu\text{m} \times 100\ \mu\text{m}$ ) diode DC characteristics were good. They have an ideality factor of 1.77, which is reasonable for p-i-n diodes, and current intercept of 44 fA ( $4.4\ \text{aA}/\mu\text{m}^2$ ). Reverse current is  $4.4\ \mu\text{A}$  ( $440\ \text{pA}/\mu\text{m}^2$ ) at 5 V, and reverse breakdown was abrupt at just under 10 V.

Very long TWPD ( $1\ \mu\text{m}$  wide) structures showed worse DC characteristics due to the larger periphery to area ratio. A  $340\ \mu\text{m}$  long TWPD structure has an ideality factor of 1.93 with current intercept of 291 fA ( $860\ \text{aA}/\mu\text{m}$ ). Leakage current is  $1.0\ \mu\text{A}$  ( $3.0\ \text{nA}/\mu\text{m}$ ) at 1 V and  $4.4\ \mu\text{A}$  ( $13\ \text{nA}/\mu\text{m}$ ) at 5 V reverse bias. The currents were the same for two and five micron wide devices of the same length, indicating that they are dominated by surface effects. Reverse breakdown is only slightly degraded compared to the large area devices.

External quantum efficiency, expressed in (1.3), is completely characterized by two parameters: the net coupling efficiency,  $\eta_c(1 - R)$ , and the modal absorption

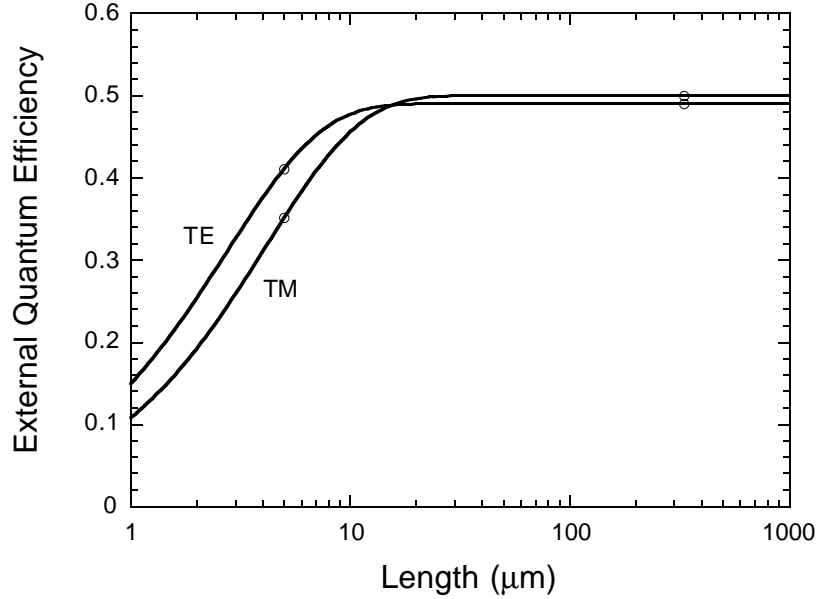
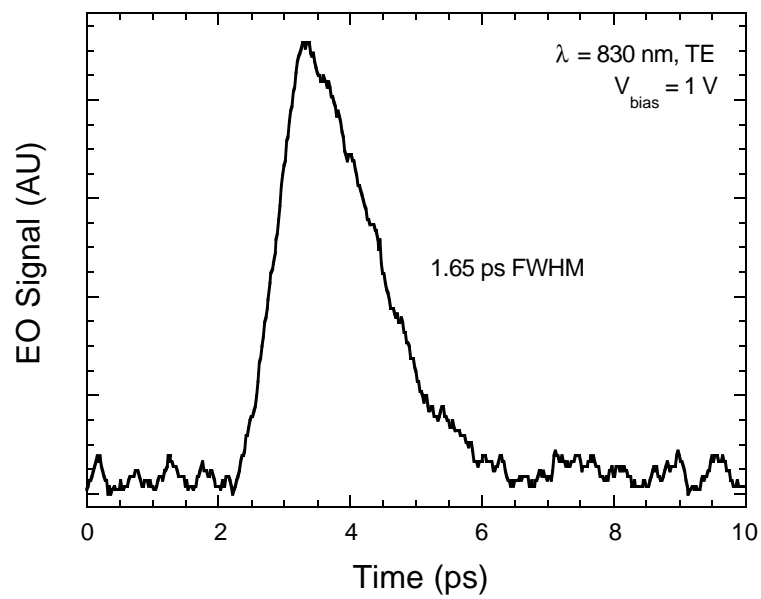


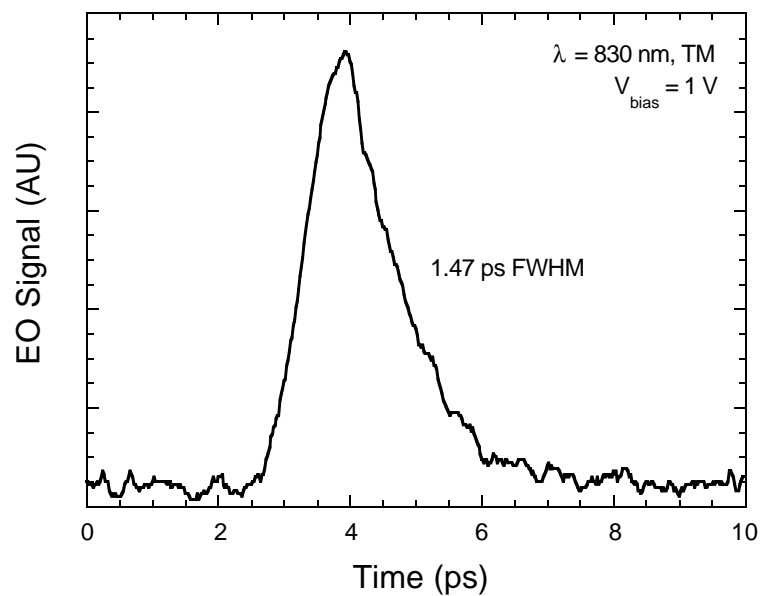
Fig. 5.2 External quantum efficiency of TWPDs versus length from measurements of 5  $\mu\text{m}$  and 340  $\mu\text{m}$  long devices.

coefficient,  $\Gamma\alpha$ . Since the Fresnel reflectivity is less than 0.01,  $R < 0.01$ , the net coupling efficiency is approximately equal to the modal coupling efficiency,  $\eta_c(1 - R) \approx \eta_c$ . The net coupling efficiency is the external quantum efficiency of a very long ( $\Gamma\alpha l \gg 1$ ) device. The modal absorption coefficient is found from an intermediate length device.

The external responsivities of 5  $\mu\text{m}$  and 340  $\mu\text{m}$  long TWPD and WGPD structures are measured at DC using a molded aspheric coupling lens [1]. The external quantum efficiencies are reconstructed from the measurements in Fig. 5.2 for TE and TM mode illumination of TWPDs. The coupling efficiencies of the TWPDs are 0.49 and 0.50 for TE and TM modes. The 2  $\mu\text{m}$  wide WGPDs yield slightly higher coupling efficiencies of 0.52 and 0.54. The coupling efficiency is lower for TE modes because they evidently have a smaller overlap with the free-space mode. The tighter confinement of the TE modes also results in a higher modal absorption coefficient, evident in Fig. 5.2.



(a)



(b)

Fig. 5.3 Pulse response of a 7  $\mu\text{m}$  long TWPD with 1 V bias and (a) TE and (b) TM illumination at 830 nm wavelength.

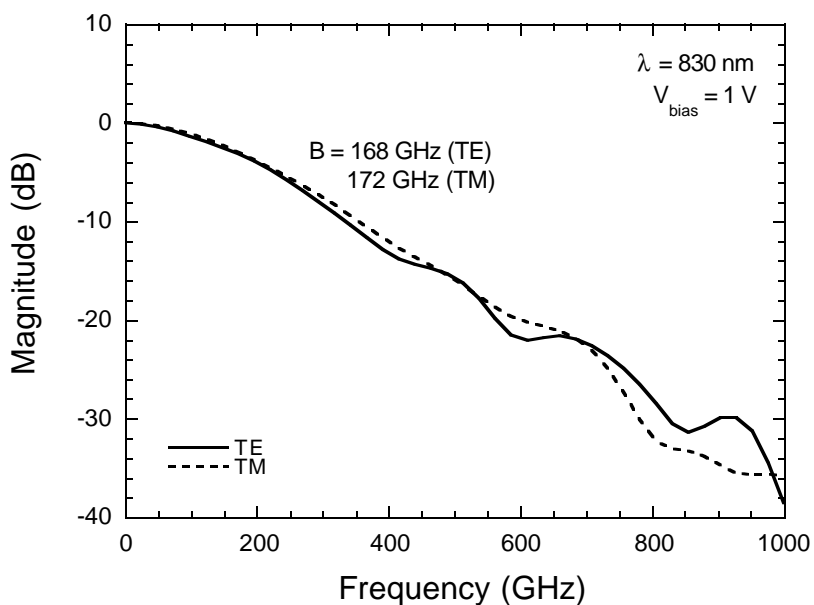


Fig. 5.4 Electrical frequency responses of a 7  $\mu\text{m}$  long TWPD for TE and TM illumination from the Fourier transforms of the pulse responses in Figs. 5.3 and 5.4.

The modulation responses of the TWPDs, WGDs, and VPDs are measured by pump-probe EO sampling, described in Chapter 4 on electro-optic measurement techniques. The laser source is a passively mode-locked Ti:sapphire laser producing pulses of less than 150 fs full-width at half-maximum (FWHM) at a repetition rate of 100 MHz. The EO sampling system sensitivity is measured to be 60-70  $\mu\text{V}/\sqrt{\text{Hz}}$  at 0.8-0.9 mA on the substrate-removed TWPD samples. Typical currents in the EO system photoreceiver during photodiode measurements are 0.3-0.7 mA.

Measured pulse responses of a 7  $\mu\text{m}$  long TWPD under 1 V reverse bias with TE and TM mode illumination at 830 nm wavelength are plotted in Fig. 5.3. The DC level of the measured signals is independent of pump amplitude. The TE and TM response FWHM are 1.65 ps and 1.47 ps. Differences in pulse shape between the two responses on this scale are not considered significant due to fluctuations in the measurement system.

The frequency responses plotted in Fig. 5.4 are found from the Fourier transforms of the pulse responses in Fig. 5.3. The difference between the two is within measurement error. The bandwidths are 168 GHz and 172 GHz for the TE

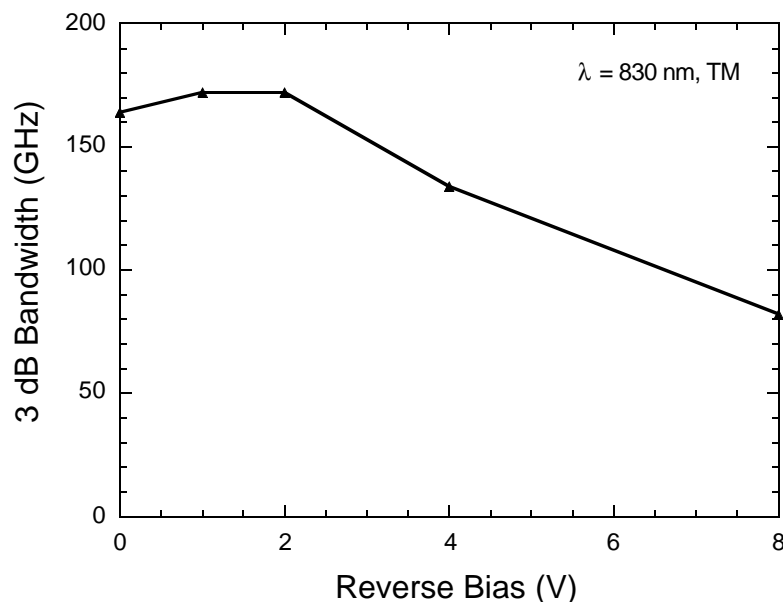


Fig. 5.5 Electrical bandwidth of a 7  $\mu\text{m}$  long TWPD versus bias voltage.

and TM cases, yielding bandwidth-efficiency products of 76 GHz and 72 GHz. Note that the external quantum efficiency is greater than 10% at 400 GHz and larger than 1% at 800 GHz.

A  $2 \times 9 \mu\text{m}^2$  WGPD has a bandwidth of 118 GHz with external quantum efficiency of 49%, giving a bandwidth-efficiency product of 57 GHz. These are the highest bandwidth and bandwidth-efficiency product reported for a WGPD, but the TWPD bandwidth-efficiency product is still 1/3 greater. A  $3 \times 3 \mu\text{m}^2$  VPD has a bandwidth of about 170 GHz, but its internal quantum efficiency is limited to about 30%.

The TWPD bandwidth versus reverse bias is plotted in Fig. 5.5. There is a maximum at around 1-2 V reverse bias. At zero bias, the carrier transit region is not fully depleted, as is evident from the high initial slope of the depletion thickness in Fig. 5.1. At 8 V reverse bias, the electric field in the depletion region is near the breakdown value for GaAs [2], and the device response is unstable. Apparently, avalanche multiplication is significant above 2 V and causes the decrease in

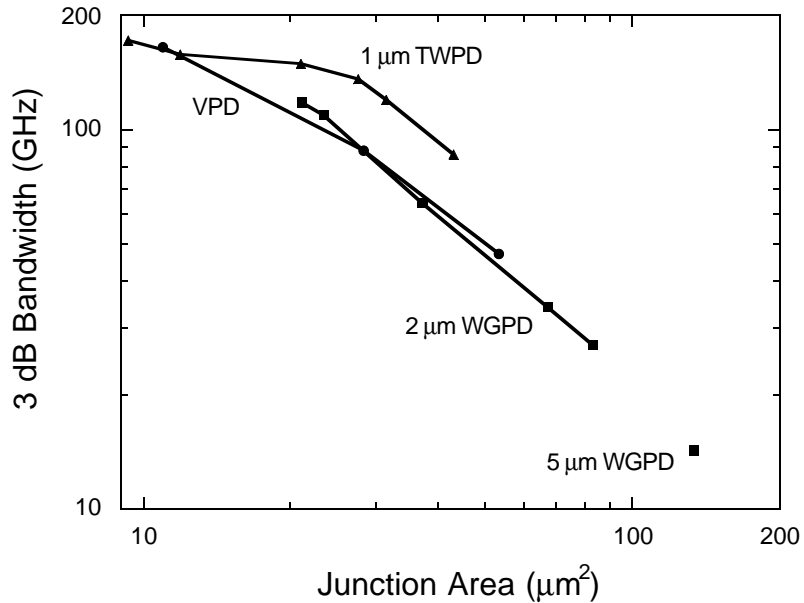


Fig. 5.6 Electrical bandwidths versus junction area of travelling-wave, waveguide, and vertically illuminated photodetectors fabricated on the same wafer.

bandwidth from 2 to 8 V reverse bias. Avalanche multiplication at high bias voltages also explains a 20-25% increase in quantum efficiency from 1 V to 8 V reverse bias.

To show that the TWPD bandwidth is not bounded by an RC limitation determined by the total junction area, the bandwidths of various lengths of TWPDs and WGPDs and various sizes of VPDs are plotted versus junction area in Fig. 5.6. All of the device bandwidths approach the transit-time bandwidth limitation as the area becomes small. The bandwidths are inversely proportional to area for larger (or longer) devices, but the bandwidths of the TWPDs are 50% larger than those of the WGPDs or VPDs. This demonstrates that the TWPDs are not subject to the same RC bandwidth limitation as the lumped devices, and strongly implies that the TWPDs are instead subject to a velocity mismatch bandwidth limitation.

## 5.2 Propagation Constant

Microwave loss on the metal-clad p-i-n waveguide structure causes a decrease in bandwidth with increasing TWPD length. The velocity-mismatch and carrier transit bandwidth limitations affect TWPD response only where there is light absorption.

After the light is mostly absorbed, the response is dominated by the electrical wave propagation characteristics.

Measuring the complex propagation constant on a photodiode transmission line structure using a conventional network analyzer provides information only over a small fraction of the bandwidth of interest. Due to an unfortunate error in layout, such a test structure is not available, anyway. However, an alternative method derives from the fact that the photocurrent responses of long TWPDs differ only by the effects of propagation over the differences in their lengths.

The complex microwave propagation constant can be determined by deconvolving the responses of long TWPDs measured by EO sampling. This method is equivalent to finding the propagation constant from network analyzer measurements of different lengths of transmission line, and it is capable of much greater bandwidth than is possible with a commercial network analyzer. Unfortunately, a precision time reference was not established with each measurement, so an absolute phase reference is not available.

The transfer function, characterizing propagation from one reference plane to another in a transmission line is defined as

$$T_{12} \equiv \frac{V(z_2)}{V(z_1)} = e^{-\gamma(z_2-z_1)} = e^{-\alpha_e(z_2-z_1)} \cdot e^{-j\beta(z_2-z_1)}. \quad (5.1)$$

The complex propagation constant, defined in (2.8) is found from measurements of two devices of different lengths according to

$$\alpha_e = \frac{\ln|T_{12}|}{\ell_1 - \ell_2} \quad (5.2)$$

$$\beta = \frac{\arg(T_{12})}{\ell_1 - \ell_2}. \quad (5.3)$$

As noted, the phase constant,  $\beta$ , can be determined only to within an arbitrary factor from the EO sampling measurements.

Experimental data from 16  $\mu\text{m}$  through 33  $\mu\text{m}$  long TWPDs are used to determine the complex propagation constant. These devices are at least four absorption lengths

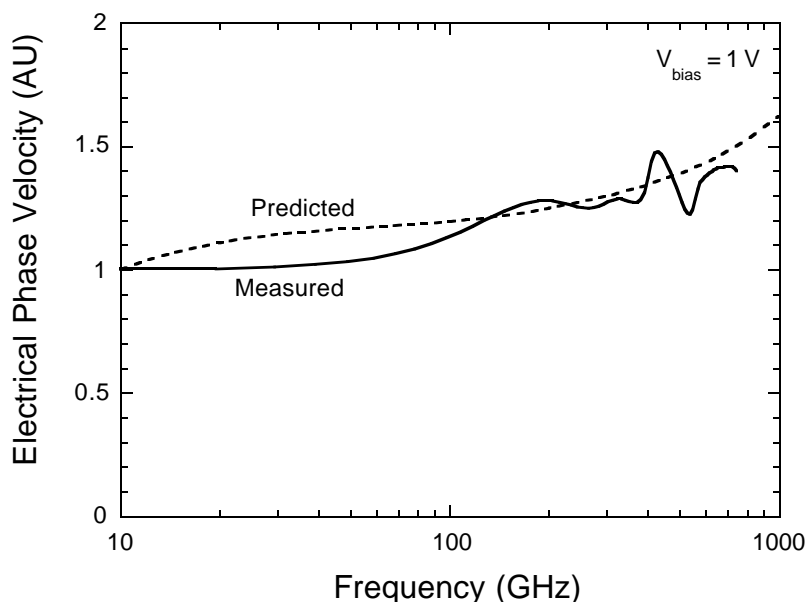


Fig. 5.7 Electrical phase velocity, normalized to 1 at 10 GHz, derived from EO sampling measurements of 21  $\mu\text{m}$  and 33  $\mu\text{m}$  long TWPDs. The predicted curve, normalized from Fig. 3.8 is shown for comparison.

long, so more than 98% of the light is absorbed in all of them. The phase velocity, normalized to one at 10 GHz, is plotted in Fig. 5.7. Values above a couple hundred gigahertz are of questionable reliability. The plot shows an increase in velocity similar to that predicted in the model, Fig. 3.8, but appears to be displaced to a much lower frequency.

Fig. 5.8 shows two sets of TWPD field attenuation constants, deconvolved from pulse response measurements of four different lengths of TWPDs. The attenuation is proportional to  $f^2$  for frequencies below about 75 GHz and seems to level out above that frequency. The behavior does not agree well with that predicted in Fig. 3.9. The strong frequency-squared dependence suggests a large  $RC + GL$  term in (2.12). The two traces differ little because the devices are transmission lines and wave propagation is length independent.

The differences between the predicted and measured propagation characteristics may be explained by examining the differences between the physical device and the model. Probably the most significant effect comes from annealed ohmic contacts that

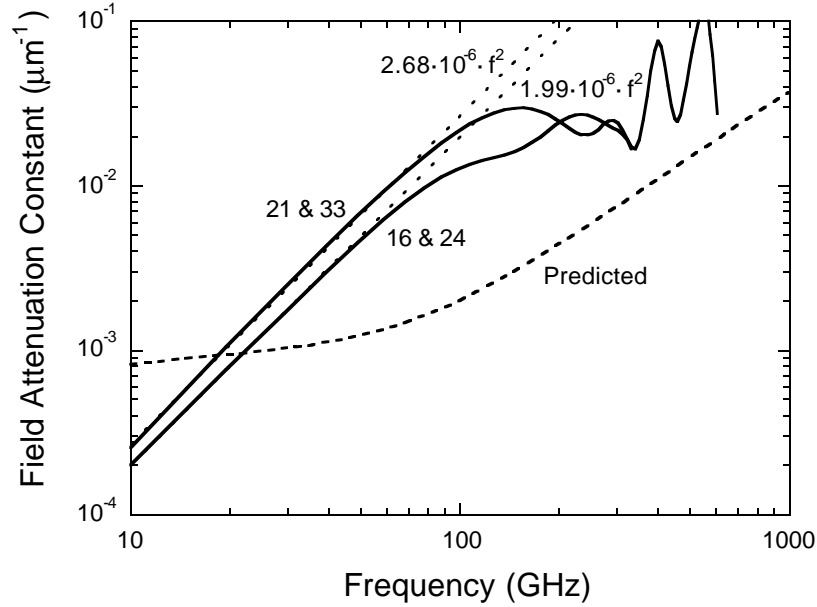


Fig. 5.8 Field attenuation constant, derived from EO sampling measurements of 16  $\mu\text{m}$  and 24  $\mu\text{m}$ , and 21  $\mu\text{m}$  and 33  $\mu\text{m}$  long TWPDs. The predicted curve from Fig. 3.9 is shown for comparison.

are rough and "spike" into the semiconductor cladding layers. Exact analysis is extremely difficult, however the roughness likely increases the transmission line inductance, and alloying affects the properties of the cladding layer material. From the theory presented in Section 2.2, an increase in inductance would enhance slow-wave effects and cause propagation characteristics to shift in frequency. Reflections and radiation at the interface between the TWPD and the connecting CPW transmission line may also account for some difference between the predicted and measured propagation characteristics.

By applying (5.1) to WGDs, a "mock propagation constant" for lumped element structures can be derived and compared to that for true wave propagation. This yields a method for distinguishing between TWPDs and WGDs by their response measurements. Using a simple RC model, as in Fig. 1.1, and (5.1) gives a mock transfer function

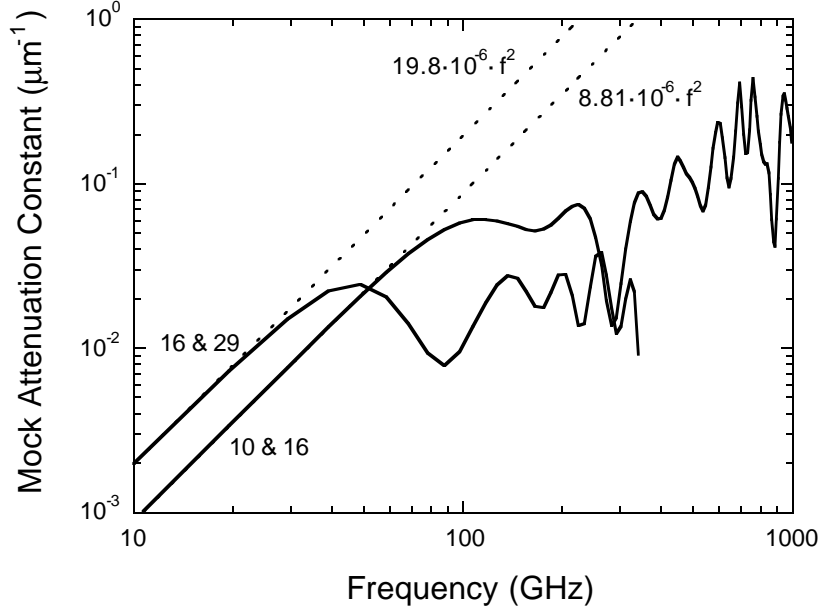


Fig. 5.9 WGPD mock attenuation constant, from EO sampling measurements of 10  $\mu\text{m}$  and 16  $\mu\text{m}$ , and 16  $\mu\text{m}$  and 29  $\mu\text{m}$  long, 2  $\mu\text{m}$  wide WGPDs.

$$T_{12}' \equiv \frac{V(l_2)}{V(l_1)} = \frac{1 + j\omega RC l_1}{1 + j\omega RC l_2} \quad (5.4)$$

where  $C$  is the capacitance per unit length. At low frequencies,  $\omega RC l_1 \ll 1$  and  $\omega RC l_2 \ll 1$ , the mock attenuation and phase constants of a WGPD are approximated by

$$\alpha_e' \approx \frac{(\omega RC)^2}{2} (l_1 + l_2) \quad (5.5)$$

$$\beta' \approx \omega RC. \quad (5.6)$$

The mock phase constant,  $\beta'$ , is linear in frequency and length independent, just like the true phase constant for dispersionless wave propagation, so WGPDs are not readily distinguished from TWPDs by comparing phase constants.

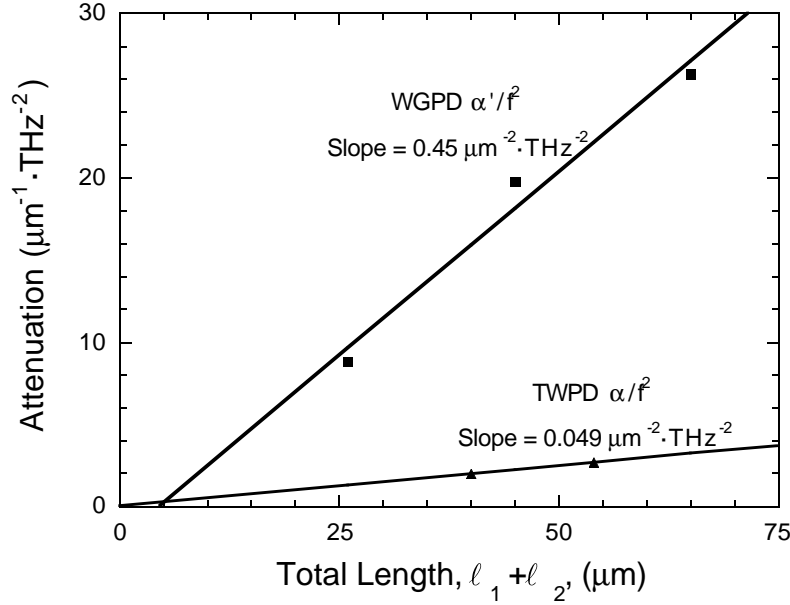


Fig. 5.10 Low-frequency attenuation of TWPDs and WGPDs versus total length of devices used to find the attenuation.

The mock attenuation constant of a WGP,  $\alpha_e'$ , has the same frequency squared dependence as does the attenuation constant of a TWPD. However  $\alpha_e'$  is proportional to the total length of the two WGP, while  $\alpha_e$ , for TWPDs, is length independent. This implies a method for discriminating between TWPDs and WGP by their response measurements. A linear dependence will be apparent in a plot of low-frequency attenuation,  $\alpha_e'/f^2$  for WGP, versus total length,  $\ell_1 + \ell_2$ , while a plot of  $\alpha_e/f^2$  for TWPDs will ideally show a zero slope.

Fig. 5.9 shows WGP mock attenuation constants versus frequency, deconvolved from pulse response measurements. The mock attenuation is proportional to  $f^2$  for low frequencies, and the frequency at which it rolls over appears to be length dependent. Note that the mock attenuation appears to be length dependent and is nearly an order of magnitude larger than attenuation in comparable length TWPDs, plotted in Fig. 5.8.

The plot of  $\alpha_e/f^2$  and  $\alpha_e'/f^2$  versus  $\ell_1 + \ell_2$  in Fig. 5.10 shows that the TWPD attenuation has a much smaller slope than the WGP mock attenuation, although it is not zero. The residual slope is probably a result of a confluence of factors that make

these TWPDs less than ideal. There is a small reflection coefficient at the TWPD output according to the design in Section 3.3. As mentioned earlier, some characteristics of the physical structure are not included in the model. Also, a mismatch of electrical wave modes at the junction between the TWPD and the coplanar waveguide (CPW) may lead to a significant reflection.

The mock attenuation constant is proportional to the square of the device width, according to (5.5). Using the WGP slope as a reference, the slope for the TWPD is less than half of the slope of a lumped element device of the equal width. This is further evidence that the TWPDs are appropriately modelled as transmission lines rather than lumped element devices.

### 5.3 Electro-Optic Sampling System Response Correction

The EO sampling system response is analyzed to assess its impact on the measured results. As discussed in Sections 4.3 and 4.4, the primary components of the EO sampling system response are the optical pump and probe pulse profiles, and the optical transit response.

Autocorrelation measurements of the in-plane pump and probe pulses in Fig. 5.11 show that the pump pulse broadens by a factor of six as it passes through the optical fiber. This is consistent with the 0.64 m fiber length and the manufacturer's specification for linear dispersion in the single-mode fiber of 120 fs/nm/m at 820nm wavelength [3].

A finite-element method computer program is used to calculate the potential profile and normal component electric field in the AlGaAs substrate and glass under the CPW [4, 5]. The four micron thick substrate limits the optical transit impulse response to less than 100 fs as shown in Fig. 5.12.

Fig. 5.13 shows components of the EO sampling system frequency response for pump-probe photodetector measurements. The net measurement bandwidth for in-plane pump is 450 GHz. The net measurement bandwidth for vertical pump is four times as large because the pump pulse does not pass through the optical fiber.

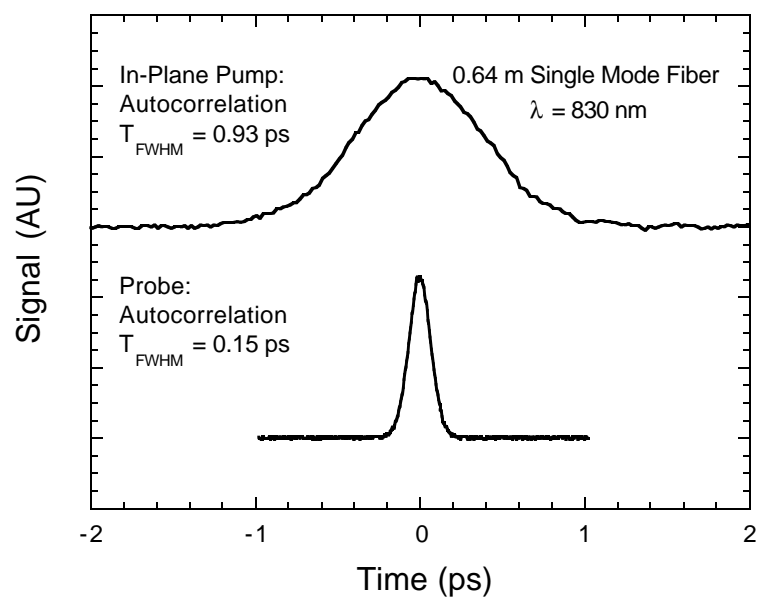


Fig. 5.11 Autocorrelation measurements of pump and probe pulses. Pump pulse for in-plane illumination passes through an optical fiber.

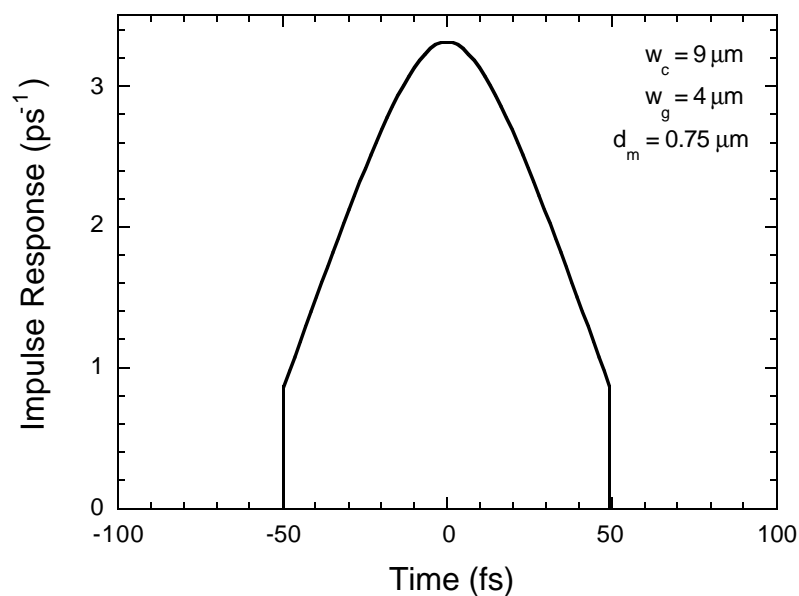


Fig. 5.12 Optical transit impulse response for the CPW on  $4.5 \mu\text{m Al}_{0.5}\text{Ga}_{0.5}\text{As}$  that is connected to the photodetectors.

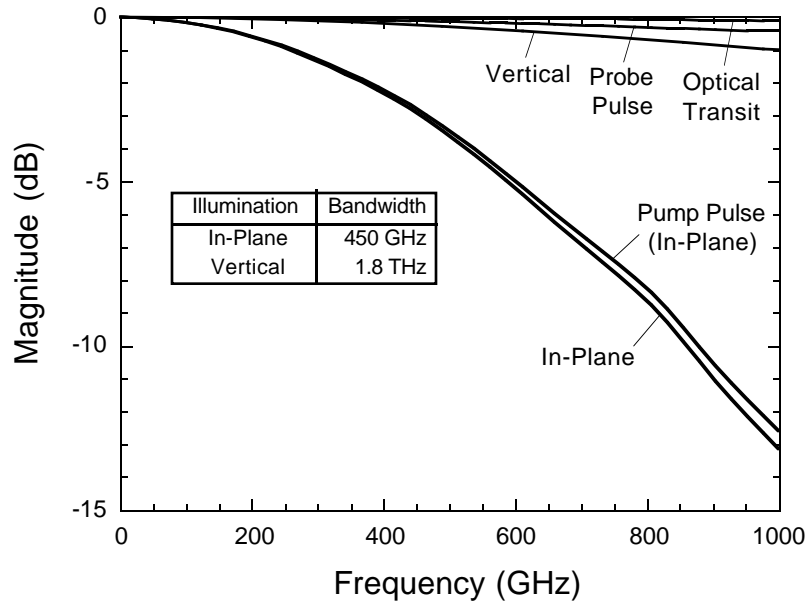
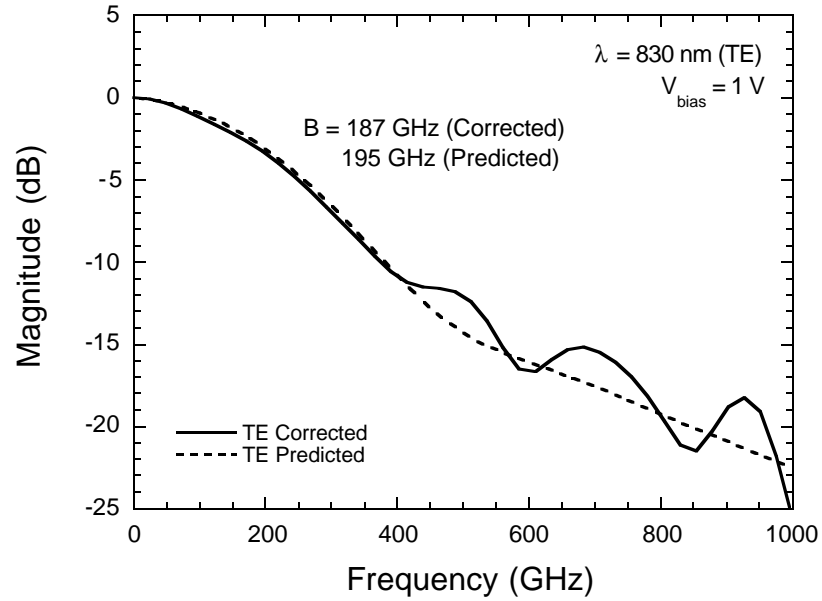
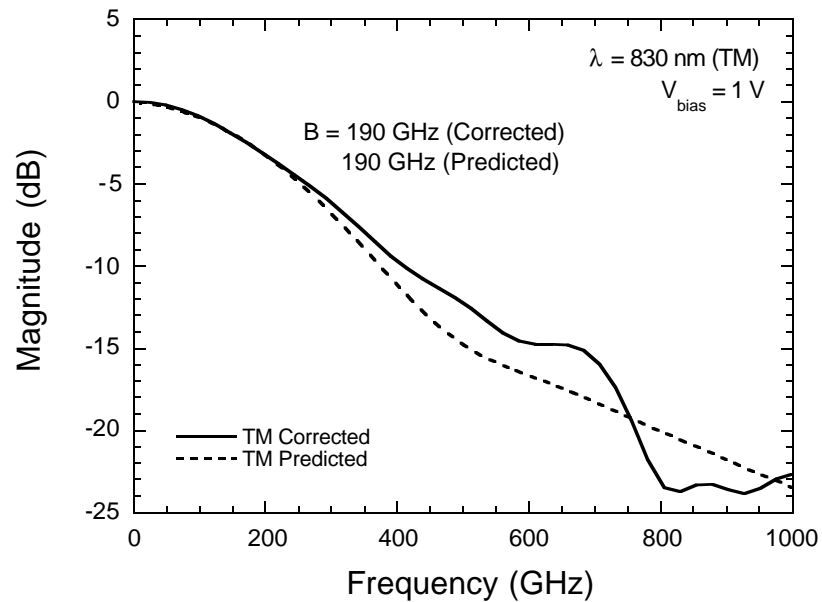


Fig. 5.13 Pump-probe EO sampling system frequency response for in-plane illumination through an optical fiber and free-space vertical illumination. Individual components and net responses are plotted.

The EO sampling system frequency response is used to correct measurement error in the device frequency responses according to (4.8). The time waveform cannot be recovered since it requires the cross-correlation of the pump and probe pulses, which was not measured. The frequency responses of Fig. 5.4 are deconvolved and plotted in Fig. 5.14. Also plotted are predictions of the frequency responses using DC measured parameters, presented in Section 5.1, in the effective area approximation (Section 2.4). The differences between the corrected measured and the predicted responses at high frequencies is explained by error in the effective area approximation and in the assumed electron velocity. The corrected measured bandwidths of 187 GHz and 190 GHz for TE and TM illumination are very close to the predicted bandwidths. These numbers give revised bandwidth-efficiency products of 84 GHz and 80 GHz.



(a)



(b)

Fig. 5.14 Electrical frequency responses of a 7 μm long TWPD for (a) TE and (b) TM illumination, corrected for EO sampling system response. The predicted frequency responses (broken lines) are found using DC measured parameters in the effective area approximation.

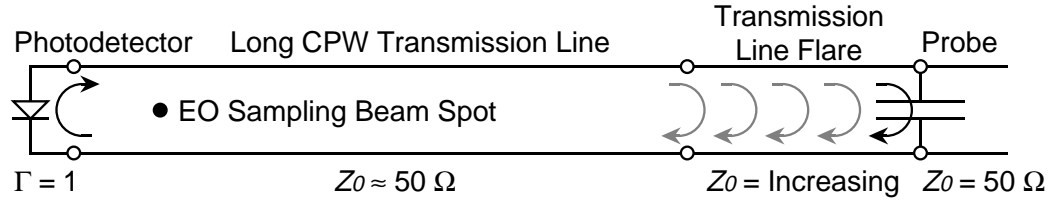


Fig. 5.15 Schematic diagram of measurement circuit for EO sampling with impedance variations.

#### 5.4 Reflection Deconvolution

Fig. 5.15 shows a schematic diagram of the measurement circuit with identifiable characteristic impedances labelled. The reflection coefficient at the TWPD input end is one. The characteristic impedances of the TWPD and long CPW transmission line are about  $50\ \Omega$  (actually closer to  $40\ \Omega$ ). The transmission line flare and pads are designed to maintain a constant characteristic impedance when on a thick substrate, but the impedance increases with the lateral dimensions of the CPW after the substrate is removed. The characteristic impedance of the probe pads is then about  $70\ \Omega$ . There is a parasitic capacitance at the microwave probe tip and the characteristic impedance in the probe is  $50\ \Omega$ . As mentioned in Section 3.3, the  $800\ \mu\text{m}$  line is expected to provide a  $10\ \text{ps}$  reflection-free measurement window when the EO sampling beam is  $100\ \mu\text{m}$  from the photodetector output.

The long CPW transmission lines connecting to the TWPDs effectively delay electrical reflections out of the measurement window for the fast photodetector responses, but the lines are not long enough to prevent reflection interference with the slow responses. When the photodetector response overlaps the reflections, time-windowing of the response is not possible, and including the reflections in the calculation of the frequency response produces erroneous results.

It is possible to derive more accurate responses by deconvolving the reflections. The reflection impulse response is found from fast photodetector measurements. Fig. 5.16 shows a fast TWPD measured response divided into regions of pulse and reflections,  $s_0(t) = a_0(t) + b_0(t)$ . The reflections are the convolution of the pulse with the reflection impulse response, or

$$b_0(t) = a_0(t) * R(t). \quad (5.7)$$

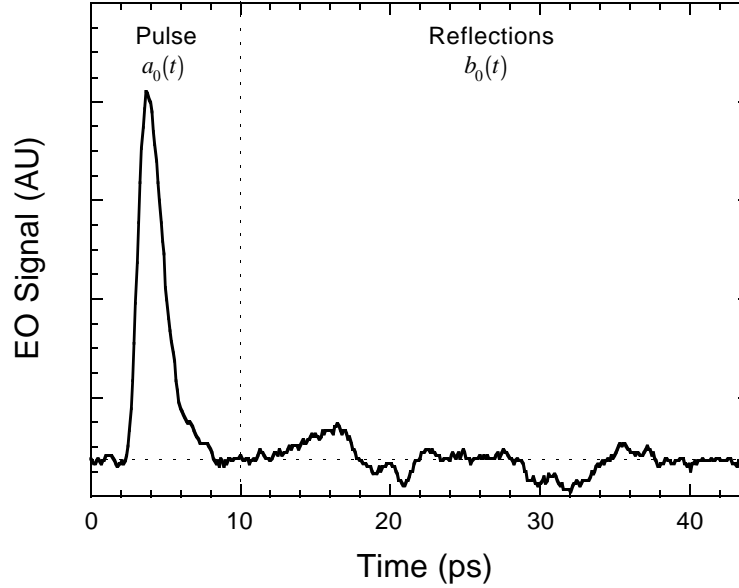


Fig. 5.16 Typical EO sampling measured response of a TWPD showing reflections from measurement circuit impedance variations.

$R$  is found by dividing in the frequency domain,

$$R(f) = \frac{b_0(f)}{a_0(f)}. \quad (5.8)$$

Fig. 5.17 shows the reflection impulse response for the trace in Fig. 5.16. There is some noncausal ringing in Fig. 5.17 as a result of a necessary linear filter, but the delay before the first reflection appears to be about 7-9 ps. The velocity in CPW may be greater than predicted due to the unknown thickness of the sublayer, a possible air gap between the sublayer and the glass substrate, and high lips on the interconnect metal resulting from the lift-off process (see Fig. 3.15).

The first rising response in Fig. 5.17 is consistent with the increasing impedance of the flared transmission line section. The large negative reflection with a positive-going peak in the middle comes from the capacitive discontinuity at the probe tip and the lower probe impedance. The positive-going peak is probably due to the secondary reflection of the first positive peak from the photodiode end. Interference from

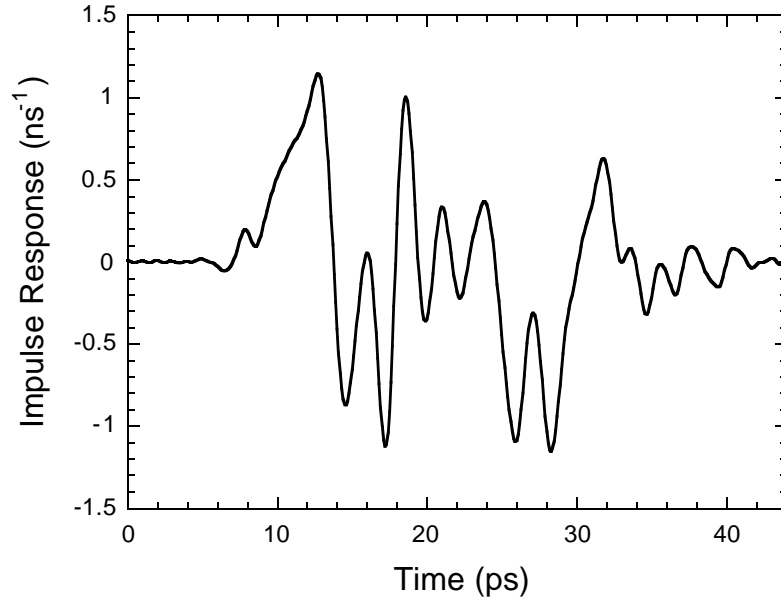


Fig. 5.17 Electrical reflection impulse response derived from the trace in Fig. 5.16.

secondary reflections at the photodiode complicate interpretation of subsequent features.

Reflections can be deconvolved from any signal with reflection impulse response,  $R$ , by

$$a(f) = \frac{s(f)}{1 + R(f)}. \quad (5.9)$$

Fig. 5.18 shows the result of deconvolving reflections from a TWPD slow response using the reflection impulse response in Fig. 5.17. Reflections in the signal as measured could easily be confused for a tail on the photodetector response. Reflection deconvolution removes this uncertainty.

### 5.5 Field-Screening Effects

Pulse response measurements are a convenient tool for investigating field-screening effects. The charge is photogenerated in a time much shorter than the device

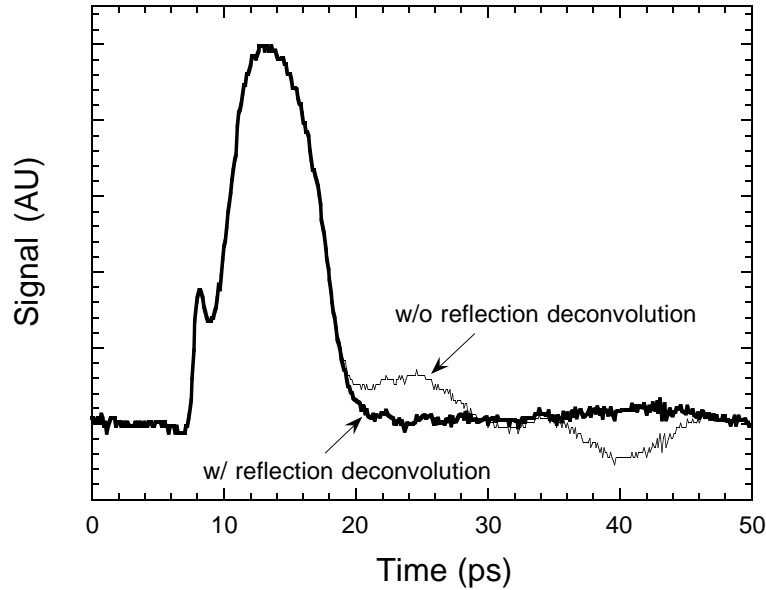


Fig. 5.18 Example of a slow TWPD response showing the signal as measured, without reflection deconvolution, and the response after deconvolving reflections using the reflection impulse response in Fig. 5.17.

response time and a duty cycle of about 1/1000 reduces thermal effects. Detailed features of device responses are resolved with pump-probe EO sampling.

Figs. 5.19 and 5.20 show pulse responses of a  $3 \times 3 \mu\text{m}^2$  VPD and a  $7 \mu\text{m}$  long TWPD at 1 V reverse bias with photogenerated charge from below to far above the field-screening thresholds. The two lowest traces in the plots, at about 4 and 10 fC of photogenerated charge, show no effects of field screening. The next traces up, at around 25 fC, are broader and display a low-level "tail."

At higher photogenerated charge of 50-60 fC, the responses show a shape that occurs when a significant fraction of the total photogenerated charge is affected by field screening [6]. The initial current transients are due to high carrier velocities prior to drift field collapse. The TWPD transient is relatively larger because it also includes a fast current component from the unscreened region as described in Section 2.5. As the photogenerated charge is increased further, the initial transient becomes smaller because the field screening occurs earlier and a decreasing fraction of the total charge is swept out under high field.

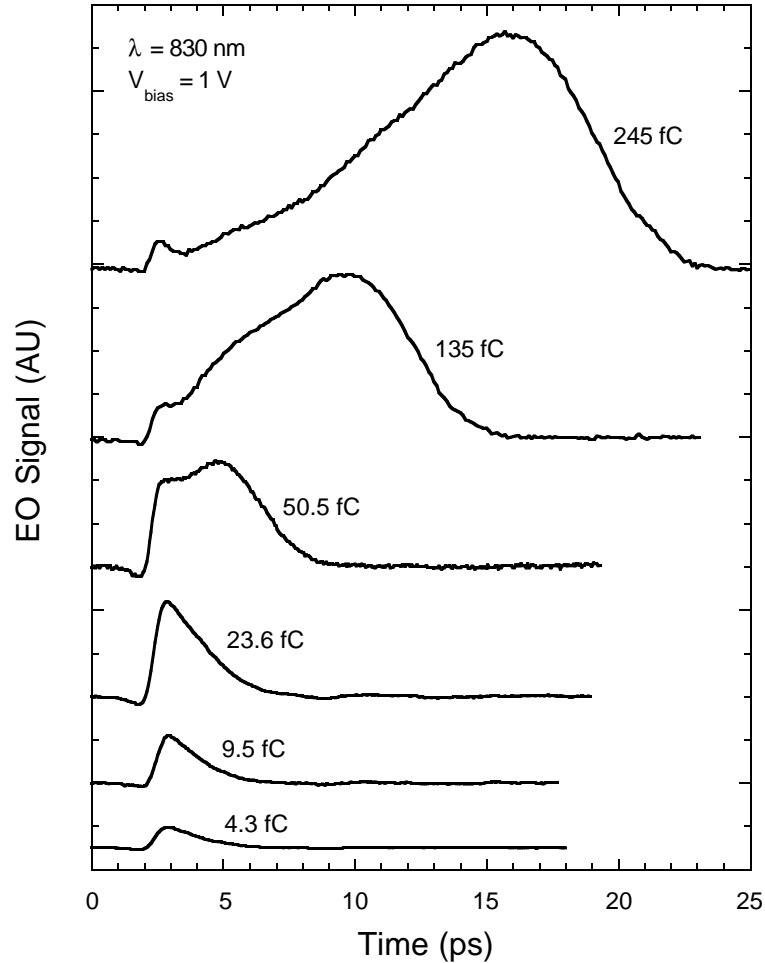


Fig. 5.19 Pulse responses of a  $3 \mu\text{m} \times 3 \mu\text{m}$  VPD showing effects of photogenerated charge from 4 fC to 245 fC. Traces are offset for clarity.

After the field collapses, it gradually recovers and a large, slow pulse is produced. The shape of this portion of the response is determined by the details of the carrier dynamics under field screening conditions. As discussed in Section 2.5, there are large longitudinal carrier and field gradients in the TWPD that do not exist in the VPD. The gradients result in significant longitudinal carrier drift and diffusion in the TWPD that do not occur in a uniformly illuminated VPD. These dynamics likely explain the difference in the shape of the slow portion of the high-charge response between the two types of photodetectors.

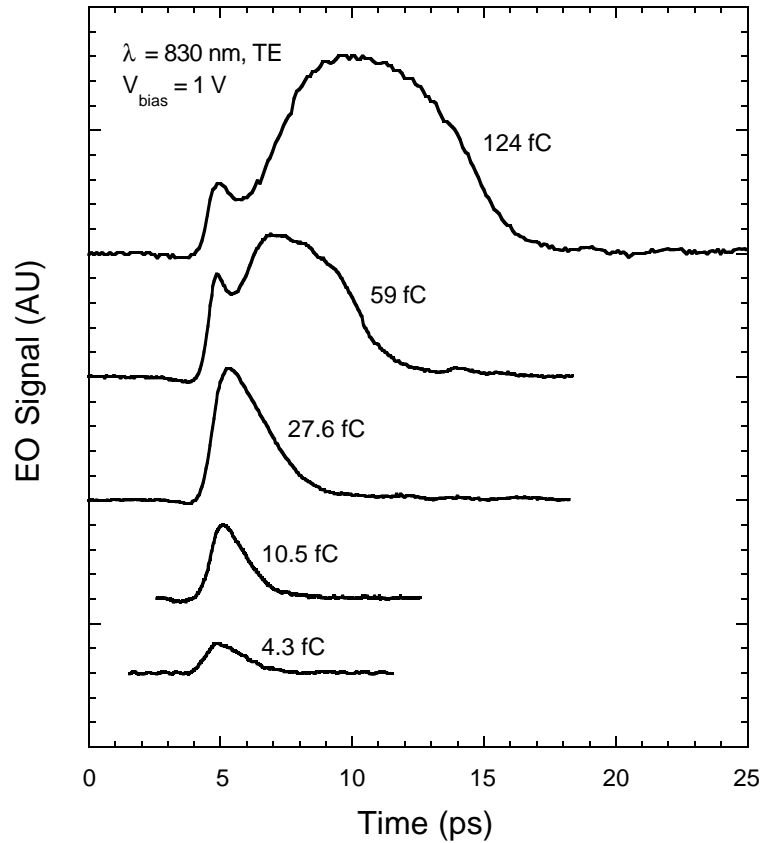


Fig. 5.20 Pulse responses of a 7  $\mu\text{m}$  long TWPD showing effects of photogenerated charge from 4 fC to 124 fC. Traces are offset for clarity.

Bandwidths from Fourier transforms of pulse responses are plotted versus photogenerated charge in Fig. 5.21. At low photogenerated charge, the bandwidths of both types of devices are primarily limited by saturated carrier drift, as discussed in Section 5.1. The slow portion of the response determines the bandwidth at high photogenerated charge levels.

A field-screening threshold can be derived by extrapolating the higher photogenerated charge portions of the curves in Fig. 5.21 to the low photogenerated charge bandwidth. The field-screening threshold of the VPD is 17.3 fC, about 24% higher than the 14.0 fC threshold of the TWPD. Inserting the field-screening

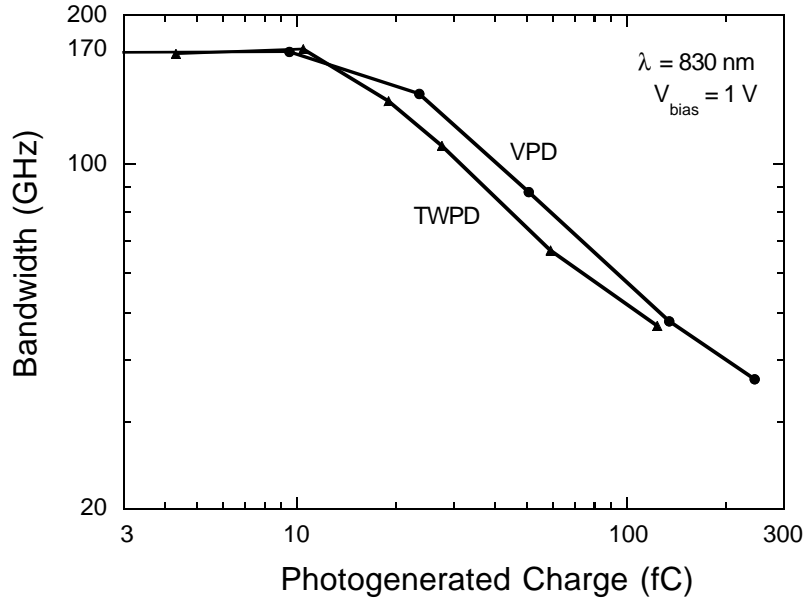


Fig. 5.21 3-dB electrical bandwidths from pulse responses of a  $3\ \mu\text{m} \times 3\ \mu\text{m}$  VPD and a  $7\ \mu\text{m}$  long TWPD versus photogenerated charge.

threshold of the VPD into Eq. (2.34) gives a field-screening threshold area density,  $\sigma_{fs} = 1.6\ \text{fC}/\mu\text{m}^2$ .

Substituting this field-screening threshold area density into (2.36) yields  $b = 2.5$ . This large factor clearly indicates that effects related to parallel illumination, analyzed in Section 2.5, have significant impact on TWPD response at high photogenerated charge levels. The high photogenerated carrier density of  $1.4 \cdot 10^5\ \mu\text{m}^{-3}$  ( $1.4 \cdot 10^{17}\ \text{cm}^{-3}$ ) at the input of the TWPD implies that nonlinear absorption is occurring at the field-screening threshold.

This analysis implies that the effective area for field-screening threshold is 1.7 times the velocity-mismatch effective area, according to (2.37). Thus, a TWPD with bandwidth limited by velocity mismatch should have a larger field-screening threshold than a VPD of the same RC-limited bandwidth.

The measurements and analysis presented in this chapter support the principles and design of TWPDs presented in previous chapters. The TWPDs have record bandwidths and bandwidth-efficiency products, as predicted. Analysis of electrical

attenuation in TWPDs and WGPDs reinforces the theory of distributed photodetection. Electrical reflections are deconvolved from high-charge measurements, which are consistent with the description of field-screening effects in Chapter 2.

## References

- [1] Model 350150 MLBB-B, Corning, Inc., Corning, NY.
- [2] S. M. Sze, *Physics of Semiconductor Devices*, 2nd ed. New York: John Wiley & Sons, 1981, p. 850.
- [3] Model F-SF, Newport Corp., Irvine, CA.
- [4] J. C. Yi, *yimodel*, University of California, Santa Barbara, CA.
- [5] J. C. Yi, S. H. Kim, S. S. Choi, "Finite-Element Method for the Impedance Analysis of Traveling-Wave Modulators," *J. Lightwave Technol.*, vol. 8, no. 6, pp. 817-822, Jun., 1990.
- [6] A. V. Uskov, J. R. Karin, R. Nagarajan, and J. E. Bowers, "Dynamics of Carrier Heating and Sweepout in Waveguide Saturable Absorbers," *IEEE J. Quantum Electron.*, submitted.

## CHAPTER 6

### OVERVIEW

The goal of surpassing the bandwidth-efficiency limitation of conventional photodetectors is verily attained with the invention of the travelling-wave photodetector (TWPD) in this thesis work. The 84 GHz bandwidth-efficiency product of the TWPD is more than double the inherent limit of vertically illuminated photodetectors (VPDs) and more than 50% larger than the previous best result for waveguide photodetectors (WGPDs) or any other type of photodetector without gain [1-3].

The apparently successful introduction of this new type of photodetector should not overshadow the potential for further innovation. The TWPD would benefit from further analysis and novel concepts. The experiences of this project afford some ideas.

Ultimately, the value of the TWPD lies in systems applications. From a simplistic viewpoint, the structure of the TWPD appears to be well-suited for integration in optoelectronic integrated circuits (OEICs). Much development, with many subtle compromises, remains to make several components function on the same chip. Eventually, TWPDs may appear in large-scale systems applications.

#### 6.1 Summary

The motivation for developing a distributed photodetector arises from the limitations on conventional, lumped-element VPDs and WGPDs. The TWPD is a WGPD designed to support microwave propagation on the device structure with characteristic impedance matched to the load. The optical wave propagating in the waveguide produces current waves that propagate on the electrical waveguide. The mismatch between the optical group velocity and the electrical phase velocity results in a bandwidth limitation that replaces the lumped RC bandwidth limitation.

The velocity-mismatch impulse response and bandwidth limitation are derived in the theory of distributed photodetection. A simple equation for velocity-mismatch effective area, suitable for device design, is distilled from the resulting expression. Effects unique to TWPDs under high-illumination are identified and equations for the field-screening threshold are derived and related to those for VPDs.

A hybrid-coplanar geometry TWPD is analyzed and a suitable bandwidth model is developed. The simple equation for the velocity-mismatch effective area is substituted for the junction area of a lumped-element device in the standard expression for the RC bandwidth limitation. An optimized design is fabricated in the AlGaAs material system using a modified ridge-waveguide laser process.

State-of-the-art optoelectronic measurement techniques are used to demonstrate record performance of high-speed photodetectors. Pump-probe electro-optic (EO) sampling is especially well suited for such measurements. However, large measurement bandwidth and high sensitivity requirements dictate that special features be integrated in the design and fabrication of the prototype TWPDs. The fabricated sample is part of the measurement system.

VPDs and WGPDs are fabricated on the same wafer for direct comparison with the TWPDs. The transmission line regions are rendered semi-insulating with proton implantation. The opaque GaAs substrate is removed, leaving a thin AlGaAs sublayer for EO sampling measurements. Lateral dimensions of the coplanar waveguide (CPW) transmission lines that connect to the photodetectors are restricted so that most of the modal fields are confined in the thin sublayer. Long CPW lines allow time-windowing to eliminate reflections in the pulse responses.

Bandwidths measured on the TWPDs break the record for p-i-n photodetector bandwidth by 70% and the record for bandwidth-efficiency product of any photodetector without gain by 50%. Comparisons of TWPD, VPD, and WGPD bandwidths versus junction area provide clear evidence that TWPDs are not lumped-element devices. Propagation constant analysis corroborates this assertion.

Corrections to the EO sampling system response allow a more accurate assessment of device performance. Reflection deconvolution inspires confidence in the detailed features of device responses under high illumination. Field-screening is proposed as the dominant effect seen in the photodetector responses under high

illumination. TWPDs may have a higher field-screening threshold than comparable VPDs.

## 6.2 Further Analysis & Improvements

This work includes all aspects of the invention process, but it provides only a basic understanding of TWPDs. Many questions and problems remain to be solved at every stage. Many opportunities remain for creative design and implementation.

A nonideal interface between the TWPD and the connecting electrical waveguide likely contributes to the disagreement between the predicted and measured propagation constants of Sections 3.3 and 5.2. There is a large change in the electric field pattern at the interface between the TWPD and the connecting electrical waveguide. The electric fields in the TWPD are confined to the thin *i*-layer, while the E-fields in the waveguide span the metal pattern. The change in magnetic field patterns between the TWPD and the waveguide is not as drastic since the currents are confined to the metals. A two-dimensional parallel-plate TWPD model could be used to gain a useful understanding of this problem.

Metal roughness and spiking of the ohmic contacts into the cladding layers is sited as another factor in the difference between the predicted and measured propagation constants. There are two approaches to dealing with this: change the model or change the structure. Changing the model would require extensive investigation into the detailed nature of the ohmic contacts. There is much literature on this subject, but it is not clear that a model implementation would be tractable.

Nonalloyed ohmic contacts are smooth and eliminate the problem of spiking, which is of concern only for the top contact of a hybrid-coplanar TWPD. The problems associated with alloyed contacts affect other types of devices, as well, so there are many recent publications focussing on nonalloyed contacts. Grading to a lower bandgap InGaAs cap layer has yielded nonalloyed specific contact resistances to n-type GaAs equal to or better than that obtained in this work [4-6]. Very heavy carbon doping produces very low resistance p-type contacts to GaAs and AlGaAs [7, 8].

A model of high-illumination effects in TWPDs is needed to verify and extend the simple model presented in Section 2.5. A two dimensional model would show time

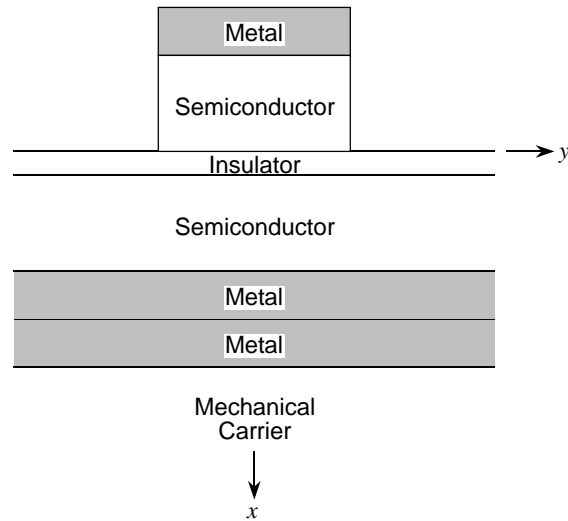


Fig. 6.1 Microstrip TWPD fabricated using metal bonding and substrate removal.

evolution of the electric field and carrier densities in the device, elucidating the detailed nature of longitudinal drift and diffusion. A more accurate model would account for nonlinear absorption and carrier heating in the drift field.

A number of different TWPD structures may have advantages. A microstrip geometry such as that drawn in Fig. 6.1 could be fabricated using metal bonding and substrate removal techniques [9]. The parallel-plate model of Sections 2.1 and 2.2 applies directly. This structure would have much lower series resistance in the bottom semiconductor layer. This thin microstrip technology, in general, has tremendous potential for very high frequency circuits due to its small dimensions and direct access to top and bottom contacts of vertical structures. Microstrip-air transmission lines would reduce loss and increase propagation velocity between components.

There is not much difference between saturated electron and hole velocities in GaAs, but the difference in InGaAs/InP is significant. In this material system, the transit-time bandwidth limitation is dominated by the holes, which only contribute half of the photocurrent. Adding a higher bandgap electron drift layer, as shown in Fig. 6.2(a), increases the electron contribution to the photocurrent and decreases the hole contribution, as plotted in Fig. 6.2(b). The absorption layer in this extended-drift heterostructure (EDH) would be thinner for faster hole transit, while the total depletion region would be thicker for lower capacitance. This is an effective means of

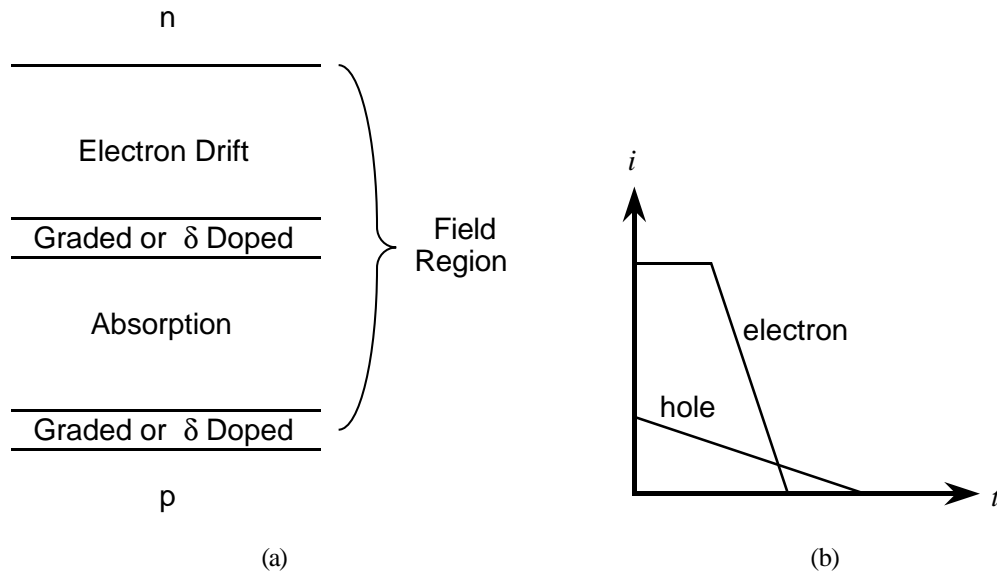


Fig. 6.2 Extended-drift heterostructure (a) epitaxial design and (b) drift current impulse response.

increasing the bandwidth of any type of photodetector in which the holes are significantly slower.

A decreasing impedance taper from the TWPD input to the output would continuously reflect the reverse travelling wave and may increase the bandwidth without compromising efficiency. This technique has been used to eliminate the backward wave in travelling-wave amplifiers [10-12]. A practical fully distributed structure would be awkward, but a periodic TWPD, discussed in the next section, could accommodate such a scheme.

### 6.3 Periodic Travelling-Wave Photodetector

This dissertation has concentrated on continuous or fully distributed TWPDs. A periodic structure in which discrete photodetectors load an electrical transmission line has similar characteristics [13, 14]. Two advantages of a periodic TWPD are greater design flexibility and reduced electrical loss. The velocity-mismatch bandwidth limitation could be eliminated in a velocity-matched periodic TWPD with a matched input termination. Another possible approach to high bandwidth and high efficiency would be impedance tapering, discussed in the previous section.

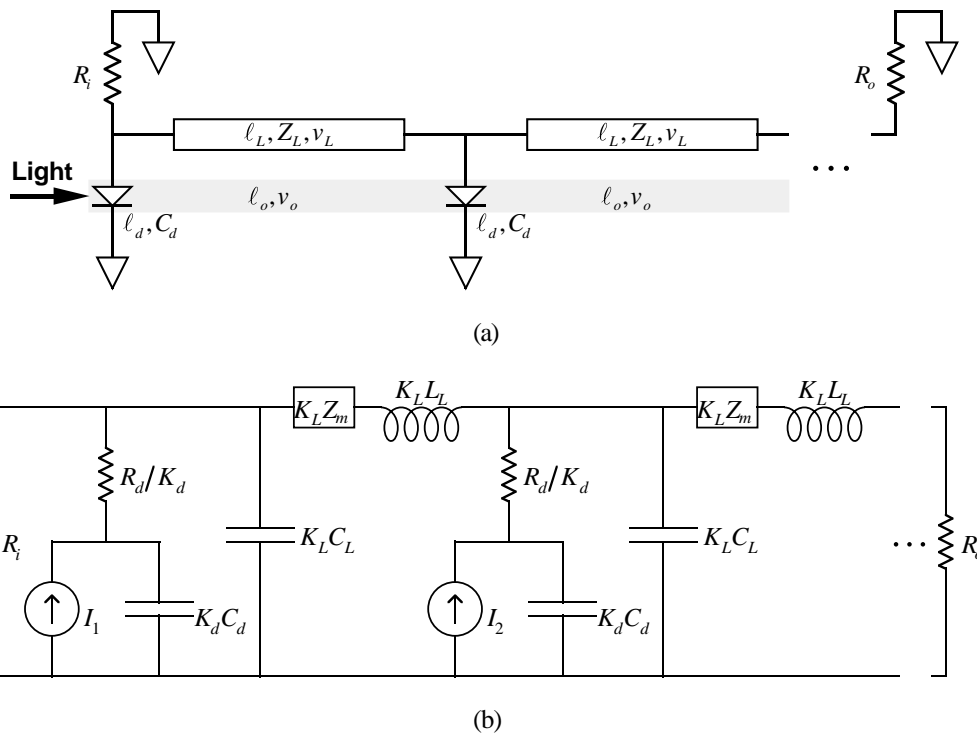


Fig. 6.3 Periodic TWPD (a) conceptual model and (b) equivalent circuit diagram.

A conceptual model of a periodic TWPD is depicted in Fig. 6.3(a). The discrete photodiodes are placed periodically on an optical waveguide and connected to an electrical transmission line. The periodic structure decouples design parameters for the photodiodes and the transmission line. Electrically, the device is a transmission line loaded with the capacitances of the discrete photodiodes. The impedance and electrical velocity are not dependent on the photodiode design, as they are in the fully distributed device. Standard transmission line impedances and variable electrical velocities can be achieved independently of photodiode cross-sectional dimensions.

The periodic TWPD circuit model is in Fig. 6.3(b). The parallel conductance of the doped semiconductor layers of a fully distributed structure and the associated electrical attenuation are largely eliminated in a periodic structure. The inductance is approximately that of the transmission line, and the capacitance is the sum of the diode and transmission line contributions. The photodiode, optical waveguide, and transmission line lengths can be varied independently, so the fractional lengths in Fig.

6.3(b),  $K_L \equiv \ell_L/\ell_o$  and  $K_d \equiv \ell_d/\ell_o$ , scale the transmission line and photodiode lengths relative to the optical waveguide length.

The overall device bandwidth will be limited by the bandwidths of the individual photodetector elements and velocity mismatch. The photodiode bandwidth limitation is calculated from a lumped element model with load impedance of  $Z_{0+}Z_{0-}/(Z_{0+} + Z_{0-})$ , where  $Z_{0+}$  is the impedance looking forward in the structure and  $Z_{0-}$  is the impedance looking backward. The velocity mismatch bandwidth limitation is given by the same equations as for the fully distributed device.

The parameters for a velocity-matched periodic TWPD are found with appropriate substitutions in the standard lossless transmission line equations for characteristic impedance and phase velocity,

$$\frac{Z_L^2}{Z_0^2} = \frac{(v_L/K_L)^2}{v_o^2} = 1 + \frac{K_d C_d}{K_L C_L} \quad (6.1)$$

where  $Z_L$  and  $Z_0$  are the characteristic impedances of the unloaded and loaded transmission lines,  $v_L$  is the phase velocity of the unloaded transmission line, and  $C_L$  and  $C_d$  are the capacitances per unit length of the unloaded transmission line and the photodiode. The optical group velocity,  $v_o$ , is set equal to the phase velocity of the loaded transmission line. Implicit in these equations are constraints on the characteristic impedance and fractional lengths,

$$1 \leq \frac{Z_L}{Z_0} \leq n_{eff} \quad (6.2a)$$

$$1 \leq K_L \leq n_{eff} \quad (6.2b)$$

$$0 \leq K_d \leq 1 \quad (6.2c)$$

where  $n_{eff}$  is the effective index of refraction of the optical waveguide.

The design parameters for a velocity-matched periodic TWPD from Eqs. (6.1) are plotted in Fig. 6.4. The lowest microwave loss occurs when the transmission line lengths are equal to the optical waveguide lengths,  $K_L = 1$ . However, only designs with  $K_L > 1$  have been proposed in [13, 14].

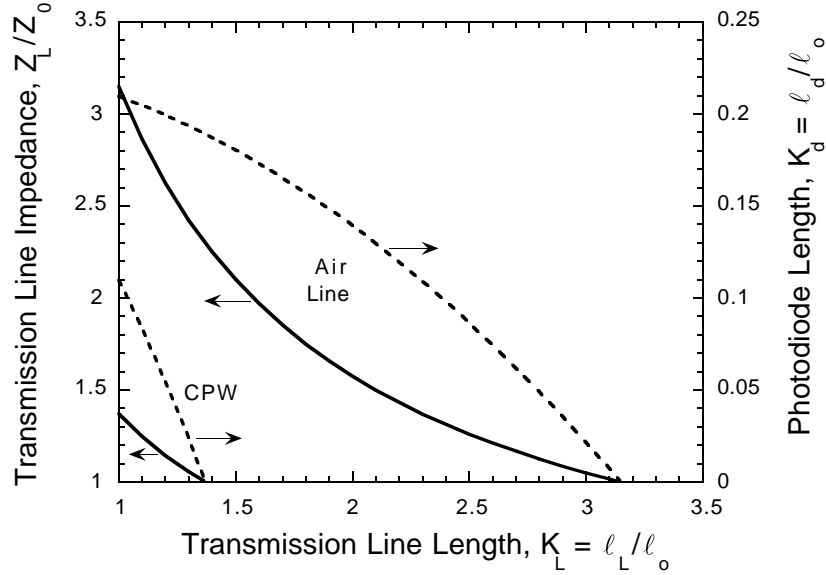


Fig. 6.4 Design parameter space for velocity-matched periodic TWPDs.

The periodic structure is an electrical low-pass filter with cutoff at the Bragg frequency. For a given bandwidth, the device period is limited by the electrical velocity. Reflections and scattering at the optical (diode/waveguide) interfaces can degrade the bandwidth and efficiency. Microwave loss may become significant for very long devices, also.

Fabrication of such a periodic TWPD would be more complicated than for a fully distributed TWPD. The simplest physical structure would consist of a p-i-n optical waveguide that is isolated and rendered low optical loss between photodiode sections. This could be accomplished by ion implantation. It may be convenient and advantageous to insert optical gain regions in long optical paths rather than low-loss optical waveguide. This could yield efficiencies greater than one, albeit with added noise. Optical preamplification is discussed briefly in the next section. A separate air transmission line could be suspended above the optical waveguide by posts that contact the photodetectors [15].

The periodic TWPD is an intriguing possibility from a theoretical viewpoint. However, the more complicated fabrication techniques and likely marginal

improvement in performance over a fully distributed TWPD raise doubts about the practical future of the periodic TWPD.

#### 6.4 Applications

Photodetectors are used in photoreceivers. The TWPD and travelling-wave amplifier (TWA) are a natural match since they are both very broadband devices [10, 16]. Low characteristic impedance results in a large thermal noise, but it has been predicted that the thermal noise penalty can be reduced to below 0.1 dB by inserting 30 dB of optical gain before a photodetector loaded in  $50 \Omega$  [17].

Integrated optical preamplifiers were included on the TWPD mask and fabricated. They did not provide gain, though, due to high surface recombination in the active region and poor carrier confinement in the shallow, graded double heterostructure. The active region was exposed in the waveguide etch and there were no steps taken to remove the surface region damaged by the dry etch. Stopping the waveguide etch before the i-layer and a compromise in the epitaxial design may be required for functional integrated optical preamplifiers.

Effective use of optical preamplification requires narrowband optical filtering to eliminate spontaneous emission noise. A practical integrated optical preamplifier/photodetector must also include an optical filter between the two devices. The filter can also be used for demodulating an optical frequency division multiplexed (OFDM) signal. An etched reflection grating can direct several narrowband optical signals to TWPDs simultaneously after the composite signal has been preamplified [18, 19]. Although somewhat larger and requiring fabrication of low-loss optical waveguide, star couplers can be connected to act as grating multiplexers/ demultiplexers, also [20-22].

As a final note, it is important not to lose sight of the range of application of the TWPD. TWPDs offer a significant advantage only for systems requiring bandwidths above 100 GHz. Below this range, lumped element detectors are simpler and more cost effective. Eventually, however, TWPDs will be commonplace in optical transmission systems.

## References

- [1] J. E. Bowers and C. A. Burrus, Jr., "Ultrawide-Band Long-Wavelength p-i-n Photodetectors," *J. Lightwave Technol.*, vol. 5, no. 10, pp. 1339-1350, Oct., 1987.
- [2] K. Kato, A. Kozen, Y. Muramoto, Y. Itaya, T. Nagatsuma, and M. Yaita, "110-GHz, 50%-Efficiency Mushroom-Mesa Waveguide p-i-n Photodiode for a 1.55- $\mu\text{m}$  Wavelength," *IEEE Photon. Technol. Lett.*, vol. 6, no. 6, pp. 719-721, Jun., 1994.
- [3] Y. G. Wey, K. Giboney, J. Bowers, M. Rodwell, P. Silvestre, P. Thiagarajan, and G. Robinson, "110 GHz GaInAs/InP Double Heterostructure p-i-n Photodetectors," *J. Lightwave Technol.*, vol. 13, no. 7, pp. 1892-, Jul., 1995.
- [4] T. C. Shen, G. B. Gao, and H. Morkoç, "Recent developments in ohmic contacts for III-V compound semiconductors," *J. Vac. Sci. Technol. B*, vol. 10, no. 5, pp. 2113-2132, Sep./Oct., 1992.
- [5] T. Nittono, H. Ito, O. Nakajima, and T. Ishibashi, "Non-Alloyed Ohmic Contacts to N-GaAs Using Compositionally Graded  $\text{In}_x\text{Ga}_{1-x}\text{As}$  Layers," *Jpn. J. Appl. Phys.*, vol. 27, pp. 1718-1722, 1988.
- [6] C. K. Peng, G. Ji, N. S. Kumar, and H. Morkoç, "Extremely low resistance nonalloyed ohmic contacts on GaAs using InAs/InGaAs and InAs/GaAs strained-layer superlattices," *Appl. Phys. Lett.*, vol. 53, no. 10, pp. 900-901, Sep. 5, 1988.
- [7] A. Katz, C. R. Abernathy, and S. J. Pearton, "Pt/Ti ohmic contacts to ultrahigh carbon-doped p-GaAs formed by rapid thermal processing," *Appl. Phys. Lett.*, vol. 56, no. 11, pp. 1028-1030, Mar. 12, 1990.
- [8] A. Katz, C. R. Abernathy, S. J. Pearton, B. E. Weir, and W. Savin, "Ohmic contacts to heavily carbon-doped p- $\text{Al}_x\text{Ga}_{1-x}\text{As}$ ," *J. Appl. Phys.*, vol. 69, no. 4, pp. 2276-2279, Feb. 15, 1991.
- [9] R. Venkatasubramanian, M. L. Timmons, T. P. Humphreys, B. M. Keyes, and R. K. Ahrenkiel, "High-quality eutectic-metal-bonded AlGaAs-GaAs thin films on Si substrates," *Appl. Phys. Lett.*, vol. 60, no. 7, pp. 886-888, Feb. 17, 1992.
- [10] T. T. Y. Wong, *Fundamental of Distributed Amplification*. Boston: Artech House, 1993, Ch. 7.
- [11] D. C. Espley, "Generation of Very Short Pulses," *J. I. E. E.*, pt. IIIa, pp. 314-315, 1946.
- [12] D. C. Espley, E. C. Cherry, and M. M. Levy, "The pulse testing of wide-band networks," *J. I. E. E.*, pt. IIIa, pp. 1176-1187, 1946.
- [13] M. C. Wu and T. Itoh, "Ultrafast Photonic-to-Microwave Transformer (PMT)," presented at *LEOS Summer Topical Meeting on Optical Microwave Interactions*, Santa Barbara, CA, Jul. 19-21, 1993.
- [14] M. C. Wu, L.-Y. Lin, T. Itoh, "A new ultrafast photodetector: optical-to-microwave transformer," presented at *Generation, Amplification, and Measurement of Ultrashort Laser*

- Pulses*, Los Angeles, CA, USA, Jan. 25-27, 1994. (*Proceedings of the SPIE - The International Society for Optical Engineering*, vol. 2116 pp. 228-36, 1994.)
- [15] U. Bhattacharya, S. T. Allen, M.J.W. Rodwell, "DC-725 GHz sampling circuits and subpicosecond nonlinear transmission lines using elevated coplanar waveguide," *IEEE Microwave Guided Wave Lett.*, vol. 5, no. 2, pp. 50-52, Feb., 1995.
- [16] J. Pustl, B. Agarwal, R. Pullela, L. D. Nguyen, M. V. Le, M. J. W. Rodwell, L. Larson, J. F. Jensen, R. Y. Yu, M. G. Case, "Capacitive-Division Traveling-Wave Amplifier with 340 GHz Gain-Bandwidth Product," in *1995 IEEE MTT-S Microwave Symposium Digest*, May 15-19, 1995.
- [17] N. G. Jensen, E. Bødtker, G. Jacobsen, and J. Strandberg, "Performance of Preplified Direct Detection Systems Under Influence of Receiver Noise," *IEEE Photon. Technol. Lett.*, vol. 6, no. 12, pp. 1488-1490, Dec., 1994.
- [18] Grande, W.J.; Johnson, J.E.; Tang, C.L., "GaAs/AlGaAs photonic integrated circuits fabricated using chemically assisted ion beam etching," *Appl. Phys. Lett.*, vol. 57, no. 24, pp. 2537-2539, Dec. 10, 1990.
- [19] P. C. Clemens, G. Heise, R. März, H. Michel, A. Reichelt, and H. W. Schneider, "8-Channel Optical Demultiplexer Realized as SiO<sub>2</sub>/Si Flat-Field Spectrograph," *IEEE Photon. Technol. Lett.*, vol. 6, no. 8, pp. 1109-1111, Sep., 1994.
- [20] C. Dragone, "An NxN Optical Multiplexer Using a Planar Arrangement of Two Star Couplers" *IEEE Photon. Technol. Lett.*, vol. 3, no. 9, pp 812-815, Sep., 1991.
- [21] C. Cremer, G. Ebbinghaus, G. Heise, R. Muller-Nawrath, AND OTHERS, "Grating spectrograph in InGaAsP/InP for dense wavelength division multiplexing," *Appl. Phys. Lett.*, vol.59, no.6, pp. 627-629, Aug. 5, 1991.
- [22] C. Cremer, N. Emeis, M. Schier, G. Heise, G. Ebbinghaus, and L. Stoll, "Grating Spectrograph Integrated with Photodiode Array in InGaAsP/InGaAs/InP," *IEEE Photon. Technol. Lett.*, vol. 4, no. 1, pp. 108-110, Jan., 1992.



## APPENDIX A

### TRANSVERSE-RESONANCE SOLUTION PROGRAM

The following Matlab script calculates the fields and propagation characteristics of a parallel-plate travelling-wave photodetector [1]. The transverse resonance method is employed in Chapter 2 to find the characteristic equation (2.5). This program solves that equation numerically to find the propagation constant and characteristic impedance. The fields are then found by assuming a value at the electric wall (see Fig. 2.3) and propagating the solution through the structure.

Calculations specific to the main script and carried out in separate functions are listed in Sec. A.2. General functions and scripts are listed in Sec. A.3.

#### A.1 Main Script

```
% script TRppcssF
% Kirk S. Giboney
% 950603; modified 950706 from TrResppssF
% First Part:
% Calculates the propagation constant and characteristic impedance of a
% parallel-plate p-i-n waveguide by the transverse resonance method.
% The characteristic equation is solved by the secant method.
% The conductivity of doped semiconductor layers is varied.
% Second Part:
% Computes magnetic and electric fields by propagating waves in the
% plus-x direction.
clear
% SI Units
Prefixes
PhysCons
%
% Variable Initialization
% Array Sizing
Nss=4; % no. semiconductor conductivity points
```

```

Nx=501; % number of x-position points
r1=ones(1,Nss); % row vector of ones
r1n=[1:Nss]; % row vector of indices
c1=ones(Nx,1); % column vector of ones
% Frequencies
f=1e11 % frequency
wf=2*pi*f*r1; % radian frequency
% Material Parameters
ei=erAlGaAs(0)*epsilon0; % i-layer dielectric constant
si=0; % i-layer conductivity
epsilon_s=erAlGaAs(.22)*epsilon0; % s-layer dielectric constant
rs=[1e0 1e1 1e2 1e3]*micro; % s-layer resistivity
ss=1./rs; % s-layer conductivity
epsilon_c=erAlGaAs(0)*epsilon0; % c-layer dielectric constant
rc=1e4*micro; % c-layer resistivity
sc=1./rc; % c-layer conductivity
rm=2.3e-8; % metal resistivity (gold)
sm=1/rm; % metal conductivity
Z0Est=50; % design characteristic impedance
% Waveguide Dimensions
w=1*micro; % waveguide width
di=.2*micro; % i-layer thickness
D=(Z0Est*w)^2*ei/mu0/di; % overall waveguide thickness
dc=10*nano; % contact layer thickness
ds=(D-di-2*dc)/2; % semiconductor layer thickness
dm=.7*micro; % metal thickness
da=.2*micro; % air thickness for field calculations
% Circuit Elements
Ci=2*ei/di; % capacitance per unit area
Rs=rs*ds; % series resistance of semiconductor layer
Cs=epsilon_s/ds; % capacitance of semiconductor layer
Zs=Rs./(1+j*wf.*Rs*Cs); % impedance of semiconductor layer
Gs=ss*ds/3; % parallel conductance of semiconductor
Im=mu0*D/2; % inductance per unit area
% metal-air impedance
sdm=sqrt(2./(wf*mu0*sm)); % skin depth
hm=sqrt(j*wf*mu0/sm); % metal impedance
hxm0=hm.*coth((1+j)*dm./sdm); % metal-air transverse wave impedance
%
```

```

% Find Propagation Constant & Characteristics
% Wave Numbers
es=epsilons-j*ss./wf;
ec=epsilonc-j*sc./wf;
ki2=wf.^2*mu0*ei;
ks2=wf.^2*mu0.*es;
kc2=wf.^2*mu0.*ec;
% Iteration for kz
% initial values
Y1=1./(1./(j*wf*Ci)+Rs);
Y2=1./(1./(j*wf*Ci)+Zs);
Z1=1./(1./(j*wf*Lm)+Gs);
Z2=1./(1./(hxm0+j*wf*Lm)+Gs);
kz2_1=-Y1.*Z1;
kz2_2=-Y2.*Z2;
[g_1,relerr]=trppc(wf,kz2_1,ki2,ks2,kc2,hxm0,ei,es,ec,di,ds,dc);
% secant method
tol=1e-5;
a=1;
while any(any(relerr>tol))
    [g_2,relerr]=trppc(wf,kz2_2,ki2,ks2,kc2,hxm0,ei,es,ec,di,ds,dc);
    kz2_3=kz2_2-(kz2_2-kz2_1).*g_2./(g_2-g_1)/a;
    g_1=g_2;
    kz2_1=kz2_2;
    kz2_2=replnans(kz2_3,kz2_1);
end
kz2=kz2_2;
kz=sqrt(kz2);
% Transmission Line Parameters
ve=wf./real(kz)/1e6; % μm/ps
alpha=-imag(kz)/1e6; % /μm
Z0=kz./wf/w.*(di/ei+ds./es+dc./ec);
R0=real(Z0);
X0=imag(Z0);
%
% Field Calculations
% Transverse Wave Vectors & Impedances
kxi=sqrt(ki2-kz2);
hxi=kxi./wf./ei;

```

```

kxs=sqrt(ks2-kz2);
hxs=kxs./wf./es;
kxc=sqrt(kc2-kz2);
hxc=kxc./wf./ec;
kxm=(1-j)./sdm;
kxa=sqrt(wf.^2*mu0*epsilon0-kz2);
hxa=kxa./wf/epsilon0;
%      Magnetic Fields
%      H transmission matrix at i-s interface
G11is=(hxi-hxs)/(hxi+hxs);      % reflection coefficient at i-s interface
T11is=1./(1-G11is);
T12is=-G11is.*T11is;
T21is=T12is;
T22is=T11is;
%      H transmission matrix at s-c interface
G11sc=(hxs-hxc)/(hxs+hxc);      % reflection coefficient at s-c interface
T11sc=1./(1-G11sc);
T12sc=-G11sc.*T11sc;
T21sc=T12sc;
T22sc=T11sc;
%      H transmission matrix at c-m interface
G11cm=(hxc-hm)/(hxc+hm);      % reflection coefficient at c-m interface
T11cm=1./(1-G11cm);
T12cm=-G11cm.*T11cm;
T21cm=T12cm;
T22cm=T11cm;
%      H transmission matrix at m-a interface
G11ma=(hm-hxa)/(hm+hxa);      % reflection coefficient at m-a interface
T11ma=1./(1-G11ma);
T12ma=-G11ma.*T11ma;
T21ma=T12ma;
T22ma=T11ma;
%      spatial variables
x=linspace(0,D/2+dm+da,Nx)';
dx=(D/2+dm+da)/Nx;
%      H in i-layer
[Hpi,Hmi,Hpis,Hmis,nxis]=layerp(x,1,0,di/2,.5*r1,.5*r1,kxi);
%      transmission through i-s interface
Hps0=T11is.*Hpis+T12is.*Hmis;

```

```

Hms0=T21is.*Hpis+T22is.*Hmis;
%           H in s-layer
[Hps,Hms,Hpsc,Hmsc,nxsc]=layerp(x,nxis,di/2,D/2-dc,Hps0,Hms0,kxs);
%           transmission through s-c interface
Hpc0=T11sc.*Hpsc+T12sc.*Hmsc;
Hmc0=T21sc.*Hpsc+T22sc.*Hmsc;
%           H in c-layer
[Hpc,Hmc,Hpcm,Hmcm,nxcm]=layerp(x,nxsc,D/2-dc,D/2,Hpc0,Hmc0,kxc);
%           transmission through c-m interface
Hpm0=T11cm.*Hpcm+T12cm.*Hmcm;
Hmm0=T21cm.*Hpcm+T22cm.*Hmcm;
%           H in m-layer
[Hpm,Hmm,Hpma,Hmma,nxma]=layerp(x,nxcm,D/2,D/2+dm,Hpm0,Hmm0,kxm);
%           transmission through m-a interface
Hpa0=T11ma.*Hpma+T12ma.*Hmma;
Hma0=T21ma.*Hpma+T22ma.*Hmma;
%           H in a-layer
[Hpa,Hma,Hpae,Hmae,nxae]=layerp(x,nxma,D/2+dm,D/2+dm+da,Hpa0,Hma0,kxa);
Hpa=[Hpa; Hpae];
Hma=[Hma; Hmae];
%           H
Hp=[Hpi; Hps; Hpc; Hpm; Hpa];
Hm=[Hmi; Hms; Hmc; Hmm; Hma];
H=Hp+Hm;
HM=abs(H);
%           Electric Fields
%           transverse wave impedances vs. x
hxi_x=ones(nxis-1,1)*hxi;
hxs_xs=ones(nxsc-nxis,1)*hxs;
hxc_xc=ones(nxcm-nxsc,1)*hxc;
hxm_xm=ones(nxma-nxcm,1)*hxm;
hxa_xa=ones(Nx-nxma+1,1)*hxa;
hx_x=[hxi_x; hxs_xs; hxc_xc; hxm_xm; hxa_xa];
%
hzi_x=ones(nxis-1,1)*(kz./(wf.*ei));
hzs_xs=ones(nxsc-nxis,1)*(kz./(wf.*es));
hzc_xc=ones(nxcm-nxsc,1)*(kz./(wf.*ec));
em=epsilon0-j*sm./wf;
hzm_xm=ones(nxma-nxcm,1)*(kz./(wf.*em));

```

```

hza_xa=ones(Nx-nxma+1,1)*(kz./(wf.*epsilon0));
hz_x=[hzi_x; hzs_xs; hzc_xc; hzm_xm; hza_xa];
%           Ex & Ez
Ex=hz_x.*(Hp+Hm);
Ez=hx_x.*(-Hp+Hm);
ExM=abs(Ex);
EzM=abs(Ez);
% Characteristic Impedance
V0_x=cumsum(Ex)*dx*2;
Z0F=V0_x(nxsc-1,r1n)./H(1,r1n)/1e-6

```

## A.2 Specific Functions

```

function [y,reldif]=trppc(w,kz2,ki2,ks2,kc2,hxm0,ei,es,ec,di,ds,dc)
% Kirk S. Giboney
% 950608; modified 950705
% Characteristic equation for a parallel-plate p-i-n waveguide from the
% transverse resonance condition.
% Input: w (array) = radian frequency
% Input: kz2 (array) = longitudinal propagation constant squared
% Input: ki2 (array) = propagation constant in i-material squared
% Input: ks2 (array) = propagation constant in s-material squared
% Input: kc2 (array) = propagation constant in c-material squared
% Input: hxm0 (array) = metal-air wave impedance
% Input: ei (scalar) = dielectric constant in i-material
% Input: es (array) = dielectric constant in s-material
% Input: ec (array) = dielectric constant in c-material
% Input: di (array) = thickness of i-material x 2
% Input: ds (array) = thickness of s-material
% Input: dc (array) = thickness of c-material
% Output: y (array) = value of equation
% Output: reldif (array) = relative difference represented by y
%
% Calculate transverse propagation constants & wave impedances
kxi=sqrt(ki2-kz2);
hxi=kxi./w./ei;
tkxi=tan(kxi.*di/2);
kxs=sqrt(ks2-kz2);
hxs=kxs./w./es;

```

```

tkxs=tan(kxs.*ds);
kxc=sqrt(kc2-kz2);
hxc=kxc./w./ec;
tkxc=tan(kxc.*dc);
% Characteristic equation
hx_plus=hxc.*(hxm0+j*hxc.*tkxc)./(hxc+j*hxm0.*tkxc);
hx_minus=j*hxs.*(hxi.*tkxi+hxs.*tkxs)./(hxs-hxi.*tkxi.*tkxs);
y=hx_plus+hx_minus;
reldif=abs(y./hx_plus);

function [Hp,Hm,Hpe,Hme,Nxe]=layerp(x,Nxs,Ds,De,Hps,Hms,kx)
% Kirk S. Giboney
% 950622; modified
% Fields in a layer.
% Calculated in plus-x direction.
% Input: x (column vector) = x-values
% Input: Nxs (scalar) = starting x-index
% Input: Ds (scalar) = starting x-value
% Input: De (scalar) = ending x-value
% Input: Hps (row vector) = positive-x going field starting value
% Input: Hms (row vector) = negative-x going field starting value
% Input: kx (row vector) = x wave number
% Output: Hp (array) = positive-x going field
% Output: Hm (array) = negative-x going field
% Output: Hpe (row vector) = positive-x going field ending value
% Output: Hme (row vector) = negative-x going field ending value
% Output: Nxe (scalar) = ending x-index
%
nx=Nxs;
while x(nx)<De;
    x1=x(nx)-Ds;
    Hp=[Hp; Hps.*exp(-j*kx*x1)];
    Hm=[Hm; Hms.*exp(j*kx*x1)];
    nx=nx+1;
end
x1=De-Ds;
Hpe=Hps.*exp(-j*kx*x1);
Hme=Hms.*exp(j*kx*x1);
Nxe=nx;

```

### A.3 General Functions & Scripts

```

% script Prefixes
% Kirk S. Giboney
% 941214; modified 941214
% Values of prefixes
centi=1e-2;
milli=1e-3;
micro=1e-6;
nano=1e-9;
pico=1e-12;
femto=1e-15;
atto=1e-18;
kilo=1e3;
mega=1e6;
giga=1e9;
tera=1e12;
peta=1e15;
exa=1e18;

% script PhysCons
% Kirk S. Giboney
% 941130; modified 941220
% Physical Constants
% SI units unless otherwise noted
% Electromagnetic
epsilon0=8.854e-12;          % F/m
mu0=pi*4e-7;                % H/m
eta0=sqrt(mu0/epsilon0);    % ohms
c=1/sqrt(mu0*epsilon0);     % m/s
q=1.602e-19;                % C
m0=9.11e-31;                % kg
% Quantum & Statistical Mechanics
hP=6.625e-34;                % Js
hPeV=4.135e-15;             % eVs
kB=1.38e-23;                 % J/K
kBeV=8.62e-5;                % eV/K

```

```
function y=erAlGaAs(x)
% Kirk S. Giboney
% 9409; modified 941228
% AlGaAs relative dielectric constant
% (for energies far below bandgap)
% Input: x (scalar or vector) = AlAs fraction
% Output: y (scalar or vector) = relative dielectric constant
% Tiwari, p 800; Singh, p 825
y=12.91-2.85*x;

function x2=replnans(x3,x1)
% Kirk S. Giboney
% 950705; modified
% Replaces Nans in an array with corresponding elements from another
% array.
% Input: x3 (array) = may contain Nans
% Input: x1 (array) = does not contain Nans
% Output: x2 (array) = elements of x3 that are not Nans, otherwise x1
%
s3=find(isnan(x3));
x2=x3;
x2(s3)=x1(s3);
```

## References

- [1] The MathWorks, Inc., *The Student Edition of Matlab Version 4*. Englewood Cliffs, NJ: Prentice Hall, 1995.



## APPENDIX B

# FABRICATION PROCESS

A wafer with designated epitaxial layers is processed to produce working devices. Various steps etch material, deposit material, or alter material properties in photolithographically patterned areas of the wafer.

The following process plan details the sequence of steps for TWPD wafer fabrication. General process steps are described in sections on cleaning, photolithography, and spin-on films, and on chemical specifications and preparation.

### B.1 Process Plan

#### 0. PREPARATION

##### A. Cleave

Cut into quarters.  
Cut smaller test pieces from one quarter.  
Put wafer orientation marks on back side of each piece.

##### B. Visual Inspection

optical microscope  
photos

##### C. Electrical Test

##### 1. Four-Point Probe

test piece  
frontside & backside  
to determine resistivity of top layer & substrate

##### D. Wet Etch

test piece  
to determine wafer orientation

##### 1. Clean

##### 2. PR laser mask

AZ4330 [1] hard-baked

##### 3. Etch Substrate

H<sub>2</sub>SO<sub>4</sub>:H<sub>2</sub>O<sub>2</sub>:H<sub>2</sub>O 1:8:1 100 s (14.6 μm/min)

##### 4. Strip PR

ACE

## 5. Inspect

optical microscope

SEM (cleaved)

E. RIE

test piece

to acquire laser monitor trace

## 1. Clean

## 2. Etch into bottom contact layer

RIE Cl<sub>2</sub> ≤ 1E-6 Torr

7.5 sccm / 1.2 mtorr / 350 V / 60 W / 13.56 MHz 10 min

laser monitor

## I. TOP OHMIC &amp; SELF-ALIGNED OPTICAL WAVEGUIDE ETCH

2 masks

A. Top Metal

## 1. Clean

## 2. PR Tohmec (1)

AZ4110 [1] lift-off

## 3. Evaporate Top contact metal

n on top

n-contact metal

E-beam

≤ 1E-6 Torr

Material	Position	Program	R (Å/s)	T (Å)
Ni	1	1	4	60
AuGe	3	5	10	1000
Ni	1	1	4	150
Au	4	4	10	2500
Total				3710

p on top

p-contact metal

Thermal

≤ 1E-6 Torr

Material	Filament	Length (cm)	Diameter (in)	Density	Acoustic Impedance	I (A)	R (Å/s)	T (Å)
Cr	3			7.20	28.95	92	5	60
AuZn5%	1	3	.030	18.72	22.89	150	15	750
Cr	3			7.20	28.95	95	7	250
Au	2	25	.015	19.32	23.18	150	15	2500
Total								3560

## 4. Lift-off

ACE

stir 300 rpm

## 5. Inspect

optical microscope

Dektak

B. Waveguide Etch

## 1. PR Etch (2)

AZ4110

## 2. Etch to bottom contact layer

RIE Cl<sub>2</sub> ≤ 1E-6 Torr

7.5 sccm / 1.2 mtorr / 350 V / 60 W / 13.56 MHz ~6 min

laser monitor

monitor test piece (keep for four-point probing)

rinse H<sub>2</sub>O

~100 Å/min Au lost due to sputtering

## 3. Strip PR

ACE

## 4. Inspect

optical microscope

Dektak

## 5. Descum

if necessary

O<sub>2</sub> Plasma 300 mtorr / 200 W / 30 kHz 3 minrinse H<sub>2</sub>OC. Top Anneal

## 1. Clean

## 2. RTA

forming gas

n on top

n-contact

Mode	Time or Rate (s or C/s)	Temperature (C)
Dly	30	
Ramp	60	320
SS	30	320
Ramp	40	380
SS	15	380
Dly	120	

p on top

p-contact

Mode	Time or Rate (s or C/s)	Temperature (C)
Dly	30	
Ramp	60	320
SS	30	320
Ramp	40	420
SS	20	420
Dly	120	

### 3. Inspect

optical microscope

## II. BOTTOM OHMIC

1 Mask

### A. Bottom Metal

1. Clean

2. PR Bohmic (3)

AZ4110 lift-off

3. Evaporate Bottom contact metal

n on top

p-contact metal

Thermal  $\leq 1E-6$  Torr

Material	Filament	Length (cm)	Diameter (in)	Density	Acoustic Impedance	I (A)	R ( $\text{\AA}/s$ )	T ( $\text{\AA}$ )
Cr	3			7.20	28.95	92	5	60
AuZn5%	1	3	.030	18.72	22.89	150	15	750
Cr	3			7.20	28.95	95	7	250
Au	2	20	.015	19.32	23.18	150	15	2000
Total								3060

p on top

n-contact metal

E-beam  $\leq 1E-6$  Torr

Material	Position	Program	R ( $\text{\AA}/s$ )	T ( $\text{\AA}$ )
Ni	1	1	4	60
AuGe	3	5	10	1000
Ni	1	1	4	150
Au	4	4	10	2000
Total				3210

### 4. Lift-off

ACE stir 300 rpm

5. Inspect

optical microscope

Dektak

B. Bottom Anneal

1. Clean

2. RTA

forming gas

n on top

p-contact

Mode	Time or Rate (s or C/s)	Temperature (C)
Dly	30	
Ramp	60	320
SS	30	320
Ramp	40	405
SS	20	405
Dly	120	

p on top

n-contact

Mode	Time or Rate (s or C/s)	Temperature (C)
Dly	30	
Ramp	60	320
SS	30	320
Ramp	40	380
SS	15	380
Dly	120	

3. Inspect

optical microscope

III. ISOLATION

1 mask

A. Isolation Mask

1. PMGI

SAL-110 [2]

2. PR

AZ4330

lift-off

Isolation (4)

## 3. Evaporate Implant Mask

E-beam  $\leq 1E-6$  Torr

3x Stage

10 min between layers

Material	Position	Program	R/3.1 (Å/s)	T/3.1 (Å)	T (Å)
Ti	3	3	2	100	310
Au	4	4	5	1200	3720
Au	4	4	5	1600	4960
Au	4	4	5	2400	7440
Total					16430

## 4. Lift-off

ACE stir 300 rpm

B. Isolation Implant

## 1. Attach to 2" Si mechanical wafer

polyimide tape [3]

## 2. Implant H+ (proton) [4]

7° off angle

n on top

Layer	Energy (keV)	Dose (cm <sup>-2</sup> )	Maximum Beam Current (μA)	Intensity (mW/cm <sup>2</sup> )	Time (s)
n+ GaAs	12	6E+14	100	59	19
n+ AlGaAs	30	2.376E+14	50	74	15
n+ AlGaAs	60	3.076E+14	50	148	20
n+ AlGaAs	100	3.622E+14	50	247	23
p+ GaAs/AlGaAs	150	4.104E+15	50	370	263
p+ GaAs/AlGaAs	200	4.502E+15	50	493	288

p on top

Layer	Energy (keV)	Dose (cm <sup>-2</sup> )	Maximum Beam Current (μA)	Intensity (mW/cm <sup>2</sup> )	Time (s)
p+ GaAs/AlGaAs	12	1.5E+15	100	59	48
p+ GaAs/AlGaAs	30	2.376E+15	50	74	152
p+ GaAs/AlGaAs	70	3.076E+15	50	173	197
n+ AlGaAs	100	3.622E+14	50	247	23
n+ AlGaAs	150	4.104E+14	50	370	26
n+ AlGaAs	200	4.502E+14	50	493	29

## 3. Remove from mechanical wafer

C. Remove Isolation Mask

## 1. Etch exposed PMGI

O<sub>2</sub> Plasma 300 mtorr / 200 W / 30 kHz 6 minO<sub>2</sub> Plasma 300 mtorr / 200 W / 13.56 MHz 6 minrinse H<sub>2</sub>O

## 2. Lift-off NMP

1165 remover [5] 100 C 300 rpm 1-2 hrs

## 3. Inspect

optical microscope

## IV. PASSIVATION

1 mask

A. Polyimide Passivation & Planarization

## 1. Clean

## 2. Polyimide

Probimide 284 [6]  
medium-baked

## 3. PR Passivation (5)

AZ4110

## 4. Etch polyimide &amp; PR

O<sub>2</sub> Plasma 300 mtorr / 200 W / 30 kHz 15 minrinse H<sub>2</sub>O

## 5. Strip PR

ACE

## 6. Bake polyimide

crosslinked

## 7. Etch Polyimide

O<sub>2</sub> Plasma 300 mtorr / 200 W / 13.56 MHz 20 minrinse H<sub>2</sub>O

## 8. Inspect

optical microscope

SEM

Dektak

## V. INTERCONNECT &amp; FIRST TEST

1 mask

A. Interconnect Metal

1. Clean

2. PR Interconnect (6)

AZ4330 lift-off

3. Evaporate Interconnect Metal

E-beam  $\leq 1E-6$  Torr

3x Stage

10 min between layers

Material	Position	Program	R/3.1 ( $\text{\AA}/s$ )	T/3.1 ( $\text{\AA}$ )	T ( $\text{\AA}$ )
Ti	3	3	1	18	56
Au	4	4	5	1200	3720
Au	4	4	5	1200	3720
Total					7496

4. Lift-off

ACE stir 300 rpm

5. Inspect

optical microscope

SEM

Dektak

B. Finished Photographs

SEM

optical microscope (color)

C. Measure

test structures

## VI. CLEAVE &amp; SECOND TEST

0 masks

A. Thin

1. Attach to mechanical Si

face down

crystal wax 150 C

2. Attach to lapping chuck

paraffin wax 100 C

iterate to achieve planar mount

3. Lap

Al <sub>2</sub> O <sub>3</sub> Grit ( $\mu\text{m}$ )	Starting Thickness (mil)	Ending Thickness (mil)
14.5	20	10
5	10	8
1	8	8

4. Remove from lapping chuck
5. Remove from mechanical wafer
6. Clean

ACE

#### B. Cleave

1. Attach to low-tack tape

face up

2. Scribe

1  $\mu\text{m}$  tip diamond  
linear translation stage  
stereo microscope

3. Break

cover with tackless tape  
0.5 mm mandrel  
stereo microscope

#### C. Cleaved Photographs

optical microscope (color)

#### D. Measure

sampling oscilloscope

### VII. BACKSIDE ETCH, ANTI-REFLECTION COATING, & FINAL TEST

1 mask

#### A. Backside Etch

Absorbing substrate only

1. Attach to mechanical Si

do not use glass mechanical substrate  
face down  
crystal wax                      200 C  
work into wax well- make sure facets are protected  
don't clean excess wax from around chip

2. Etch

$\text{C}_6\text{H}_8\text{O}_7:\text{H}_2\text{O}_2$                       5:1                      no stirring  
0.3  $\mu\text{m}/\text{min}$                               10-11 hrs

3. Clean

excess wax from around chip  
ACE

4. Inspect

optical microscope  
look for facet damage

#### B. Transfer to Glass Substrate

1. Cut cover slip

number 2 thickness 18 mm square

size so that device facets will be 0.1-1 mm from edges of glass

2. Clean cover slip
3. HMDS cover slip  
expose to vapor 2 min
4. Spin UV curable epoxy  
Norland Optical Adhesive 61  
3 krpm 40 s
5. Place cover slip on chip  
epoxy down  
align edges
6. Expose Light Rectangle mask  
soft contact mode  
~0.1 mm separation  
7.5 mW/cm<sup>2</sup>  
5 min/position (overlapping rectangles)  
10 min/position (non-overlapping rectangles or single exposure)
7. Unmount from mechanical Si  
ACE ~1-1/2 hrs
8. Inspect  
optical microscope

### C. AR Coat Facets

1. Sputter deposit Si<sub>3</sub>N<sub>4</sub>  
1070 Å

### D. Measure

EO sampling

### E. SEM Photographs

## **B.2 Cleaning, Photolithography, & Spin-On Films**

### **A. CLEANING**

All subsequent steps must be completed after any solvent exposure.

#### 1. Soak TCE

only first cleaning and after exposure to unclean environment  
100 C 3 min

#### 2. Soak ACE

skip after lift-off  
3 min

#### 3. Soak NMP

Microposit 1165 remover  
Optional- to remove traces of photoresist insoluble in ACE  
100 C 3 min

4. Soak ISO

3 min

5. Soak H<sub>2</sub>O

3 min

6. Rinse H<sub>2</sub>O7. Etch clean

before passivation

HCl:H<sub>2</sub>O 1:100 30 sH<sub>2</sub>SO<sub>4</sub>:H<sub>2</sub>O 1:100 30 s if HCl etches sampleRinse H<sub>2</sub>O8. Bake

Oven 120 C 10 min

Cool 5 min

**B. HIGH RESOLUTION PHOTOLITHOGRAPHY**

AZ4110 [1]

1. Spin AZ4110

6 krpm 40 s -&gt; 1.1 μm

2. Bake

Oven 90 C 10 min

Cool 5 min

3. Remove edge bead

Expose 30 s

Develop AZ400K:H<sub>2</sub>O 1:44. Expose

HP mode vacuum ≥ 4

7.5 mW/cm<sup>2</sup>

8 s

5. Soak Toluene

lift-off only

8-9 min

6. DevelopAZ400K:H<sub>2</sub>O 1:4

60 s

70 s w/ Toluene soak

7. Hard-bake

etch only

Oven 120 C 30 min

Cool 5 min

8. Flood Expose

optional

30 s

9. Descum

O <sub>2</sub> Plasma	300 mtorr / 100 W / 30 kHz	10 s
-----------------------	----------------------------	------

10. Etch clean

before metal films

HCl:H <sub>2</sub> O	1:100	30 s	
H <sub>2</sub> SO <sub>4</sub> :H <sub>2</sub> O	1:100	30 s	if HCl etches layers

**C. THICK FILM PHOTOLITHOGRAPHY**

AZ4330 [1]

1. Spin AZP4330

5 krpm	40 s -> 3.3 μm
--------	----------------

2. Bake

Oven	90 C	10 min
Cool	5 min	

3. Remove edge bead

Expose	60 s	
Develop AZ400K:H <sub>2</sub> O	1:4	40 s

4. Expose

HP mode vacuum  $\geq 4$   
 7.5 mW/cm<sup>2</sup>  
 13 s

5. Soak Toluene

lift-off only  
 10 min

6. Develop

AZ400K:H<sub>2</sub>O 1:4  
 90 s  
 90 s w/ Toluene soak

7. Hard-bake

etch only

Oven	120 C	30 min
Cool	5 min	

8. Flood Expose

optional  
 60 s

9. Descum

O <sub>2</sub> Plasma	300 mtorr / 100 W / 30 kHz	10 s
-----------------------	----------------------------	------

10. Etch clean

before metal films

HCl:H <sub>2</sub> O	1:100	30 s	
H <sub>2</sub> SO <sub>4</sub> :H <sub>2</sub> O	1:100	30 s	if HCl etches layers

**D. PMGI**

SAL-110 [2]

**1. Spin PMGI**6 krpm                      40 s                      -> ~1  $\mu\text{m}$ **2. Bake**Oven                      250 C                      1 hr  
Cool                      10 min**E. POLYIMIDE**

Probimide 284 [5]

**1. Spin adhesion promoter**

QZ3289:QZ3290 1:9

expires in 3 days

6 krpm                      40 s

**2. Spin Probimide 284**6 krpm                      40 s -> 1.1  $\mu\text{m}$ **3. Bake**

Programmable oven

N<sub>2</sub> atmosphere

Ramp 5 C/min

Level	Temperature (C)	Time (min)
Soft-Baked	90	30
Medium-Baked	150	15
Hard-Baked	240	15
Crosslinked	320	60
Cool	Oven Off	120
Total		240

**B.3 Chemical Specifications & Preparation****A. REAGENT INITIAL CONCENTRATIONS**

Name	Formula	Concentration	By
Hydrofluoric Acid	HF	49%	weight
Hydrochloric Acid	HCl	37%	weight
Sulfuric Acid	H <sub>2</sub> SO <sub>4</sub>	98%	weight
Citric Acid	C <sub>6</sub> H <sub>8</sub> O <sub>7</sub>	50%	weight
Hydrogen Peroxide	H <sub>2</sub> O <sub>2</sub>	30%	volume

**B. GENERAL ETCH SOLUTION PREPARATION****1. Dilute acid**

Slowly pour acid into water.

2. Add hydrogen peroxide

3. Set temperature

Wait to cool to room temperature before etching.

### C. CITRIC ACID SOLUTION PREPARATION

1. Mix citric acid crystals

Put 50 g of *anhydrous* citric acid crystals in 50 ml of H<sub>2</sub>O.

Alternatively, put 50 g of citric acid *monohydrate* crystals in 45 ml of H<sub>2</sub>O.

2. Wait for dissolution

Allow at least one full day for the C<sub>6</sub>H<sub>8</sub>O<sub>7</sub> to enter solution.

### References

- [1] Hoechst-Celanese Corp., Somerville, NJ.
- [2] SAL-110, Shipley, Marlborough, MA.
- [3] Kapton (Scotch brand #5413), 3M Corporation, St. Paul, MN.
- [4] IICO Corp., Santa Clara, CA.
- [5] Microposit 1165 Remover, Shipley, Marlborough, MA.
- [6] CIBA-GEIGY Corp., Santa Clara, CA.